High-Resolution Spectroscopic Investigations Of Various Trace Gases And Their Isotopologues Using Cavity Ring-Down Spectroscopy.

A thesis submitted for the degree of

Doctor of Philosophy (Science)

in

Physics (Experimental)

by

Biswajit Panda

Department of Physics

University of Calcutta

2023

Dedicated to my family and supervisor…

Abstract

The measurements of stable isotopic compositions of molecules are extremely important to explore various underlying physical and chemical processes and they can contribute to the identification of potential sources and sinks. Anthropogenic activities of various gas molecules and their isotopes like methane (CH_4), carbon dioxide (CO_2), nitrous oxide (N_2O) [greenhouse gases] are always prime members of global warming.

In this thesis, we have utilized our home-built laboratory developed quantum cascade (QCL) laser-based cavity ring-down spectroscopy (CRDS) technique for high-resolution spectroscopic investigation of trace gas molecules. In the first part of the thesis, we probed the $\nu_4(F_2)$ fundamental band of $^{13}CH_4$ at around 1301 cm^{-1} and subsequently acquired high-resolution experimental spectra of 22 interference-free transition lines. Thereafter studied symmetry-specific different spectroscopic line-parameters i.e. line-intensity, pressure broadening coefficient along with temperature-dependence of broadening coefficient for complete spectroscopic characterization of the transition lines. Next, we probed the *a*-type ν_9 (B_2-symmetry) fundamental vibrational band of $^{12}CH_2D_2$ and explored the high-resolution ro-vibrational gas-phase spectra of this molecule. We performed the high-level Gaussian 16 calculations and PGOPHER simulation for accurate determination of various spectroscopic parameters of $^{12}CH_2D_2$.

In the next part of the thesis, we have coupled the QCL with a multi-pass cell to develop a high-sensitive gas sensor for the monitoring of trace gas molecules. We applied the wavelength modulation spectroscopy (WMS) technique for monitoring of two trace gas molecules NO and OCS and compared the signal-to-noise ratio with the direct absorption Furthermore, we next used the same fundamental principle of 2*f*-WMS to monitor CH_4 and N_2O concentrations both in ambient air and exhaled breath samples. High-resolution 2*f*-WMS spectra of both CH_4 and N_2O are recorded by probing the interference-free absorption lines in a single QCL scan of ~ 0.06 cm^{-1}. In the final part of the thesis, we have explored the catalytic activity of urea-urease kinetics in soil medium using utilizing integrated cavity output spectroscopy (ICOS). We investigated the temperature dependent effect on urea-urease hydrolysis in a soil medium. Further, we investigated any inhibition or activation effect of different concentrations of D_2O in the urea urease hydrolysis in a soil medium in both normal air and nitrogen environment.

ସଙ୍କ୍ଷେପ

ଅଣୁର ସ୍ଥିର ଆଇସୋଟୋପିକ ଗଠନର ମାପ ବିଭିନ୍ନ ଅନ୍ତର୍ନିହିତ ଶାରୀରିକ ଏବଂ ରାସାୟନିକ ପ୍ରକ୍ରିୟା ଅନୁସନ୍ଧାନ କରିବା ପାଇଁ ଅତ୍ୟନ୍ତ ଗୁରୁତ୍ୱପୂର୍ଣ୍ଣ ଏବଂ ସେମାନେ ସମ୍ଭାବ୍ୟ ଉତ୍ସ ଏବଂ ବୁଡ ଚିହ୍ନଟ କରିବାରେ ଯୋଗଦାନ କରିପାରିବେ। ମିଥେନ୍ (CH_4), ଅଙ୍ଗାରକାମ୍ଳ (CO_2), ନାଇଟ୍ରସ୍ ଅକ୍ସାଇଡ୍ (N_2O) [ଗ୍ରୀନ୍ହାଉସ୍ ଗ୍ୟାସ୍] ଭଳି ବିଭିନ୍ନ ଗ୍ୟାସ୍ ଅଣୁ ଏବଂ ସେଗୁଡ଼ିକର ଆଇସୋଟୋପର ଆନ୍ଥ୍ରୋପୋଜେନିକ୍ କାର୍ଯ୍ୟକଳାପ ସବୁବେଳେ ଗ୍ଲୋବାଲ୍ ବାର୍ମିଂର ମୁଖ୍ୟ ସଦସ୍ୟ।

ଏହି ଥିସିସରେ, ଆମେ ଆମର ଘର ନିର୍ମିତ ଲାବୋରେଟୋରୀ ବିକଶିତ କ୍ୱାଣ୍ଟମ କ୍ୟାସ୍କେଡ (ଜେଡସିଏଲ) ଲେଜର-ଆଧାରିତ ଗହ୍ୱର ରିଂ-ଡାଉନ ସ୍ପେକ୍ଟ୍ରୋସ୍କୋପି (ସିଆରଡିଏସ) ଟେକନିକକୁ ଟ୍ରେସ ଗ୍ୟାସ ଅଣୁର ଉଚ୍ଚ-ରିଜୋଲ୍ୟୁସନ ସ୍ପେକ୍ଟ୍ରୋସ୍କୋପିକ ଅନୁସନ୍ଧାନ ପାଇଁ ବ୍ୟବହାର କରିଛୁ। ଥିସିସର ପ୍ରଥମ ଭାଗରେ, ଆମେ ପ୍ରାୟ 1301 ସେମି$^{-1}$ ରେ $^{13}CH4$ ର ν_4 (F2) ମୌଳିକ ବ୍ୟାଣ୍ଡକୁ ଅନୁସନ୍ଧାନ କଲୁ ଏବଂ ପରବର୍ତ୍ତୀ ସମୟରେ 22 ହସ୍ତକ୍ଷେପ-ମୁକ୍ତ ସଙ୍କ୍ରମଣ ରେଖାର ଉଚ୍ଚ-ରିଜୋଲ୍ୟୁସନ୍ ପରୀକ୍ଷଣ ସ୍ପେକ୍ଟ୍ରା ହାସଲ କଲୁ। ତା'ପରେ ସମମିତି- ନିର୍ଦ୍ଦିଷ୍ଟ ଭିନ୍ନ ଭିନ୍ନ ସ୍ପେକ୍ଟ୍ରୋସ୍କୋପିକ ରେଖା-ପ୍ରାଚ୍ୟ ଅର୍ଥାତ୍ ରେଖା-ତୀବ୍ରତା ଉପରେ ଅଧ୍ୟୟନ କଲେ, ସଙ୍କ୍ରମଣ ରେଖାର ସମ୍ପୂର୍ଣ୍ଣ ସ୍ପେକ୍ଟ୍ରୋସ୍କୋପିକ ବୈଶିଷ୍ଟ୍ୟୀକରଣ ପାଇଁ ତାପମାତ୍ରା ନିର୍ଭରଶୀଳତା ସହିତ ଚାପ ବୃଦ୍ଧିକାରୀ ଗୁଣକ। ତା'ପରେ ଆମେ $^{12}CH_2D_2$ ର a-type ν_9 (B2-symmetry) ମୌଳିକ କମ୍ପନ ବ୍ୟାଣ୍ଡର ଅନୁସନ୍ଧାନ କରି ଏହି ଅଣୁର ଉଚ୍ଚ-ରିଜୋଲ୍ୟୁସନ r-vibrational gas-phase spectraର ଅନୁସନ୍ଧାନ କରିଥିଲୁ। ଆମେ $^{12}CH_2D_2$ ର ବିଭିନ୍ନ ସ୍ପେକ୍ଟ୍ରୋସ୍କୋପିକ ପାରାମିଟରର ସଠିକ୍ ନିର୍ଦ୍ଧାରଣ ପାଇଁ ଉଚ୍ଚ ସ୍ତରୀୟ ଗାଉସିଆନ୍ 16 ଗଣନା ଏବଂ PGOPHER ସିମ୍ୟୁଲେସନ ପ୍ରଦର୍ଶନ କଲୁ।

ଥିସିସର ପରବର୍ତ୍ତୀ ଭାଗରେ ଆମେ ଟ୍ରେସ୍ ଗ୍ୟାସ୍ ଅଣୁର ଅନୁଧ୍ୟାନ ପାଇଁ ଏକ ଉଚ୍ଚ ସମ୍ବେଦନଶୀଳ ଗ୍ୟାସ୍ ସେନସର ବିକଶିତ କରିବା ପାଇଁ ଏକ ମଲ୍ଟି ପାସ୍ ସେଲ୍ ସହିତ ଜେଡ୍ସିଏଲକୁ ଯୋଡ଼ିଛୁ। ଆମେ ଦୁଇଟି ଟ୍ରେସ୍ ଗ୍ୟାସ୍ ଅଣୁ NO ଏବଂ OCSର ଅନୁଧ୍ୟାନ ପାଇଁ ତରଙ୍ଗ ଦୈର୍ଘ୍ୟ ମଡୁ୍ୟଲେସନ୍ ସ୍ପେକ୍ଟ୍ରୋସ୍କୋପି (WMS) କୌଶଳ ପ୍ରୟୋଗ କଲୁ ଏବଂ ସିଗନାଲ-ଟୁ-ନାଏଜ୍ ଅନୁପାତକୁ ସିଧାସଳଖ ଶୋଷଣ ସହିତ ତୁଳନା କଲୁ, ଏହା ପରେ ଆମେ 2f-WMS ର ସମାନ ମୌଳିକ ସିଦ୍ଧାନ୍ତକୁ ବ୍ୟବହାର କରି ସିଏଚ୍4 ଏବଂ ଏନ୍2ଓ ସାନ୍ଦ୍ରତାକୁ ଉଭୟ ପାରିପାର୍ଶ୍ୱିକ ବାୟୁ ଏବଂ ନିଃଶ୍ୱାସ ନେଉଥିବା ଶ୍ୱାସ ନମୁନାରେ ନିରୀକ୍ଷଣ କରିଥିଲୁ। CH_4 ଏବଂ N_2O ଉଭୟର ଉଚ୍ଚ-ବିକାଶ 2f-WMS ସ୍ପେକ୍ଟ୍ରାକୁ 0.06 ସେଣ୍ଟିମିଟର-1ର ଏକକ ଜେଡସିଏଲ ସ୍କାନରେ ହସ୍ତକ୍ଷେପ-ମୁକ୍ତ ଅବଶୋଷଣ ରେଖାକୁ ଯାଞ୍ଚ କରି ରେକର୍ଡ କରାୟାଏ। ଥିସିସର ଶେଷ ଭାଗରେ ଆମେ ଏକୀକୃତ ଗହ୍ୱର ଉତ୍ପାଦନ ସ୍ପେକ୍ଟ୍ରୋସ୍କୋପି (ଆଇସିଓଏସ)ର ଉପୟୋଗ କରି ମୃତ୍ତିକା ମଧ୍ୟମରେ ୟୁରିଆ-ୟୁରିଆ ଗତିଶୀଳତାର ଅନୁଘଟକ କାର୍ଯ୍ୟକଳାପର ଅନୁସନ୍ଧାନ କରିଛୁ। ଆମେ ଏକ ମୃତ୍ତିକା ମାଧ୍ୟମରେ ୟୁରିଆ-ୟୁରିଆ ହାଇଡ୍ରୋଲିସିସ୍ ଉପରେ ତାପମାତ୍ରା ନିର୍ଭରଶୀଳ ପ୍ରଭାବର ଅନୁସନ୍ଧାନ କରିଥିଲୁ। ଅଧିକନ୍ତୁ, ଆମେ ଉଭୟ ସାଧାରଣ ବାୟୁ ଏବଂ ଯବକ୍ଷାରଜାନ ପରିବେଶରେ ଏକ ମୃତ୍ତିକା ମାଧ୍ୟମରେ ୟୁରିଆ ୟୁରିଆଜ ହାଇଡ୍ରୋଲିସିସ୍ରେ D_2O ର ବିଭିନ୍ନ ସାନ୍ଦ୍ରତାର କୌଣସି ପ୍ରତିବନ୍ଧକ କିମ୍ବା ସକ୍ରିୟତା ପ୍ରଭାବର ଅନୁସନ୍ଧାନ କଲୁ।

List of publications related to the synopsis chapter

1. "High-resolution investigation of temperature and pressure-induced spectroscopic parameters of 13C-isotopomer of CH_4 in the v_4 band using cavity ring-down spectroscopy." **Biswajit Panda**, Sanchi Maithani, and Manik Pradhan. ***Chemical Physics***, *2020*, 110769.
2. "Ro-vibrational spectral features and pressure broadening dynamics of dideutero-methane ($^{12}CH_2D_2$) in the v_9 (B2) fundamental band." **Biswajit Panda**, Ardhendu Pal, Sanchi Maithani, Abhijit Maity, and Manik Pradhan, 2022. ***Journal of Molecular Spectroscopy***, *384*, 111572.
3. "Direct and 2f-wavelength modulation spectroscopy of NO and OCS using an astigmatic multipass cell coupled with a mid-IR 5.2 μm cw-QCL." **Biswajit Panda,** Ardhendu Pal and Manik Pradhan, 2022. ***Laser Physics***, *32*(3), 035702.
4. "An EC-QCL based dual-species (CH_4/N_2O) detection method at 7.8 μm in mid-IR region for simultaneous applications of atmospheric monitoring and breath diagnostics." **Biswajit Panda,** Ardhendu Pal, Soumyadipta Chakraborty, and Manik Pradhan, 2022. ***Infrared Physics & Technology***, *125*, 104261**.**
5. **"**Elucidation of temperature-dependent soil enzyme urease activity and observation of deuterium-enriched isotopic resonance effects**."** **Biswajit Panda**, Ardhendu Pal (2023, under review)

Other works apart from synopsis chapter

1. "Gas-Phase Isotopic Fractionation Study of Singly and Doubly Deuterated Isotopologues of Water in the H–D Exchange Reaction by Cavity Ring-Down Spectroscopy." Sanchi Maithani, **Biswajit Panda**, Abhijit Maity and Manik Pradhan. ***The Journal of Physical Chemistry A*** 124, 2020, 1104-1111.
2. "Cavity ring-down spectroscopy of l-type doubling in ^{15}N-β-site N_2O isotopomer near 7.8 μm." Ardhendu Pal, **Biswajit Panda**, Sanchi Maithani, and Manik. Pradhan, 2021. ***Journal of Molecular Spectroscopy***, 111523.
3. "l-doublet splittings in Δ vibrational state of $^{15}N^{14}N^{16}O$ isotopomer." Ardhendu Pal, **Biswajit Panda**, Sanchi Maithani and Manik Pradhan, ***Chemical Physics Impact***, 2021, 100049.
4. "Spectroscopic investigation of hydrogen and triple-oxygen isotopes in atmospheric water vapor and precipitation during Indian monsoon season." Sayoni Bhattacharya, Mithun Pal, **Biswajit Panda** and Manik Pradhan, 2021. ***Isotopes in Environmental and Health Studies***, 1-18.
5. "Elucidating Λ-doublet splittings and rotational quantum number-dependent collisional broadenings in $^2\Pi_{1/2}$ and $^2\Pi_{3/2}$ spin-split sub-bands of NO at 5.2 μm." A. Pal, S. Chakraborty, **B. Panda**, M. Pradhan, ***Journal of Molecular Spectroscopy***, 391,111719, **(2023).**
6. "Elucidation of rotational-interaction coupling and collision-induced effects in rovibrational transitions of β-N_2O isotopologue at 7.8 μm mid-infrared region by cavity ring-down spectroscopy." Chakraborty, Soumyadipta, Ardhendu Pal, **Biswajit Panda**, Indrayani Patra, and Manik Pradhan. ***Infrared Physics & Technology*** (2023): 104752.
7. "Development of a compact 406 nm diode laser-based cavity-enhanced spectrometer for high-sensitive detection of NO_2 levels in exhaust gas." Ardhendu Pal, Koushik Mondal, **Biswajit Panda** and Manik Pradhan. ***Laser Physics Letter***, 2023.

Acknowledgement

The present research work has been carried at S. N. Bose National Centre for Basic Sciences, Kolkata under the supervision of Prof. Manik Pradhan. First, I would like express my sincere gratitude to my supervisor Prof. Manik Pradhan for giving me the opportunity to work in his lab. I would also like to thank my supervisor for his continuous support, consistent motivation and great encouragement in my research work during the difficult covid time.

I would also address my thanks to Dr. Abhijit Maity, Dr. Mithul Pal and Dr. Sanchi Maithani for their productive discussions on my research work throughout my journey. Special thanks to Mr. Ardhendu Pal for his useful discussions during the development of experimental set-ups and for his assistance during the experiment. I am also thankful for my lab mates: Dr. Puspendu Barik, Dr. Jayeta Bannerjee, Dr. Akash Das, Dr. Koushik Mondol, Mr. Soumen Mondal, Mr. Somodipta Chakraborty and Mr. Indrayani Patra for their continuous support and valuable discussions.

I would also like to thank my school friends: Shibashis, Raja, Amaresh, Manoj, Manas, Aliva, Bikram, Kailash, Archana for staying beside me from school days to till now. I also convey my gratitude to friends in B.SC and M.SC days: Pratik, Naba, Bijay, Malay, Soumyashree, Dipak, Hari for their support in difficult times. I convey my heartiest gratitude to my fellow SNBNCBS mates for their wonderful company during my stay at SNBNCBS for almost five years, in particular, snb cricket and football fellows, Shivam, Vishal da, Shanshak da, Tanmay, Premashis, Anish, Debayan.

I also wish to express my love and gratitude to my grandparents, parents and younger brother for their continuous support, love, sacrifice and encouragement during bad days and good days, without them the journey would not be possible. I am greatly thankful to my special person in my life, Kabita for her persistent love, trust, encouragement and mental support during my PhD tenure, which helped me a lot to overcome difficulties in the research and personal life.

Finally, I would like to acknowledge S. N. Bose National Centre for Basic Sciences for doctoral research funding and for providing an excellent research environment.

Biswajit Panda

Table of content

Abstract…….…….…..iii

List of publications related to thesis work…….…..…v

List of publications apart from thesis work…….....vi

Acknowledgment……..…vii

Table of contents…….……ix

Chapter-1. Introduction……1

1.1 Background and motivation……1

1.2 Outline of the thesis…….3

Chapter-2. Importance of trace gas monitoring and an overview of spectroscopic techniques for trace gas monitoring……..5

2.1 Introduction…….6

2.1.1 Importance of trace gas in atmospheric monitoring and in biomedical diagnosis……6

2.1.2 Isotopic analysis and its application……..8

2.2 Fundamental spectroscopy……..10

2.2.1 Introduction to infrared spectroscopy……..…13

2.2.2.1 Vibrational spectroscopy…….....13

2.2.2.2 Rotational spectroscopy……..17

2.2.2.3 Ro-vibrational spectroscopy…….....19

2.3 Line intensity and line strength of spectral line……21

2.4 Line width and line shape function of spectral line……..…23

2.5 Overview of spectroscopy techniques for trace gas analysis…….26

2.5.1 Tunable diode laser absorption spectroscopy (TDLAS) …….26

2.5.2 Fourier transform infrared spectroscopy (FTIR)……...…27

2.5.3 Photoacoustic spectroscopy (PAS)……..27

2.5.4 Cavity enhanced absorption spectroscopy (CEAS)……..28

2.5.5 Wavelength modulation spectroscopy (WMS)…….....29

2.6 References……..30

Chapter-3. High-resolution investigation of temperature and pressure-induced spectroscopic $^{13}CH_4$ using cavity ring-down spectroscopy……...41

3.1 Introduction…….....42

3.2 Basic principles of CRDS technique…….....44

3.3 Quantum cascade laser as a mid-IR laser source …….....46

3.4 Experimental setup…….....47

3.5 Results and discussion……..…...48

3.5.1 Interference-free transition lines …….....48

3.5.2 Line-intensity measurements……..…… 49

3.5.3 Air-broadening coefficients at room temperature.……...53

3.5.4 Temperature dependence of broadening coefficients…….....56

3.6 Conclusion…….60

3.7 References…….....60

Chapter-4. Ro-vibrational spectral features and pressure broadening dynamics of dideutero-methane ($^{12}CH_2D_2$) in the $\nu_9(B_2)$ fundamental band ……65

4.1 Introduction…….66

4.2 Experimental section……..70

4.3 Results and discussions…….…….71

4.3.1 High-resolution absorption spectral lines of $^{12}CH_2D_2$……....71

4.3.2 Gaussian 16 and PGOPHER simulations…….....74

4.3.3 Line intensity measurements of $^{12}CH_2D_2$…….79

4.3.4 Pressure broadening investigations of $^{12}CH_2D_2$……..82

4.3.5 Squared transition moment measurements of $^{12}CH_2D_2$…….86

4.4 Conclusion……...88

4.5 References……. ……..89

Chapter-5 Direct and 2f-wavelength modulation spectroscopy of NO and OCS using an astigmatic multipass cell……....94

5.1 Introduction…….…..95

5.2 Basic Principle of wavelength modulation spectroscopy.....96

5.3 Experimental section……....97

5.4 Results and discussions……...….99

5.4.1 Selections of absorption lines…….....99

5.4.2 Optimization of 2f-WMS signal…….…….100

5.4.3 Calibration of 2f-WMS signal…….…....103

5.4.4 Allan Variance test……...104

5.4.5 Comparison signal-to-noise ratio between DAS AND WMS techniques……105

5.5 Conclusion……..108

5.6 References ……..108

Chapter-6 An EC-QCL based dual-species (CH_4 / N_2O) detection method for simultaneous applications of atmospheric monitoring and breath diagnostics……..112

6.1 Introduction……113

6.2 Experimental section…….114

6.3 Results and discussions…….116

6.3.1 Selections of absorption lines…….....116

6.3.2 Optimization of 2f-WMS signal…….....117

6.3.3 Calibration of 2f-WMS signal……110

6.3.4 Allan Variance test……..120

6.3.5 Real time monitoring of CH_4 and N_2O……121

6.4 Conclusion…….....122

6.5 References……...123

Chapter-7 Elucidation of Temperature-Dependent Soil Enzyme Urease Activity and Observation of Deuterium-Enriched Isotopic Resonance Effects ……..127

7.1 Introduction…….127

7.2Results and discussions……..129

7.3 Conclusion…….....134

7.4 Experimental Methods…….....135

7.5 References……..138

Chapter-8 Summary of the thesis and future perspectives……..…..142

8.1 Summary of the thesis…….……..142

8.2 Future perspectives……..…..144

8.2.1 Field specific deployment of 2f-WMS sensor……....…..144

8.2.2 Development of incoherent broadband cavity enhanced spectroscopy …….……..…...145

8.3 References…….....145

Chapter-1

Introduction

Contents

1.1 Background and motivation……1

1.2 Outline of the thesis……3

1.1 Background and motivation

The atmosphere is mainly composed of molecular nitrogen (78.1 %) and oxygen (20.9%), the remaining 1% consists of argon, carbon dioxide and trace gases. The most important greenhouse gases in our earth's atmosphere are water vapour, carbon dioxide (CO_2), methane (CH_4) and nitrous oxide (N_2O) and these gases are present in very low concentrations (trace gases) in our atmosphere Despite their low concentrations in the atmosphere, these gases play a significant role in atmospheric physics and chemistry, particularly in relation to climate change. Unfortunately, human activities such as industrialization, deforestation, and fossil fuel use have led to a rapid increase in the atmospheric concentrations of these trace gases over the past century. This increase in concentration is a major cause for concern as it has direct impacts on human health and the stability of the climate in the long term. Therefore, monitoring these trace gases is crucial in order to gain a better understanding of their impact on our health and the environment, as well as to promote effective measures to mitigate their effects.

Several laser spectroscopic techniques such as tunable diode laser absorption spectroscopy (TDLAS) and Fourier transform infrared spectroscopy (FTIR) are widely used for monitoring of these trace gases and their isotopes. However, the recent

development of quantum cascade laser (QCL) technology with unique features of narrow line-width (~5 MHz), large tuneability (≥100 cm^{-1}) and high-power (~100 mW) paves the way for high-resolution (~0.0003 cm^{-1}) molecular spectroscopy, thus opening a new window for precise measurements of trace gases at a very low concentration up to ppb (parts per billion) and ppt (parts per trillion) levels. The incorporation of mode-hop-free (MHF) continuous wave (cw)-QCL with cavity ring-down spectroscopy (CRDS) technique where the decay rate of light-trapped in a high-finesse optical cavity and the measured ring-down time being independent of laser intensity fluctuations has given a new way for the high-resolution spectroscopic investigation of various small and complex molecular species and their isotopes that will have enormous applications in environmental and biomedical research.

In this thesis the main goal is to investigate the spectroscopic properties of trace gases and its isotopes subsequently to develop mid-IR continuous wave (cw) QCL based sensor for the real-time measurement of trace gases in atmosphere and in human breath. We have worked on two high-sensitive spectroscopic techniques i.e, cavity ring-down spectroscopy (CRDS) and wavelength modulation spectroscopy (WMS) coupled with an external cavity (EC) cw-QCL working at 5-8 μm. This region has strong absorption features of different atmospheric pollutants and breath bio markers like CH_4, N_2O, NO, OCS and their isotopes. This new generation experimental setup will give us opportunity to study the high-resolution spectroscopic studies of important atmospheric molecules for atmospheric application.

In this thesis we have worked on four important trace gas molecules and their isotopes such as CH_4, N_2O, NO, OCS. Methane (CH_4) is the second most contributing greenhouse gas, which has a global warming potential 25 times higher than carbon dioxide. N_2O is also important to trace molecule in atmospheric science due to its potential in global warming. However, the monitoring of both CH_4 and N_2O in human breath has significance application in biomedical science. Morever,$^{13}CH_4$ is the second most abundant isotopomer of methane and can be traced to identify different sources of CH_4 correctly. Both NO and OCS have potential sources involving biomass burning

and anthropogenic activities in chemical industries. The urea urease kinetics study as D_2O regulator has very wide application in soil environment.

1.2 Outline of the thesis

The thesis has described the spectroscopic study and the wide application of high-sensitive monitoring of trace gases in atmosphere and human exhaled breath. Firstly, we have utilized our lab developed we have developed quantum cascade laser coupled cavity ring down spectrometer for the spectroscopic study of two important isotopes of methane $^{13}CH_4$ and $^{12}CH_2D_2$. Next, we have utilized the multi-pass cell coupled with cw-QCL to develop a gas sensor using wavelength modulation spectroscopy techniques for the simultaneous monitoring of trace gases like NO, N_2O, OCS and CH_4. In the final part of thesis, we investigated the isotopic resonance in urea urease kinetic in soil medium. The thesis has been divided in to several chapters. The first chapter cover the importance of trace gas monitoring and a brief overview of infrared laser absorption spectroscopy.

Chapter 3 describes the high-resolution investigation of $^{13}CH_4$ in the ν_4 band using cavity ring-down spectroscopy. The importance of temperature and pressure-induced spectroscopic parameters of$^{13}CH_4$ has been discussed in this chapter.

Chapter 4 describes the ro-vibrational spectral features and pressure broadening dynamics study of dideutero-methane ($^{12}CH_2D_2$) in the $\nu_9(B_2)$ fundamental band. The experimental parameters have been verified with the PGOPHER simulation parameters of $^{12}CH_2D_2$ in this chapter.

Chapter 5 demonstrates the development of experimental gas sensor for the simultaneous measurement of NO and OCS using multi-pass cell-based wavelength modulation spectroscopy.

Chapter 6 demonstrate the simultaneous detection of dual-species (CH_4 / N_2O) using wavelength modulation spectroscopy for atmospheric monitoring and breath diagnostics applications.

Chapter 7 described the urea urease kinetics in soil medium using high resolution spectroscopy. The isotopic resonance due to presence of D_2O solution in reaction has been discussed in this chapter.

Chapter 8 summarizes all the research work described in the thesis. The future outlook of the research work has also been described in this chapter.

Chapter-2

Importance of trace gas monitoring and an overview of spectroscopic techniques for trace gas monitoring

Contents

2.1 Introduction……..…..6

2.1.1 Importance of trace gas in atmospheric monitoring and in biomedical diagnosis…….…...6

2.1.2 Isotopic analysis and its application……...8

2.2 Fundamental spectroscopy……...10

2.2.1 Introduction to infrared spectroscopy……..13

2.2.2.1 Vibrational spectroscopy…….....13

2.2.2.2 Rotational spectroscopy……..…..17

2.2.2.3 Ro-vibrational spectroscopy……....19

2.3 Line intensity and line strength of spectral line…….21

2.4 Line width and line shape function of spectral line……...23

2.5 Overview of spectroscopy techniques for trace gas analysis…....26

2.5.1 Tunable diode laser absorption spectroscopy (TDLAS) ……26

2.5.2 Fourier transform infrared spectroscopy (FTIR)……..27

2.5.3 Photoacoustic spectroscopy (PAS)…….....27

2.5.4 Cavity enhanced absorption spectroscopy (CEAS)……....28

2.5.5 Wavelength modulation spectroscopy (WMS)…….....29

2.6 References……....30

2.1 Introduction

2.1.1 Importance of trace gas in atmospheric monitoring and in biomedical diagnosis

Trace gas monitoring is the process of measuring and analyzing the concentration of gases present in the atmosphere at low concentrations, typically in the parts-per-billion (ppb) or parts-per-trillion (ppt) range. Trace gas monitoring is an important tool for studying air quality, climate change, and atmospheric chemistry. The concentration of trace gases in the atmosphere can have significant impacts on human health, ecosystems, and climate [1-8].

Trace gas monitoring has a wide range of applications, including air quality monitoring, climate change research, and atmospheric chemistry studies. One of the most important applications of trace gas monitoring is the monitoring of air pollutants, such as nitrogen oxides (NOx), sulfur dioxide (SO_2), and volatile organic compounds (VOCs). These pollutants can have significant impacts on human health and the environment, and trace gas monitoring is an important tool for tracking their concentrations and sources (Table-2.1 and Table-2.2). Trace gas monitoring is also important for studying climate change. Many trace gases, such as carbon dioxide (CO_2), methane (CH_4), and nitrous oxide (N_2O), are greenhouse gases that contribute to the warming of the atmosphere. Trace gas monitoring is used to track changes in the concentration of these gases over time and to identify their sources and sinks.
Moreover, trace molecule detection has gained much more importance in biomedical diagnostics. Several organic and inorganic volatile trace molecules that exhaled during breath can be used as a biomarker for the early detection of several diseases.

This non-invasive method can provide different stage of diseases which help easy diagnosis and the effectiveness of diseases can be tracked by measuring the level of biomarker in patients body over time.

Table-2.1

Typical concentrations of trace gases and their importance [9-15].

Trace gas	**Concentrations ppbv (10^{-9})**	**Importance**
Methane ($^{12}CH_4$)	1500-2000	Greenhouse gas, emitted from fossils fuels
Nitrous oxide (N_2O)	300-340	Greenhouse gas, causes ozone layer depletion
Nitric oxide (NO)	10- 50	lays a vital role in atmospheric chemistry
Ammonia (NH_3)	0.01-50	Produced from fertilizer use
Nitrogen dioxide (NO_2)	0.01-200	Regulates atmospheric chemistry and affect ozone concentrations
Carbon dioxide (CO_2)	350-400	Primary Greenhouse gas
Carbon monoxide (CO)	80-100	Toxic gas produced from combustion of fossil fuels and biomass

Table-2.2

Concentrations of different molecules in human breath linked to different diseases [16-22].

Trace gas	Concentrations in exhaled breath	Diseases/ Conditions
Methane ($^{12}CH_4$)	2-10 ppmv	Intestinal diseases
Nitrous oxide (N_2O)	250-350 ppbv	Nitrification and denitrication process in human body
Nitric oxide (NO)	5-60 ppbv	Asthma, lung cancer
Ammonia (NH_3)	0.05-2 ppmv	Kidney diseases
Carbon dioxide (CO_2)	3-5%	H. Pylori infection in stomach
Hydrogen sulfide (H_2S)	0.2-2 ppmv	Halitosis, Airway diseases

2.1.2 Isotopic analysis and its application

Stable isotope analysis is an important tool in environmental research and the isotopic signature of different molecular species can be used to identify and estimate the global importance of various sources and sinks. Isotopic analysis can be used to identify the sources of pollutants in the environment, such as heavy metals, pesticides, or petroleum hydrocarbons. The isotopic signature of ice cores, ocean can provide information on past climates, and biological processes and ocean chemistry in water. Further, the isotopic composition investigations of atmospheric gases can help understand the role of different greenhouse gases in climate change and also isotope ratio study has some important application in planetary sciences. Again, the change in isotopic signature during various physical, chemical and biological processes linked with different isotopic species can provide a powerful constraint for the overall trace gas budget. Moreover, measurements of $^{13}C/^{12}C$ variations of CO_2 in ocean can give the idea of fractions of fossil fuels absorbed by oceans. Similarly, the isotopic ratio

study has some essential applications in biomedical field. The presence of ^{13}C isotopes of CO_2 can be used for the detection of the Heliobacter Pylori bacterial infection in stomach (Table 2.3).

Table-2.3

Importance of different isotopes linked different molecular species [23-29]

Trace gas	Isotopes	Importance
$^{12}CH_4$	$^{13}CH_4$, CH_3D	$^{12}C/^{13}C$, D/H ratio of CH_4 to study planetary atmosphere and surfaces
H_2O	HDO, D_2O, $H_2{}^{18}O$	Coolant in heavy water nuclear reactor, used to detect leakage in heavy water reactor,
N_2O	$N^{15}NO$ ($^{\alpha}N$), ^{15}NNO ($^{\beta}N$),	Site specific $^{\alpha}N$ or $^{\beta}N$ and $N_2{}^{18}O$
CO_2	$^{13}CO_2$, $C^{18}O^{16}O$	$^{13}C/^{12}C$ ratio used detect H. Pylori infection in stomach, ^{18}O exchange in isotopes is lined to enzymatic activity

The stable isotopic ratio is mathematically written in delta (δ) notation and can be expressed as following manner

$$\delta^{13}R\ (^{0}/_{00}) = [(R_{sample}/R_{standard}) - 1] \times 1000 \qquad (1.1)$$

The $^{0}/_{00}$ (per mil) symbol indicates multiplication by 1000 that enhances the readability of delta values as these values are very small and the standard values of isotopic ratios are different according to different molecules. The detailed tabulation of isotopic ratio standard values is given in Table 2.4

For example, if we write the isotopic ratio for $^{13}C/^{12}C$ of carbon it can be written as follows

$$\delta^{13}C\ (^{0}/_{00}) = [((^{13}C/12C)_{\ sample}/(^{13}C/12C)_{\ standard}) - 1] \times 1000 \qquad (1.2)$$

The above-mentioned equations can be used for other molecules and notation can used according the notation of molecules.

Table 2.4

List of standard value of different isotopic ratio values of commonly used isotopes [30-31].

Isotopes	Isotopic ratios	Standard used	Standard isotopic ratio values
D (^{2}H)	D/H	Vienna Standard Mean Ocean Water (VSMOW)	1.5575×10^{-4}
^{17}O	$^{17}O/^{16}O$	Vienna Standard Mean Ocean Water (VSMOW)	3.799×10^{-4}
^{18}O	$^{18}O/^{16}O$	Vienna Standard Mean Ocean Water (VSMOW)	2.0052×10^{-3}
^{13}C	$^{13}C/^{12}C$	Vienna Pee Dee Belemnite (VPDB)	1.12372×10^{-2}
^{15}N	$^{15}N/^{14}N$	Atmospheric nitrogen (N_2)	3.677×10^{-3}
^{34}S	$^{34}S/^{32}S$	Vienna Canyon Diablo Troilite (VCDT)	4.5005×10^{-2}

2.2 Fundamental spectroscopy

Spectroscopy is a field of science that originated from the study of how matter interacts with electromagnetic energy. When an object is exposed to light, some of it is reflected while the rest is absorbed. The absorbed light energy may be emitted later as light of a different colour or wavelength. Spectroscopy aims to identify the specific energies and amounts of light absorbed and emitted by different substances. Spectrometers, which are optical instruments, produce photographic or printed records of the absorbed and emitted light energies as a series of distinct wavelengths or frequencies. These records, known as spectra, are vital in revealing information

about the atomic and molecular structure of the materials being studied. Spectra offer unique "fingerprints" that are closely linked to different elements and compounds.

In terms of quantum mechanical view, when molecules change their quantum state from lower energy state to higher energy state by absorbing incoming photon. So, the energy difference between the two energy levels can be written in terms of Planck's law

$$\Delta E = E_{upper} - E_{lower} = h\nu$$

In atomic systems, the spectroscopic transitions are caused by changes in electronic configuration, while in molecular systems, internal motions such as rotation, vibration, and nuclear spins are responsible for the transitions. Quantum mechanical models are used to analyze observed spectra, allowing researchers to obtain information about the structure and properties of the molecule, including bond lengths, strengths, and the identities and relative positions of constituent atoms. The molecular orbital energies and symmetries can also be determined. The intensities of the spectral transitions reveal the relative populations of the individual molecular energy levels, and the selection rule determines which levels may be coupled by allowed transitions, providing insight into the symmetry of the molecular electronic wave functions. The energy level pattern observed in the spectra provides information about the thermodynamic properties of the molecules, including enthalpy, entropy, and heat capacity, as well as equilibrium constants for chemical reactions. The spectrum of a particular species provides an absolute indication of its identity.

Many gaseous chemical substances possess powerful fundamental vibrational absorption bands in the mid-infrared (mid-IR) spectral range. The absorption of electromagnetic radiation by these fundamental bands offers distinct characteristics that make them useful for detection purposes. As a result, the mid-IR region is a highly convenient choice for the direct quantitative absorption monitoring of trace molecular species in exhaled breath and atmospheric samples. The absorption cross-section of these fundamental bands in the mid-IR region can be up to several orders of

magnitude higher than the overtone or combination bands that occur in the near-infrared (NIR) region.

An ideal mid-infrared (mid-IR) source should possess certain desirable characteristics to achieve high-quality measurements. These include high optical power, narrow linewidth, single longitudinal mode operation, ease of wavelength tailoring, low noise, high beam quality, low tuning rates, rapid wavelength tunability, environmental stability, long-term consistency, and compactness. However, it is difficult to achieve all these attributes in a real-world mid-IR laser source. Depending on the application, certain properties may be more critical than others in obtaining optimal measurement performance. Therefore, it is important to prioritize the key features based on the specific requirements of the application at hand.

However, quantum cascade lasers (QCLs) [32-34] have emerged as a critical component in mid-infrared (mid-IR) photonics and represent a significant advancement in semiconductor laser technology. Unlike earlier mid-IR semiconductor lasers that relied on inter-band transitions, QCLs operate by exploiting the inter sub-band transitions within a multiple quantum-well structure. This approach provides excellent design flexibility, as the step-like structure of inter sub-band transitions can be tailored to achieve specific emission wavelengths. In recent years, significant progress has been made in developing QCLs that exhibit room-temperature, mode-hop-free tuning, continuous wave operation, single-mode operation, high output power, and extremely narrow linewidths. These advances have opened up new possibilities for highly sensitive monitoring of multiple chemical species in gas samples.

The primary objective of this thesis is to advance the field of mid-infrared spectroscopy using quantum cascade lasers (QCLs) and their application in quantitative trace gas monitoring. This technology has immense potential for various fields such as environmental science, breath research, and calculation of absolute spectroscopic parameters [35-38]. To achieve this objective, this chapter aims to provide a comprehensive introduction to the fundamental principles of molecular

spectroscopy. This will enable a better understanding of infrared spectroscopy and the mechanisms underlying the common spectroscopic detection methods used for monitoring trace atmospheric constituents and human exhaled air. By gaining a deeper insight into the fundamental principles of molecular spectroscopy, we can enhance the effectiveness and efficiency of mid-IR QCL-based spectroscopic techniques for the precise and accurate monitoring of trace gases in various applications.

2.2.1 Introduction to infrared spectroscopy

Infrared (IR) spectroscopy is a technique used to analyze the vibrations of molecular bonds in a sample. It involves measuring the absorption or transmission of infrared radiation by the sample. Infrared radiation lies in the range of the electromagnetic spectrum between visible light and microwaves, with wavelengths ranging from approximately 780 nano meters to 1 millimeter.

Infrared spectroscopy can provide information about the functional groups present in a molecule and the molecular structure. Different functional groups absorb infrared radiation at different frequencies, which produces a unique spectral pattern that can be used to identify the molecule. IR spectroscopy is commonly used in a wide range of fields, including chemistry, biology, materials science, and forensic science. It is particularly useful for analyzing organic compounds, such as drugs, polymers, and proteins. IR spectroscopy is a non-destructive and non-invasive technique, making it a valuable tool for analyzing delicate samples.

2.2.1.1 Vibrational spectroscopy

Molecular vibrations are caused by the displacement of atoms in a molecule relative to each other when exposed to electromagnetic radiation. This movement can result in a change in dipole moment, leading to transitions between quantized vibrational energy levels. Only changes in dipole moment parallel or perpendicular to the line of

symmetry axis cause an infrared-active transition, unlike molecules with a permanent dipole moment. Homonuclear diatomic molecules such as H_2 and N_2 are considered infrared-inactive because they lack the possibility of changing their dipole moment. However, heteronuclear diatomic molecules such as NaBr, HCl, and OH have differences in atomic polarizabilities, resulting in a non-zero permanent dipole moment that oscillates during bond stretching. In polyatomic molecules, each atom's motion can be resolved into components along three Cartesian coordinates, resulting in 3N degrees of freedom of motion including vibrations, translations, and rotations. A polyatomic linear molecule containing N atoms has 3N-5 degrees of freedom (3N-6 for non-linear molecules) that describe its vibration modes [39].

For example, carbonyl sulfide (OCS), having 3 atoms, comprises of degrees of freedom 3N-5 = 4 (being a linear molecule), which means it has 4 normal modes of vibration as depicted in Figure-2.1. Each vibrational mode quantum number is specified in normal mode notation; v_1 and v_2 represent the C-O stretching and the C-S stretching respectively. Whereas v_3 is described the O-C-S bending with degeneracy 2. The frequencies of the fundamental vibrations are given in Table-2.5.

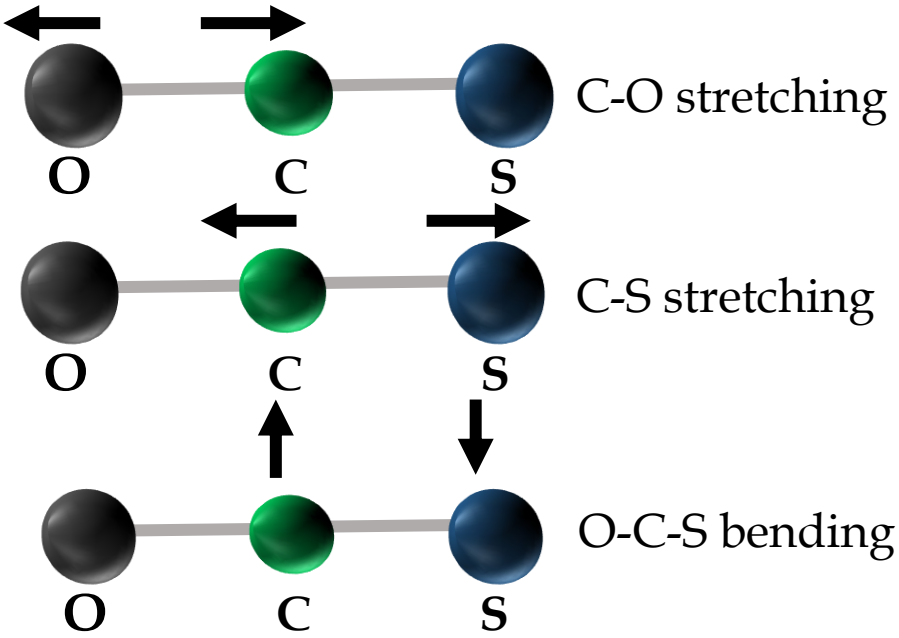

Figure 2.1 - Vibrational modes of OCS molecule

Table 2.5

Tabulations for detailed band type and band origin of OCS molecule

Assignment	Description	Band Origin	IR active
$\mathbf{v_1}$	C-O stretching	2174 cm^{-1}	yes
$\mathbf{v_2}$	C-S stretching	874 cm^{-1}	yes
$\mathbf{v_3}$	O-C-S bending	539 cm^{-1}	yes

Each vibrational mode of a molecule can be described as a unique combination of atomic displacements, and can be modelled as an independent simple harmonic oscillator (SHO). Using the Schrödinger equation, one can determine the allowed energy levels, E_{vib} for each vibrational state of the molecule. So, the Hamiltonian for a particular state with $\Psi(r)$ is the wave function can be expressed as following equation

$$\hat{H}_{vib}\Psi(r) = -\frac{\hbar^2}{2\mu}\frac{d^2\Psi(r)}{dr^2} + V(r)\Psi(r) = E_{vib}\Psi(r) \qquad (2.1)$$

The potential energy function $V(r) = \frac{1}{2}k(r - r_e)^2$ is expressed here [40] as a function of (r - r_e) which is the separation between inter-nuclear and equilibrium separation of bond.

The eigen value can be found by solving the Schrödinger equation and can be expressed as

$$E_\nu = (\nu+\frac{1}{2})h\nu_0 \qquad (2.2)$$

Where ν_0 is the frequency of oscillation and can be written as

$$\nu_0 = \frac{1}{2\pi}\sqrt{\frac{k}{\mu}} \qquad (2.3)$$

Here μ is the reduced mass ($\mu = \frac{m_1 m_2}{m_1+m_2}$) and k is the force constant. ν is the vibrational quantum number which allowed the value of v =0, 1,2 3, …

In spectroscopy, the vibrational energies normally expressed in cm^{-1} which is represented by G and it can be expressed as follows

$$G(\nu) = \frac{Evib}{hc} = (\nu+\frac{1}{2})\,\bar{\upsilon}_0 \ (cm^{-1}) \qquad (2.4)$$

$$\text{Where } \bar{\upsilon}_0 = \frac{1}{2\pi c}\sqrt{\frac{k}{\mu}} \quad (\text{cm}^{-1})$$

From equation 2.4 we can easily see that the minimum energy does not have zero vibrational energy but rather has a zero-point energy G (0) = $\frac{1}{2}\bar{\upsilon}_0$

The selection rules of vibrational transitions are of SHO are $\Delta v = \pm 1$. For a harmonic oscillator with allowed conditions $|\Delta v| > 1$ and that leads to weak overtone transitions which introduces anharmonicity. This anharmonicity arises due to non-harmonic nature of vibrational bonds and therefore the restoring force is no longer proportional to displacement. The anharmonicity can be expressed as Morse potential function

$$V(r) = D_e\left[1 - e^{-\beta(r-r_0}\right]^2 \qquad (2.5)$$

D_e is depth of potential energy known as the dissociation energy and β a constant known as stiffness of small amplitudes near potential minimum.

The solutions of Schrodinger equation in presence of Morse potential can be expressed as

$$G(v) = \left(v + \frac{1}{2}\right)\bar{\upsilon}_0 - \left(v + \frac{1}{2}\right)^2 \bar{\upsilon}_0 x_e \qquad (2.6)$$

Where $x_e = \frac{\bar{\upsilon}_0}{4D_e}$

From the equation (2.6) we can estimate the ground state energy of the molecule and can be expressed as

$$G(0) = \frac{1}{2}\bar{\upsilon}_0\left(1 - \frac{1}{2}x_e\right) \qquad (2.7)$$

For vibrational quantum number changes $\Delta v = \pm 1$ are strongly allowed transitions and transitions with $\Delta v = \pm 2, \pm 3, \ldots$ are weaker transitions.

For strongest transitions $|\Delta v| = 1$ the change in energy can be written as

$$\Delta G = \Delta(v+1) - \Delta(v)$$

$$= \left(v + 1 + \frac{1}{2}\right)\bar{\upsilon}_0 - \left(v + 1 + \frac{1}{2}\right)^2 \bar{\upsilon}_0 x_e - \left(v + \frac{1}{2}\right)\bar{\upsilon}_0 + \left(v + \frac{1}{2}\right)^2 \bar{\upsilon}_0 x_e$$

$$\Delta G = \bar{\upsilon}_0 - 2\bar{\upsilon}_0 x_e(v + 1) \qquad (2.8)$$

Equations (2.8) indicates with increasing in vibrational quantum number, the vibrational energy level are decreased and completely diminished at the dissociation limit as shown in Figure 2.2. Again, the energy associate with transitions can be calculated using

equation (2.8) and transitions like $\nu = 0 \rightarrow 1$ are known as fundamental transitions and transitions like $\nu = 0 \rightarrow 2$, $\nu = 0 \rightarrow 3$ etc are known as overtone transitions. The intensity of the fundamental transitions is stronger as compared to the overtone transitions.

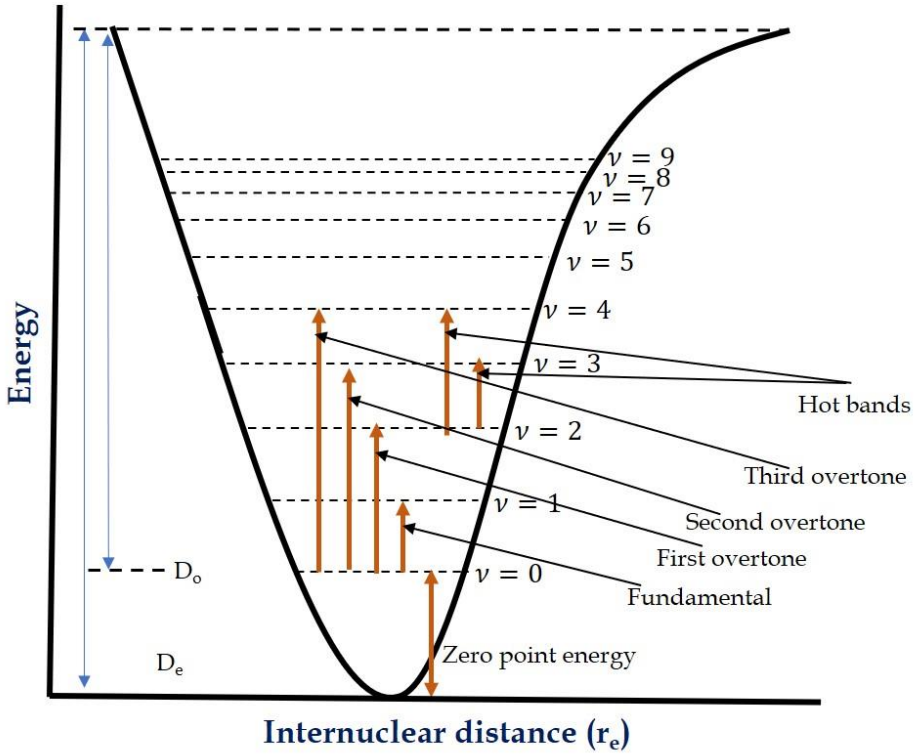

Figure -2.2-Vibrational level and transitions in a Morse potential function

2.2.1.2 Rotational spectroscopy

Rotational spectroscopy provides valuable insights into the structure of molecules, particularly their bond angle and bond length. This is achieved by observing the closely spaced rotational lines that comprise each vibrational energy level, resulting from the interaction between the dipole moment of a rotating molecule and the oscillating electric field of incident infrared (IR) light. A crucial prerequisite for rotational transitions is the presence of a permanent electric dipole moment in the molecule, which varies periodically as the molecule rotates around its centre of gravity. By analyzing the pure rotational transitions observed in the electromagnetic spectrum of the microwave region, valuable information about the structure of the

molecule can be obtained. For a linear polyatomic spherical rotor type molecule, the rotational energy can be expressed as

$$E_{rot} = \frac{h^2}{8\pi^2 I} J(J+1) \text{ [Joule]} \qquad 2.9$$

Further the rotational energy can be expressed as cm^{-1} unit as follows

$$F(J) = \frac{E_J}{hc} = \frac{h}{8\pi^2 Ic} J(J+1) = BJ(J+1) \ (cm^{-1}) \qquad 2.10$$

Where $B = \frac{h}{8\pi^2 Ic}$ known as rotational constant of the molecule and J is the rotational quantum number.

From equation 2.10 we can see that there is systematic increase in spacing in energy level with increase in J value and it happened with a transitional selection rule of $\Delta J = \pm 1$. Where $\Delta J = +1$ corresponds to the absorption of a photon and $\Delta J = -1$ corresponds to emission of a photon.

Further the observed transition energies between two consecutive j levels are given by

$$\begin{aligned} \tilde{\upsilon}_{j\,rot} &= \Delta F(J) = F(J+1) - F(J) \\ &= B[(J+1)(J+2) - J(J+1)] \\ &= 2B(J+1) \end{aligned} \qquad 2.11$$

Next,

$$\begin{aligned} \Delta\tilde{\upsilon}_{j\,rot} = \tilde{\upsilon}_{j\,rot} - \tilde{\upsilon}_{j-1\,rot} &= \Delta F(J) - \Delta F(J-1) \\ &= 2B[(J+1) - J)] \\ &= 2B \end{aligned} \qquad 2.12$$

Therefore, the rotational energy is linearly increasing with J and all lines spaced with a separation of 2B (Figure-2.3) as given in equation 2.12

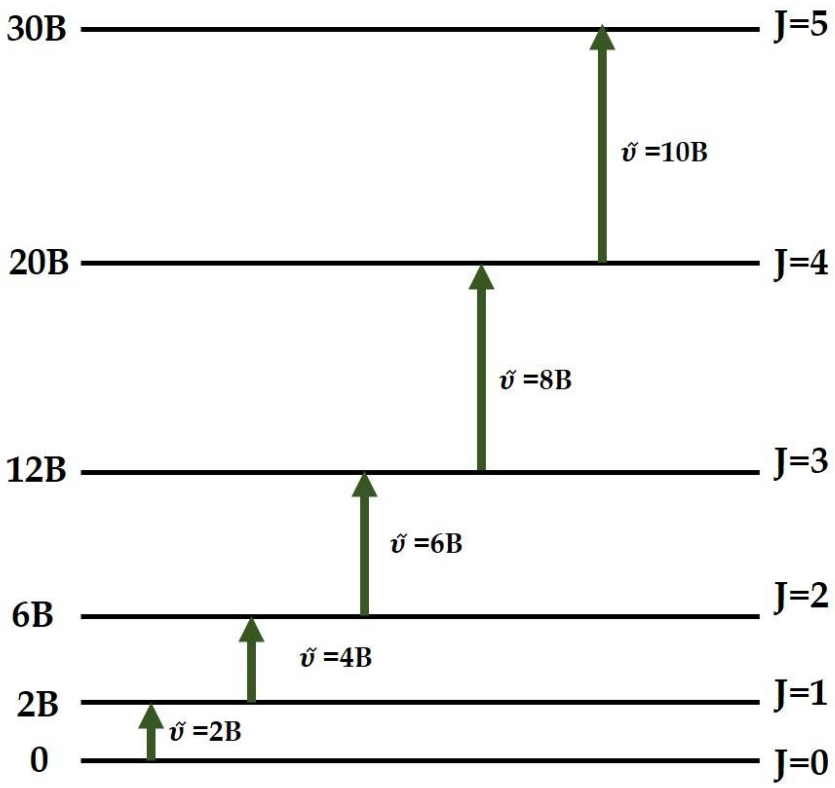

Figure2.3- Rotational energy levels spacing for a linear rigid molecule

In real-world conditions, when a molecule rotates under the influence of electromagnetic (EM) radiation, the centrifugal force causes the distance between its atoms to increase. This leads to an increase in the molecule's moment of inertia, which results in a progressive decrease in the spacing between adjacent rotational energy levels as the value of J increases. Therefore, the rotational energy in presence of centrifugal distortion can be expressed as

$$F_v(J)=B_v[(J(J+1)]-D_v[J(J+1)]^2 \qquad 2.13$$

Here B_v is the vibrational dependence of rotational constant and D_v is the centrifugal distortion constant.

2.2.1.2 Ro-vibrational spectroscopy

In rovibrational spectroscopy molecules undergo rotational transitions with accompany of vibrational transitions. Heteronuclear diatomic molecules in the gas phase have normal modes of vibration that exhibit energy states closely spaced (1-10 cm^{-1} apart) due to accompanying rotational transitions. The change in bond length

during a vibrational transition can affect the rotation of the molecule, leading to the occurrence of rotational transitions. The rotational energy states associated with these transitions can be superimposed upon the vibrational energy states, despite the latter being on the order of 1000 cm^{-1}. So, for a vibrational band transition $\nu' \leftrightarrow \nu''$, composed of lines $\nu'\ J' \leftrightarrow \nu''\ J''$, the rotational- vibrational energy can be expressed as

$$E_{tot} = E_{rot} + E_{vib}$$

$$= B_v\,[(J(J+1)] - D_v[J(J+1)]^2 + \ldots\ldots + \left(\nu + \frac{1}{2}\right)\bar{\upsilon}_0 - \left(\nu + \frac{1}{2}\right)^2 \bar{\upsilon}_0 x_e + \ldots\ldots \quad (2.14)$$

The combined ro-vibrational spectrum displays different branches based on the position of the lines relative to $\bar{\upsilon}_0$. Lines located on the higher frequency side of $\bar{\upsilon}_0$ are known as R-branch and exhibit a $\Delta J = +1$, whereas those on the lower frequency side are designated as P-branch with a $\Delta J = -1$. In addition, rovibrational transitions with a $\Delta J = 0$ are also possible when the electronic angular momentum of the molecule is non-zero. This condition gives rise to a Q-branch with an energy gap of $\Delta E = \bar{\upsilon}_0$. The presence of these ro-vibrational fundamental bands provides us an opportunity to probe molecular transitions of different molecular species mid-IR (3-25 μm) region also known as molecular fingerprint region. Figure-2.4 shows HITRAN (high-resolution transmission) [41] simulations of different molecular species in the mid-infrared regions and demonstrates the ability to probe different frequency of different molecular species due to different in reduced mass. Thus ro-vibrational spectroscopy is most suited in the mid-IR region for trace gas monitoring due to presence of strong fundamental band of different molecular species.

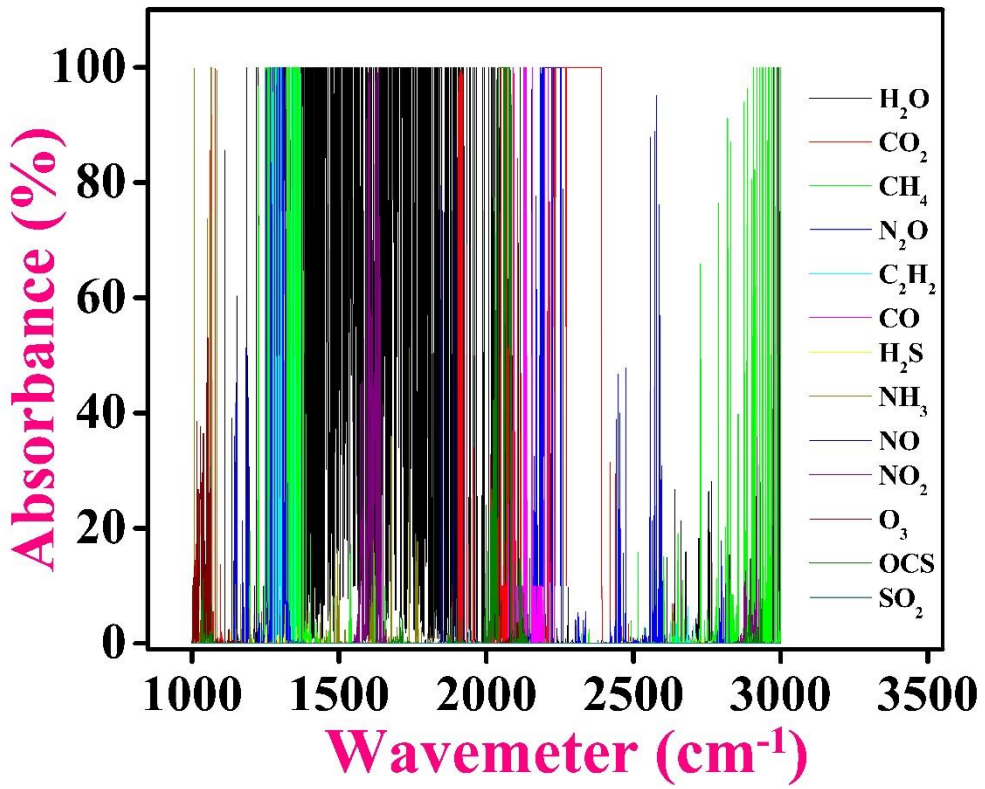

Figure: -2.4 – HITRAN simulations of different molecular species from 1000 cm^{-1} to 3000 cm^{-1} regions.

2.3 Line intensity and line strength of spectral line

The intensity of spectral lines in rovibrational spectra is a measure of the amount of radiation absorbed or emitted during a particular transition. The intensity is proportional to the transition probability, which is determined by the selection rules of the transition and the quantum mechanical properties of the molecule. The population at a particular energy at thermodynamic equilibrium can be expressed in terms of statistical partition function. The probability of a molecular at a specific energy level at thermodynamics equilibrium can be proportional to $g_i e^{\frac{-E_i}{K_B T}}$ where g_i is the total degeneracy of the E_i energy levels, K_B is the Boltzmann constant and T is the temperature. Now, the probability of molecules at energy level E_i can be written as

$$f_i(T) = \frac{g_i e^{\frac{-E_i}{K_B T}}}{\sum_i g_i e^{\frac{-E_i}{K_B T}}} \qquad 2.15$$

The denominator is the molecular partition function which indicates summing over all distinct energy levels E_i.

As we know the degeneracy is given by 2J+1, J is the rotational quantum number and the energy is given by from equation 2.10 is F(J)= BJ(J+1)

Now equation 2.15 can be expressed as

$$f_i(T) = \frac{(2J+1)e^{\frac{-BJ(J+1)}{K_BT}}}{\sum_J (2J+1)e^{\frac{-BJ(J+1)}{K_BT}}} \qquad 2.16$$

The maximum populated rotational level can be expressed as $\frac{d}{dJ} f_J(T) = 0$ and by solving this we can get $J_{max}(T)= \sqrt{\frac{K_BT}{2B_\nu}} - \frac{1}{2}$ which is the most populated level for a given temperature (Figure-2.5).

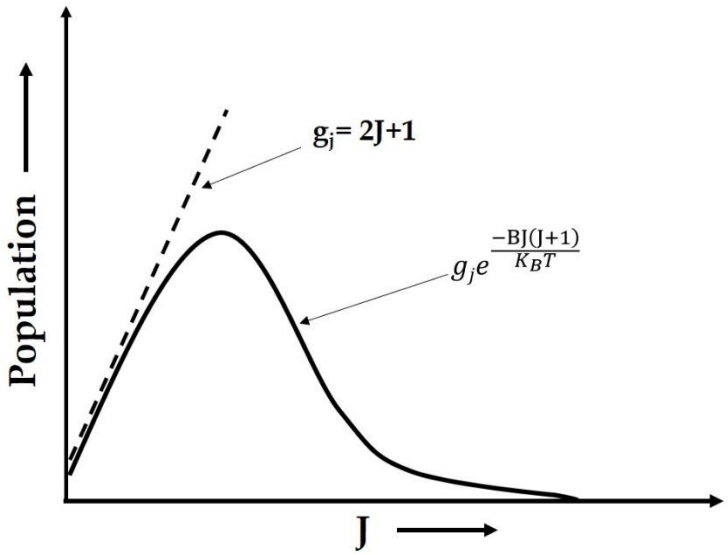

Figure: -2.5 Population distribution of rotating diatomic molecule at 296 K.

The line strength of a spectral line which is used to calculate the concentration of the samples can be demonstrated using Beer-Lambart law equation, $I=I_0 e^{-\alpha d}$ where I and I_0 are the final and initial intensity of light source, d is the path-length of the sample and α is the absorption co-efficient of the sample. However, the spectral absorbance can be obtained from integrated line strength S(T) (cm/molecule) by the following equation

$$\alpha(\nu) = S(T).g(T,P).N.d \qquad 2.17$$

Here g (T, P) is the line shape function and N is sample concentration.

The line strength S (T) can be expressed as the reference temperature T_0 and lower state energy E,

$$S(T) = S(T_0)\frac{Q(T_0)}{Q(T)}\frac{e^{-\frac{hcE}{K_BT}}}{e^{-\frac{hcE}{K_BT_0}}}\frac{\left(1-e^{-\frac{hc\nu_0}{K_BT}}\right)}{\left(1-e^{-\frac{hc\nu_0}{K_BT_0}}\right)} \qquad 2.18$$

Where Q (T) is the partition function at temperature T of the absorbing molecule, h is Planck's constant equal to $6.6260755 \times 10^{-27}$ erg s (1 erg $=10^{-7}$ J), c is speed of light in vacuum equal to $2.99792458 \times 10^{10}$ cm s^{-1}, K is Boltzmann's constant equal to 1.380658×10^{16} erg K^{-1} and ν_0 is the line centre frequency of the spectral transition.

2.4 Line width and line shape function of spectral line

The line width of a spectral line refers to the range of frequencies or wavelengths that are included within the line. A spectral line can have a natural width or a Doppler width. The natural width of a spectral line is caused by the Heisenberg uncertainty principle, which states that it is impossible to know the exact position and momentum of a particle simultaneously. This means that the lifetime of an excited state of an atom or molecule is uncertain, and the energy levels can have a finite width. The natural width of a line is inversely proportional to the lifetime of the excited state.

It is typically represented by the spectral distribution I(ν), where ν is the frequency. The line profile provides valuable information about the properties of the material being studied. The linewidth of a spectral line is a measure of the frequency range over which the intensity of the line is spread. It is defined as the frequency interval $\delta\nu=(\nu_1 - \nu_2)$ between two frequencies ν_1 and ν_2 at which the spectral intensity has decreased to half of its maximum value (Figure-2.6).

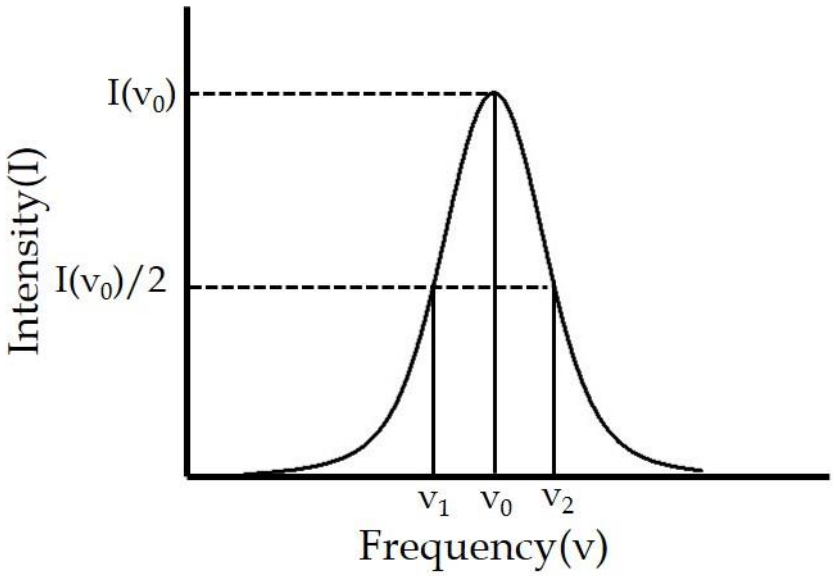

Figure: 2.6- Line shape of spectral line with centre frequency ν_0 and FWHM $\delta\nu = (\nu_1 - \nu_2)$.

When analyzing spectral lines, the Lorentzian profile is commonly used to describe the natural line-profile. However, it is important to note that other broadening effects, such as Doppler broadening and collisional broadening, play a significant role in determining the shape of spectral lines. In fact, these broadening mechanisms are essential for gas-phase measurements. While the Lorentzian profile is a useful model for describing the natural line-profile, it is important to consider the effects of Doppler broadening and collisional broadening when studying spectral lines in a gas phase.

Doppler broadening is mainly happened by the thermal motion of atoms or molecules in a gas. It occurs because atoms and molecules have random velocities that cause them to move towards or away from the observer. This movement leads to a Doppler shift in the frequency of light emitted or absorbed by the atoms or molecules, which in turn leads to a broadening of the spectral lines. The Doppler shift in frequency is given by the equation $\delta\nu/\nu = v/c$, where $\delta\nu$ is the change in frequency, ν is the original frequency, v is the velocity of the atom or molecule, and c is the speed of light. The Doppler broadening of a spectral line depends on the velocity distribution of the emitting or absorbing species in the gas. The Doppler shift can be expressed as Gaussian profile with FWHW [42].

$$\delta\nu=\frac{2\nu}{C}\left(\sqrt{\frac{2K_BTln2}{m}}\right)^{\frac{1}{2}} \qquad 2.19$$

where ν is the transition frequency, m is the mass of the molecule, T is the temperature, k is the Boltzmann constant and c is the speed of the light. The width of a spectral line broadened by Doppler effect has calculated using the Maxwell-Boltzmann distribution of velocity. From equation 2.19, it can be observed that the width of the spectral line is proportional to the temperature of the gas in which the line is formed. This is because at higher temperatures, the molecules in the gas have a wider range of velocities, leading to a broader distribution of Doppler shifts in the emitted or absorbed photons, which results in a broader spectral line.

Again, collisional broadening is another type of spectral line broadening, in addition to Doppler broadening, that occurs due to the interaction of the emitting or absorbing species with other particles in the gas. As the emitting or absorbing species move through the gas, they collide with other particles, causing the spectral lines to broaden. In general, the width of a collision-broadened spectral line depends on the density and pressure of the gas, as well as the type of particles with which the emitting or absorbing species are colliding. When gas molecules randomly collide with each other, the energy levels are perturbed due to their mutual interaction which shorten the lifetime of the colliding molecules introduces broadening of spectral lines.

If τ is the mean life time between two collisions, the line collisional line width can be written as

$$\delta E=\approx \frac{\hbar}{\tau}$$

When a spectral line is broadened by both Doppler and pressure effects, a Voigt profile should be used to accurately describe the line shape. This is because while Doppler broadening causes a Gaussian profile, pressure broadening leads to a Lorentzian profile. A Voigt profile is a convolution of these two functions, which can accurately capture the line shape in such situations.

2.5 Overview of spectroscopy techniques for trace gas analysis

We already mentioned earlier the importance of trace gas molecules in atmosphere and breath and also the accurate precise measurement of these molecules is important to have a clear idea about their role in the specific requirement. As we know the most common and simple method used for trace gas monitoring is direct absorption spectroscopy (DAS). This method mainly related to Beer-Lambart law [43] and that can be expressed as

$$I=I_0 e^{-\alpha d} \qquad 2.20$$

Where I and I_0 are the final and initial intensity of light source, d is the path-length of the sample and α is the absorption co-efficient of the sample. But the low signal-to-noise ratio due to intensity fluctuations leads to open the door for other different techniques. In this section we will discuss the basic method about different spectroscopic techniques that can be used for the monitoring of trace ga molecule in atmosphere as well as in breath sample.

2.5.1 Tunable diode laser absorption spectroscopy (TDLAS)

Tunable diode laser absorption spectroscopy (TDLAS) is a technique used for the measurement of gas concentrations in breath sample also atmospheric samples [44-49]. It uses a laser source which is coupled to White cell or Herriott cells that tuned to a specific wavelength of light, which is absorbed by the gas molecules being measured. By measuring the amount of light that is absorbed, the concentration of the gas can be determined.

It is highly accurate and precise, allowing for the detection of trace amounts of gases in the parts per billion range. Again, it is non-invasive and non-destructive, meaning that it can be used to measure gas concentrations in situ, without the need to extract samples from the process stream. The main disadvantages of TDLAS fail to recognise low absorption spectra as it unable to measure as low signal in large noise background. But the combination of modulation with the signal can improve the signal-to- noise ration and able to trace low absorption features of overtone and

combination vibrational band. Various authors have worked on these techniques and reported the measured concentrations of trace molecules like NH_3, CO, N_2O, OCS etc in both atmosphere and in human exhaled breath.

2.5.2 Fourier transform infrared spectroscopy (FTIR)

Fourier transform infrared spectroscopy (FTIR) is a powerful analytical technique that is used to obtain the infrared spectrum of absorption or emission of a gas in solid liquid and gas and have various application in the field of chemistry, materials science, biology, and medicine [50-55].

FTIR spectroscopy works by shining infrared radiation onto a sample, which causes its molecules to vibrate at specific frequencies. These vibrations cause changes in the dipole moment of the molecules, which in turn causes the absorption of specific wavelengths of infrared light. The resulting absorption spectrum is unique to the chemical composition of the sample and can be used to identify the compounds present.

The instrument used for FTIR spectroscopy consists of an infrared light source, an interferometer, a sample holder, and a detector. The interferometer is used to split the infrared light into two beams, one of which passes through the sample while the other is used as a reference. The two beams are then recombined, and the resulting interference pattern is detected by the detector. The resulting spectrum is a plot of the intensity of the absorbed infrared radiation as a function of the wavenumber of the light. FTIR cover the wide range of IR and measured the low concentration of the required sample and used for different applications.

2.5.3 Photoacoustic spectroscopy (PAS)

Photoacoustic Spectroscopy (PAS) is a non-invasive and non-destructive analytical technique that has gained significant attention in recent years due to its ability to provide accurate and precise measurements of various types of samples. PAS

combines the benefits of spectroscopy and acoustics to provide a unique method of detection and analysis that can be used in environmental monitoring and biomedical diagnostics [56-60].

PAS is based on the photoacoustic effect, which was first discovered by Alexander Graham Bell [61] in 1880. The instrumentation used in PAS typically includes a light source, a detector, and a signal amplifier. The light source can be a laser, a xenon lamp, or an LED. The detector can be a microphone or a piezoelectric transducer. The signal amplifier is used to amplify the photoacoustic signal. The photoacoustic effect occurs when a sample absorbs light energy and converts it into heat. This heat causes the sample to expand, creating a pressure wave that can be detected acoustically. The magnitude of the pressure wave is proportional to the amount of absorbed light energy, which is related to the concentration of the sample. The photoacoustic signal is typically detected using a microphone or a piezoelectric transducer. The signal can be processed to obtain a spectrum, which provides information about the absorbance of the sample at different wavelengths. However, the limited spectral range, high sampling pressure, sensitivity to environmental noise, complexity in the instrumentation limiting the selectivity and sensitivity in some cases.

2.5.4 Cavity enhanced absorption spectroscopy (CEAS)

Cavity-enhanced absorption spectroscopy (CEAS) is a highly sensitive analytical technique that has gained significant attention in recent years [62-65]. CEAS combines the benefits of cavity-enhanced optics and absorption spectroscopy to provide a unique method of detection and analysis. In CEAS, there is an optical cavity consists of two high reflective mirrors separated by a distance called cavity length. When light is introduced into the cavity, it is reflected back and forth between the mirrors, creating a standing wave pattern. This standing wave pattern can be used to enhance the interaction between the light and the sample, leading to higher sensitivity.

In 1988, O'Keefe and Deacon developed a technique called cavity ring down spectroscopy (CRDS), which is also known as pulsed absorption CRDS [66]. This technique involves measuring the decay time of radiation trapped in an optical

resonator with a high-quality factor. The decay occurs when the injected laser power is rapidly turned off after the laser frequency is actively locked to the cavity length. The cavity consists of two high reflectivity mirrors aligned parallel to each other, which allow for several kilometre path lengths inside the ring-down cavity (RDC). This path length exceeds the performance of multi-pass cell spectroscopy. To characterize the absorption of the intracavity medium, the exponential decay of light leaking out from the CRDS cell is monitored. The absorption spectrum of the target analyte inside the RDC cell is obtained by subtracting the total cavity losses from the empty cavity losses. With the absorption cross-section and line shape parameter, the unknown concentration of the target gas can be easily determined without any further secondary calibration.

The CRDS can further upgraded by injecting laser light slightly in an off-axis alignment into the cavity known as off-axis integrated cavity output spectroscopy (OA-ICOS) which will give better sensitivity with faster response time [67-68]. Broadband cavity ring-down spectroscopy (BB-CRDS) is also a high-sensitive technique used for monitoring of trace gas molecules [69-70]. In this we have utilised the CRDS techniques for the spectroscopic investigation of different isotopes and trace gas monitoring that will be discussed in the coming chapters.

2.5.5 Wavelength modulation spectroscopy (WMS)

Wavelength modulation is a powerful and high-sensitive laser-based detection technique used for trace gas monitoring [71-76]. In this method the laser source is modulated by a high frequency sine wave. When the laser beam passed through the gas cell, the interaction between rapidly modulating wavelength and the nonlinear absorption feature give rise to harmonic components at the detector signal. The output at the detector can be demodulated by using a lock-in-amplifier.

The 2nd harmonics signal is strongly dependent on spectral parameters and gas properties, which enables the inference of gas properties through comparison with spectral simulations. Apart from its sensitivity to gas properties, WMS-2f has several advantages that make it preferable over direct absorption for certain sensing applications. These benefits include greater immunity to background interference,

improved detection sensitivity, and the ability to distinguish between gas species with overlapping absorption spectra. The detailed demonstration and application of WMS techniques have been discussed in chapter-5 and 6.

2.6 References

[1] Rao, Gottipaty N., and Andreas Karpf. "External cavity tunable quantum cascade lasers and their applications to trace gas monitoring." *Applied optics* 50, no. 4 (2011): A100-A115.

[2] Barik, Puspendu, and Manik Pradhan. "Selectivity in trace gas sensing: recent developments, challenges, and future perspectives." *Analyst* (2022).

[3] Hundt, P. Morten, Béla Tuzson, Oleg Aseev, Chang Liu, Philipp Scheidegger, Herbert Looser, Filippos Kapsalidis, Mehran Shahmohammadi, Jérôme Faist, and Lukas Emmenegger. "Multi-species trace gas sensing with dual-wavelength QCLs." *Applied Physics B* 124 (2018): 1-9.

[4] Hodgkinson, Jane, and Ralph P. Tatam. "Optical gas sensing: a review." *Measurement science and technology* 24, no. 1 (2012): 012004.

[5] Galli, I., S. Bartalini, S. Borri, P. Cancio, D. Mazzotti, P. De Natale, and G. Giusfredi. "Molecular gas sensing below parts per trillion: radiocarbon-dioxide optical detection." *Physical Review Letters* 107, no. 27 (2011): 270802.

[6] Xia, Jinbao, Feng Zhu, James Bounds, Eshtar Aluauee, Alexandre Kolomenskii, Qian Dong, Jingliang He, Cain Meadows, Sasa Zhang, and Hans Schuessler. "Spectroscopic trace gas detection in air-based gas mixtures: Some methods and applications for breath analysis and environmental monitoring." *Journal of Applied Physics* 131, no. 22 (2022): 220901.

[7] So, Stephen, Ardalan Amiri Sani, Lin Zhong, Frank Tittel, and Gerard Wysocki. "Laser spectroscopic trace-gas sensor networks for atmospheric monitoring applications." In *ESSA Workshop*, vol. 9. 2009.

[8] Baldocchi, Dennis, Markus Reichstein, Dario Papale, Laurie Koteen, Rodrigo Vargas, Deborah Agarwal, and Robert Cook. "The role of trace gas flux networks in the biogeosciences." *Eos, Transactions American Geophysical Union* 93, no. 23 (2012): 217-218.

[9] de Lacy Costello, B. P. J., M. Ledochowski, and Norman M. Ratcliffe. "The importance of methane breath testing: a review." *Journal of breath research* 7, no. 2 (2013): 024001.

[10] Schulze, E. D., S. Luyssaert, P. Ciais, A. Freibauer, Ivan A. Janssens, Jean-François Soussana, P. Smith et al. "Importance of methane and nitrous oxide for Europe's terrestrial greenhouse-gas balance." *Nature geoscience* 2, no. 12 (2009): 842-850.

[11] Davidson, Eric A. "Sources of nitric oxide and nitrous oxide following wetting of dry soil." *Soil Science Society of America Journal* 56, no. 1 (1992): 95-102.

[12] Behera, Sailesh N., Mukesh Sharma, Viney P. Aneja, and Rajasekhar Balasubramanian. "Ammonia in the atmosphere: a review on emission sources, atmospheric chemistry and deposition on terrestrial bodies." *Environmental Science and Pollution Research* 20 (2013): 8092-8131.

[13] Crutzen, Paul J. "The influence of nitrogen oxides on atmospheric ozone content." *Paul J. Crutzen: A Pioneer on Atmospheric Chemistry and Climate Change in the Anthropocene* (2016): 108-116.

[14] Siegenthaler, U., and Jorge Louis Sarmiento. "Atmospheric carbon dioxide and the ocean." *Nature* 365, no. 6442 (1993): 119-125.

[15] Brenninkmeijer, C. A. M., T. Röckmann, M. Bräunlich, P. Jöckel, and P. Bergamaschi. "Review of progress in isotope studies of atmospheric carbon monoxide." *Chemosphere-Global Change Science* 1, no. 1-3 (1999): 33-52.

[16] Das, Sagnik, and Mrinal Pal. "Non-invasive monitoring of human health by exhaled breath analysis: A comprehensive review." *Journal of The Electrochemical Society* 167, no. 3 (2020): 037562.

[17] Kim, Jae Hak, Eugenia Lin, and Mark Pimentel. "Biomarkers of irritable bowel syndrome." *Journal of neurogastroenterology and motility* 23, no. 1 (2017): 20.

[18] Accorsi, Antonio, Simona Valenti, Anna Barbieri, Giovanni Raffi, and Francesco Violante. "Proposal for single and mixture biological exposure limits for sevoflurane and nitrous oxide at low occupational exposure levels." *International archives of occupational and environmental health* 76 (2003): 129-136.

[19] Escamilla-Gil, Jose M., Mar Fernandez-Nieto, and Nathalie Acevedo. "Understanding the cellular sources of the fractional exhaled nitric oxide (FeNO) and its role as a biomarker of type 2 inflammation in asthma." *BioMed Research International* 2022 (2022).

[20] Davies, Simon J., Patrik Španěl, and David Smith. "Breath analysis of ammonia, volatile organic compounds and deuterated water vapor in chronic kidney disease and during dialysis." *Bioanalysis* 6, no. 6 (2014): 843-857.

[21] Syrjänen, Kari, Matti Eskelinen, Ants Peetsalu, Toomas Sillakivi, Pentti Sipponen, Matti Härkönen, Lea Paloheimo et al. "GastroPanel® biomarker assay: The most comprehensive test for Helicobacter pylori infection and its clinical sequelae. a critical review." *Anticancer Research* 39, no. 3 (2019): 1091-1104.

[22] Feng, Dongliang, Lingling Du, Xiaxia Xing, Chen Wang, Jian Chen, Zhengyou Zhu, Yongtao Tian, and Dachi Yang. "Highly sensitive and selective NiO/WO3 composite nanoparticles in detecting H2S biomarker of halitosis." *ACS sensors* 6, no. 3 (2021): 733-741.

[23] Douglas, Peter MJ, Daniel A. Stolper, John M. Eiler, Alex L. Sessions, Michael Lawson, Yanhua Shuai, Andrew Bishop et al. "Methane clumped isotopes: Progress and potential for a new isotopic tracer." *Organic Geochemistry* 113 (2017): 262-282.

[24] Chanton, Jeffrey P. "The effect of gas transport on the isotope signature of methane in wetlands." *Organic Geochemistry* 36, no. 5 (2005): 753-768.

[25] Schimmelmann, Arndt, Alex L. Sessions, and Maria Mastalerz. "Hydrogen isotopic (D/H) composition of organic matter during diagenesis and thermal maturation." *Annu. Rev. Earth Planet. Sci.* 34 (2006): 501-533.

[26] Sarkar, Arnab, Xianglei Mao, George C-Y. Chan, and Richard E. Russo. "Laser ablation molecular isotopic spectrometry of water for 1D2/1H1 ratio analysis." *Spectrochimica Acta Part B: Atomic Spectroscopy* 88 (2013): 46-53.

[27] Röckmann, Thomas, Jan Kaiser, Carl AM Brenninkmeijer, John N. Crowley, Reinhard Borchers, Willi A. Brand, and Paul J. Crutzen. "Isotopic enrichment of nitrous oxide ($^{15}N^{14}NO$, $^{14}N^{15}NO$, $^{14}N^{14}N^{18}O$) in the stratosphere and in the laboratory." *Journal of Geophysical Research: Atmospheres* 106, no. D10 (2001): 10403-10410.

[28] Bakwin, Peter S., Pieter P. Tans, James WC White, and Robert J. Andres. "Determination of the isotopic ($^{13}C/^{12}C$) discrimination by terrestrial biology from a global network of observations." *Global Biogeochemical Cycles* 12, no. 3 (1998): 555-562.

[29] Som, Suman, Anulekha De, Gourab Dutta Banik, Abhijit Maity, Chiranjit Ghosh, Mithun Pal, Sunil B. Daschakraborty, Sujit Chaudhuri, Subhra Jana, and Manik Pradhan. "Mechanisms linking metabolism of Helicobacter pylori to ^{18}O and ^{13}C-isotopes of human breath CO_2." *Scientific Reports* 5, no. 1 (2015): 10936.

[30] Kendall, Carol, and Eric A. Caldwell. "Fundamentals of isotope geochemistry." In *Isotope tracers in catchment hydrology*, pp. 51-86. Elsevier, 1998.

[31] Sharp, Zachary. "Principles of stable isotope geochemistry." (2017).

[32] Maithani, Sanchi, Abhijit Maity, and Manik Pradhan. "Quantum cascade laser spectroscopy for atmospheric sensing and biomedical diagnostics." In *Advances in Spectroscopy: Molecules to Materials: Proceedings of NCASMM 2018*, pp. 67-82. Springer Singapore, 2019.

[33] Li, J. S., W. Chen, and H. Fischer. "Quantum cascade laser spectrometry techniques: a new trend in atmospheric chemistry." *Applied Spectroscopy Reviews* 48, no. 7 (2013): 523-559.

[34] Zhang, Lizhu, Guang Tian, Jingsong Li, and Benli Yu. "Applications of absorption spectroscopy using quantum cascade lasers." *Applied spectroscopy* 68, no. 10 (2014): 1095-1107.

[35] Tuzson, Bela, Rebecca V. Hiller, Kerstin Zeyer, Werner Eugster, Albrecht Neftel, Christof Ammann, and Lukas Emmenegger. "Field intercomparison of two optical analyzers for CH_4 eddy covariance flux measurements." *Atmospheric Measurement Techniques* 3, no. 6 (2010): 1519-1531.

[36] Santoni, Gregory W., Ben H. Lee, Jordan P. Goodrich, Ruth K. Varner, Patrick M. Crill, J. Barry McManus, David D. Nelson, Mark S. Zahniser, and Steven C. Wofsy. "Mass fluxes and isofluxes of methane (CH_4) at a New Hampshire fen measured by a continuous wave quantum cascade laser spectrometer." *Journal of Geophysical Research: Atmospheres* 117, no. D10 (2012).

[37] Kosterev, A. A., R. F. Curl, F. K. Tittel, C. Gmachl, F. Capasso, D. L. Sivco, J. N. Baillargeon, A. L. Hutchinson, and A. Y. Cho. "Methane concentration and isotopic composition measurements with a mid-infrared quantum-cascade laser." *Optics letters* 24, no. 23 (1999): 1762-1764.

[38] Webster, Christopher R., Gregory J. Flesch, David C. Scott, James E. Swanson, Randy D. May, W. Stephen Woodward, Claire Gmachl et al. "Quantum-cascade laser measurements of stratospheric methane and nitrous oxide." *Applied Optics* 40, no. 3 (2001): 321-32.

[39] Steinfeld, Jeffrey I. *Molecules and radiation: An introduction to modern molecular spectroscopy*. Courier Corporation, 2012.

[40] Banwell, Colin N., and Elaine M. McCash. *Fundamentals of molecular spectroscopy*. Indian Edition, 2017.

[41] Gordon, Iouli E., Laurence S. Rothman, Christian Hill, Roman V. Kochanov, Y. Tan, Peter F. Bernath, Manfred Birk et al. "The HITRAN2016 molecular spectroscopic database." *Journal of Quantitative Spectroscopy and Radiative Transfer* 203 (2017): 3-69.

[42] Atkins, P. W., and J. D. Paula. "physical chemistry (7th) Oxford University press." (2002).

[43] Hardesty, Jon H., and Bassam Attili. "Spectrophotometry and the Beer-Lambert Law: An important analytical technique in chemistry." *Collin College, Department of Chemistry* (2010).

[44] Lackner, Maximilian. "Tunable diode laser absorption spectroscopy (TDLAS) in the process industries–a review." *Reviews in Chemical Engineering* 23, no. 2 (2007): 65-147.

[45] Schiff, H. I., G. I. Mackay, and J. Bechara. "The use of tunable diode laser absorption spectroscopy for atmospheric measurements." *Research on chemical intermediates* 20 (1994): 525-556.

[46] Werle, P. O., R. Mücke, and F. Slemr. "The limits of signal averaging in atmospheric trace-gas monitoring by tunable diode-laser absorption spectroscopy (TDLAS)." *Applied Physics B* 57 (1993): 131-139.

[47] Werle, P. "Tunable diode laser absorption spectroscopy: recent findings and novel approaches." *Infrared physics & technology* 37, no. 1 (1996): 59-66.

[48] Nelson, D. D., M. S. Zahniser, J. B. McManus, C. E. Kolb, and J. L. Jimenez. "A tunable diode laser system for the remote sensing of on-road vehicle emissions." *Applied Physics B: Lasers & Optics* 67, no. 4 (1998).

[49] Kouznetsov, Andrian I., and Eugene V. Stepanov. "Applications of tunable diode laser spectroscopy for the detection of exhaled endogenous gases: CO, NH_3, CH_4, N_2O, and CO_2." In *Biomedical Sensing, Imaging, and Tracking Technologies I*, vol. 2676, pp. 272-282. SPIE, 1996.

[50] Smith, Brian C. *Fundamentals of Fourier transform infrared spectroscopy*. CRC press, 2011.

[51] Dutta, Aastha. "Fourier transform infrared spectroscopy." *Spectroscopic methods for nanomaterials characterization* (2017): 73-93.

[52] Berzina-Cimdina, Liga, and Natalija Borodajenko. "Research of calcium phosphates using Fourier transform infrared spectroscopy." *Infrared spectroscopy-materials science, engineering and technology* 12, no. 7 (2012): 251-263.

[53] Weiss, Pierre, Mieczyslaw Lapkowski, Raquel Z. Legeros, Jean-Michel Bouler, Alain Jean, and Guy Daculsi. "Fourier-transform infrared spectroscopy study of

an organic–mineral composite for bone and dental substitute materials." *Journal of Materials Science: Materials in Medicine* 8, no. 10 (1997): 621-629.

[54] Baker, Matthew J., Júlio Trevisan, Paul Bassan, Rohit Bhargava, Holly J. Butler, Konrad M. Dorling, Peter R. Fielden et al. "Using Fourier transform IR spectroscopy to analyze biological materials." *Nature protocols* 9, no. 8 (2014): 1771-1791.

[55] Movasaghi, Zanyar, Shazza Rehman, and Dr Ihtesham ur Rehman. "Fourier transform infrared (FTIR) spectroscopy of biological tissues." *Applied Spectroscopy Reviews* 43, no. 2 (2008): 134-179.

[56] Kistenev, Yury V., Alexey V. Borisov, Dmitry A. Kuzmin, Olga V. Penkova, Nadezhda Y. Kostyukova, and Alexey A. Karapuzikov. "Exhaled air analysis using wideband wave number tuning range infrared laser photoacoustic spectroscopy." *Journal of Biomedical Optics* 22, no. 1 (2017): 017002-017002.

[57] Chandrasekharan, Nirmala, Benjamin Gonzales, and Brian M. Cullum. "Non-resonant multiphoton photoacoustic spectroscopy for noninvasive subsurface chemical diagnostics." *Applied spectroscopy* 58, no. 11 (2004): 1325-1333.

[58] Sampaolo, Angelo, Pietro Patimisco, Marilena Giglio, Andrea Zifarelli, Hongpeng Wu, Lei Dong, and Vincenzo Spagnolo. "Quartz-enhanced photoacoustic spectroscopy for multi-gas detection: A review." *Analytica Chimica Acta* 1202 (2022): 338894.

[59] Aloraynan, Abdulrahman, Shazzad Rassel, Chao Xu, and Dayan Ban. "A single wavelength mid-infrared photoacoustic spectroscopy for noninvasive glucose detection using machine learning." *Biosensors* 12, no. 3 (2022): 166.

[60] Shang, Zhijin, Shangzhi Li, Biao Li, Hongpeng Wu, Angelo Sampaolo, Pietro Patimisco, Vincenzo Spagnolo, and Lei Dong. "Quartz-enhanced photoacoustic

NH3 sensor exploiting a large-prong-spacing quartz tuning fork and an optical fiber amplifier for biomedical applications." *Photoacoustics* 26 (2022): 100363.

[61] Hutt, Dan. "Alexander Graham Bell's optical disc and other inventions." (1996).

[62] Romanini, Daniele, Irène Ventrillard, Guillaume Méjean, Jérôme Morville, and Erik Kerstel. "Introduction to cavity enhanced absorption spectroscopy." *Cavity-Enhanced Spectroscopy and Sensing* (2014): 1-60.

[63] Maity, Abhijit, Sanchi Maithani, and Manik Pradhan. "Cavity ring-down spectroscopy: recent technological advancements, techniques, and applications." *Analytical Chemistry* 93, no. 1 (2020): 388-416.

[64] Maithani, Sanchi, Abhijit Maity, and Manik Pradhan. "A perspective on the evolving role of stable isotope analysis and the emergence of cavity enhanced spectroscopy as a potent tool." *Journal of Analytical Atomic Spectrometry* 36, no. 9 (2021): 1813-1825.

[65] Singh, Dheeraj Kumar, Manik Pradhan, and Arnulf Materny. *Modern Techniques of Spectroscopy*. Springer Singapore, 2021.

[66] O'Keefe, Anthony, and David AG Deacon. "Cavity ring-down optical spectrometer for absorption measurements using pulsed laser sources." *Review of scientific instruments* 59, no. 12 (1988): 2544-2551.

[67] Rambo, Joshua, Chun-Ta Lai, James Farlin, Matt Schroeder, and Ken Bible. "On-site calibration for high precision measurements of water vapor isotope ratios using off-axis cavity-enhanced absorption spectroscopy." *Journal of Atmospheric and Oceanic Technology* 28, no. 11 (2011): 1448-1457.

[68] Liu, Xin, Guangzhen Gao, Xiong Yu, Zhenwei Gao, and Tingdong Cai. "Development of an off-axis cavity-enhanced absorption spectroscopy system

with open-path configuration for gas sensing." *Infrared Physics & Technology* 114 (2021): 103654.

[69] Fiedler, Sven E., Achim Hese, and Albert A. Ruth. "Incoherent broad-band cavity-enhanced absorption spectroscopy." *Chemical physics letters* 371, no. 3-4 (2003): 284-294.

[70] Ball, Stephen M., Justin M. Langridge, and Roderic L. Jones. "Broadband cavity enhanced absorption spectroscopy using light emitting diodes." *Chemical Physics Letters* 398, no. 1-3 (2004): 68-74.

[71] Supplee, James M., Edward A. Whittaker, and Wilfried Lenth. "Theoretical description of frequency modulation and wavelength modulation spectroscopy." *Applied Optics* 33, no. 27 (1994): 6294-6302.

[72] Schilt, Stephane, Luc Thevenaz, and Philippe Robert. "Wavelength modulation spectroscopy: combined frequency and intensity laser modulation." *Applied optics* 42, no. 33 (2003): 6728-6738.

[73] Song, Kyuseok, and Euo Chang Jung. "Recent developments in modulation spectroscopy for trace gas detection using tunable diode lasers." *Applied Spectroscopy Reviews* 38, no. 4 (2003): 395-432.

[74] Maity, Abhijit, Mithun Pal, Sanchi Maithani, Gourab Dutta Banik, and Manik Pradhan. "Wavelength modulation spectroscopy coupled with an external-cavity quantum cascade laser operating between 7.5 and 8 μm." *Laser Physics Letters* 15, no. 4 (2018): 045701.

[75] Ren, Wei, Wenzhe Jiang, and Frank K. Tittel. "Single-QCL-based absorption sensor for simultaneous trace-gas detection of CH_4 and N_2O." *Applied Physics B* 117 (2014): 245-251. Zhu, Cunguang, Pengpeng Wang, Tongwei Chu, Feng Peng, and Yongjie Sun. "Second harmonic phase angle method based on WMS for background-free gas detection." *IEEE Photonics Journal* 13, no. 5 (2021): 1-6.

[76] Xia, Jinbao, Feng Zhu, James Bounds, Eshtar Aluauee, Alexandre Kolomenskii, Qian Dong, Jingliang He, Cain Meadows, Sasa Zhang, and Hans Schuessler. "Spectroscopic trace gas detection in air-based gas mixtures: Some methods and applications for breath analysis and environmental monitoring." *Journal of Applied Physics* 131, no. 22 (2022): 220901.

[77] Zhu, Cunguang, Pengpeng Wang, Tongwei Chu, Feng Peng, and Yongjie Sun. "Second harmonic phase angle method based on WMS for background-free gas detection." *IEEE Photonics Journal* 13, no. 5 (2021): 1-6.

Chapter-3

High-resolution investigations of temperature and pressure-induced spectroscopic $^{13}CH_4$ using cavity ring-down spectroscopy

Contents

3.1 Introduction……42

3.2 Basic principles of CRDS technique……44

3.3 Quantum cascade laser as a mid-IR laser source ……..…46

3.4 Experimental setup……47

3.5 Results and discussion……...…48

3.5.1 Interference-free transition lines ……..……...48

3.5.2 Line-intensity measurements……...…...49

3.5.3 Air-broadening coefficients at room temperature……...…53

3.5.4 Temperature dependence of broadening coefficients…….56

3.6 Conclusion……60

3.7 References……60

3.1 Introduction

Methane (CH_4) is the simplest prototypical hydrocarbon found in Jovian planets' terrestrial and extra-terrestrial atmosphere and their satellites [1-3]. This molecule provides valuable information on atmospheric chemistry and the ecology of planets and exoplanets [4-5]. In the Earth's atmosphere, CH_4 is a trace constituent with a relative concentration of a few parts per million (ppm) by volume. However, the atmospheric lifetime of about three years of CH_4 makes it the second most contributor to the greenhouse effect. In addition, it plays a critical role in stratospheric ozone chemistry [6]. Hence, different space and ground-based missions are continuously tracking the footprints of CH_4 and interpreting the thermal infrared signals.

Nevertheless, it is also essential to identify the natural and anthropogenic sources and sinks of CH_4 and its stable isotopomers to understand the atmospheric methane cycle better. It is noteworthy that $^{13}CH_4$ is the second most abundant isotopomer of methane and can be traced to identify different sources of CH_4 correctly. The ^{13}C-isotopomer of CH_4 is usually found to be depleted in biogenic sources and enriched in concentrations for combustion and fossil fuel sources relative to the atmospheric concentration [7]. Therefore, there is an immense significance of accurate measurement of the concentration of $^{13}CH_4$ isotopomer, which eventually necessitates the precise knowledge of different spectroscopic line parameters associated with the stable ^{13}C-isotopomer of CH_4.

Methane is a highly symmetric molecule around the central carbon atom (C) with a tetrahedral structure. Hence, the change in the isotope of carbon atoms (i.e., ^{12}C or ^{13}C) does not alter Td's symmetry and point group. Therefore, $^{13}CH_4$ also possesses nine vibrational degrees of freedom corresponding to four fundamental modes, i.e., $\nu_1(A_1)$, $\nu_2(E)$, $\nu_3(F_2)$, and $\nu_4(F_2)$ in which $\nu_1(A_1)$ [non-degenerate] and $\nu_3(F_2)$ [triply-degenerate] corresponds to CH stretching vibrations, whereas $\nu_2(E)$ [doubly-degenerate] and $\nu_4(F_2)$ [triply-degenerate] represent bending vibrations. However, only $\nu_3(F_2)$ and $\nu_4(F_2)$ fundamental modes centered around 3020 cm^{-1} and 1301 cm^{-1}, respectively, are infrared active and hence are the prime targets for atmospheric sensing and interpreting infrared thermal images of extra-terrestrial objects. During the past

decades, several theoretical and experimental studies were carried out to investigate the $\nu_4(F_2)$ fundamental bands of $^{12}CH_4$ with various spectroscopic techniques such as Fourier Transform Infrared Spectroscopy (FTIR) and Tunable diode laser absorption spectroscopy (TDLAS) [8-11]. However, the high-resolution spectroscopic analysis in the ν_4 fundamental band of $^{13}CH_4$ is minimal, and the database is still far from complete [12-14]. The database is updated regularly, revising the old values and incorporating new data for missing lines. The study's primary aim was to obtain accurate and high-resolution measurements of various spectroscopic parameters for individual rotational lines in the ν_4 band of $^{13}CH_4$ with (A, E, F) symmetry species at 7.5 µm. In addition, the temperature dependence of broadening coefficients of $^{13}CH_4$ transitions in the $\nu_4(F_2)$ band is mainly unexplored and thus requires experimental investigation to obtain a reliable set of spectroscopic data at elevated temperatures. These are essential for revalidation and further development of the database for application to remote sensing of the Earth and planetary atmospheres for the different conditions.

Nevertheless, a low abundance of ^{13}C-isotope (i.e., ^{13}C:^{12}C≈1:99) necessitates high-sensitive and high-resolution experimental investigations of the transition lines of $^{13}CH_4$ in the presence of the most robust signature of the ^{12}C-isotope of methane. It is also essential to study the interference-free transition lines of $^{13}CH_4$ for accurate atmospheric sensing. The recent development of quantum cascade laser (QCL) technology with unique features of narrow line width (~5 MHz), large tuneability (≥100 cm^{-1}), and high-power (~100 mW) pave the way for high- resolution (~0.0003 cm^{-1}) spectroscopic exploration of molecular species in the mid-infrared (mid-IR) "finger-print" spectral region [15-17]. In addition, cavity ring-down spectroscopy (CRDS) coupled with QCL has emerged as an optical cavity-enhanced absorption technique for high-sensitive and high-resolution spectroscopic studies of low abundant heavier isotopomers like $^{13}CH_4$ [18-22].

In this chapter, we have discussed the experimental study of the $\nu_4(F_2)$ fundamental band of $^{13}CH_4$ at around 1301 cm^{-1} and subsequently acquired high-resolution experimental spectra of 22 interference-free transition lines in the P, Q and R- branches

of $^{13}CH_4$ utilizing a widely tunable continuous wave (*CW*) external-cavity (EC)-QCL coupled with CRDS technique. We after that studied symmetry-specific different spectroscopic line parameters, i.e., line intensity, pressure broadening coefficient, and temperature dependence of broadening coefficient for complete spectroscopic characterization of the transition lines. This study thus provides the first, more accurate interpretation of high-resolution spectral features of $^{13}CH_4$ with rotational symmetry (A, E, F) for the $\nu_4(F_2)$ fundamental band occurring at 7.5 µm.

3.2 Basic principles of CRDS technique

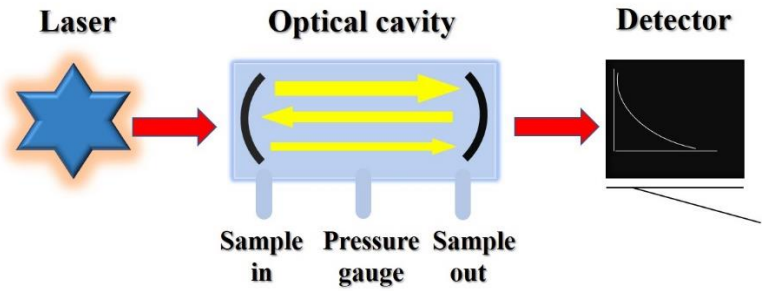

Figure- 3.1 Schematic for the basic principle of CRDS technique.

A CRDS experimental set-up consists of an optical cavity made up of two high-reflective mirrors (R > 99.97). The laser light injected into the cavity and the fraction of the laser beam that is successfully coupled into the cavity makes many passes, with a small amount being transmitted through the mirrors upon each reflection (Fig. 3.1) [23]. The transmission through one of the mirrors is measured using a photosensitive detector and shows an exponential decrease in intensity with time.

The transmitted intensity can be expressed as

$$I=I_0\, e^{\frac{-t}{\tau}} \qquad 3.1$$

Here, I_0 and I are the incident and the output intensities, whereas τ is the time required for the light signal to decay to 1/e of its initial output intensity and is known as the ring-down time. In the absence of a sample inside the cavity, the ring-down time is the empty cavity ring-down time (τ_0). It is a characteristic parameter of the optical

cavity and is related to the mirror reflectivity R and the cavity length L and the speed of light c by the following Equation

$$\tau_0 = \frac{L}{c(1-R)} \qquad 3.2$$

The effective optical pathlength can be expressed as $L_{effective} = \tau_0 c$

For a typical optical cavity with R =0.99988, pathlength, L=0.5 m, empty cavity ring-down time, τ_0= 8.53μs, the effective optical pathlength, $L_{effective}$= 2.6 km can be achieved.

Now when the gas sample present inside the optical cavity the ring-down time (τ) can be expressed as

$$\tau = \frac{L}{c[(1-R)+\alpha d]} \qquad 3.3$$

where α is the absorption coefficient of the sample and d is the sample length which will be equal to L in case of gases which fill the entire cavity. The inverse of τ is known as decay rate (k=1/ τ) which also can be expressed in form of absorption coefficient and concentration [X] of the sample by the following equation

$$\alpha = \frac{\Delta k}{c} = \sigma_\lambda[X] \qquad 3.4$$

where $\Delta k = k - k_0$ is the change in k in the presence and absence of the sample and σ_λ is the wavelength dependent absorption cross-section of the absorbing sample. So, by measuring the decay rate of the sample the concentration of the sample can be measured.

The sensitivity of the CRDS system is generally evaluated as the minimum absorption coefficient α_{min} which is a characteristic parameter of the system and can be calculated by the following equation

$$\alpha_{min} = \frac{1}{c\tau_0}\frac{\Delta\tau_{min}}{\tau_0} \qquad 3.5$$

where $\Delta\tau_{min}$ is the minimum change in τ that can be detected. The range of α_{min} in a typical CRDS system is ~10^{-8}-10^{-9} cm^{-1}. If the absorption cross-section σ_λ for a sample species is known, α_{min} can also be translated to the minimum concentration detection limit for the sample as follows:

$$[X]_{min}=\frac{\alpha_{min}}{\sigma_\lambda} \quad 3.6$$

3.3 Quantum cascade laser as a mid-IR laser source

The Quantum cascade laser (QCL) is a relatively new technology that has revolutionized trace gas analysis in recent years. Its ability to access the entire mid-infrared region, spanning 4-25 μm, is particularly significant as this is considered to be the "molecular fingerprint" region [24-27]. This means that the fundamental and combinational vibrational bands of important trace molecules can be accurately probed with unparalleled molecular selectivity and sensitivity. QCLs are highly versatile and offer several advantages over other laser sources. They can operate at room temperature, have high optical output power, excellent spectral purity, compact size, and provide mode-hop-free broad tunability of over 100 cm^{-1}. Additionally, they possess an extremely narrow linewidth of less than 0.0003 cm^{-1}, making them the preferred laser source for QCL-based absorption spectroscopy (QCLAS) in real-time trace gas monitoring.

Unlike conventional semiconductor lasers, which rely on inter-band transitions between valence and conduction bands to emit wavelength-dependent radiation, quantum cascade lasers (QCLs) use a different mechanism known as inter sub-band transition. In QCLs, only one type of charge carrier, electrons, is involved in the lasing process, making them a unipolar laser source. This sets them apart from traditional bipolar semiconductor lasers. QCLs are typically constructed using a superlattice composed of periodic thin layers with varying material compositions. This results in the formation of an electric potential gradient across the length of the device, creating a one-dimensional multiple quantum well confinement. This confinement splits the energy level into a number of discrete electronic sub-bands, allowing electrons to

cascade down through identical energy steps. At each step, a photon is emitted, resulting in laser emission with high optical power due to population inversion between these discrete conduction band-excited states.

3.4 Experimental setup

All the experimental spectra reported in this study were acquired using the CRDS technique coupled with a CW EC-QCL (Daylight Solutions, USA) operating at around 7.5 μm. A detailed description of the experimental set up was provided elsewhere [18]. The narrow line width ~5MHz of the present CW EC-QCL ensures high-resolution spectral acquisition. The real-time laser wavelength monitoring was achieved by a wavelength-meter (621B-MIR; Bristol Instruments) with an accuracy of ±0.001 cm^{-1}. A high-finesse optical cavity (50 cm length) comprising two high reflectivity mirrors (R>99.98%) at the two ends was utilized for highly sensitive spectroscopic analysis of low-abundant isotopomers of methane in gaseous samples. The optical signal was detected by a thermo-electrically cooled mercury-cadmium-telluride (MCT) detector (PVI-4TE-8-1X1, Vigo Systems S.A.), which was further connected to a high-speed data acquisition card of 100 MHz bandwidth (PCI 5122, National Instruments) for subsequent digitization and analysis of the acquired signal using a custom-written LabVIEW program.

The optical cavity was covered with a thermal jacket to regulate and subsequently maintain the temperature of the cavity with a precession of 0.01°C utilizing a thermocouple and proportional integral derivative (PID) temperature controller. The pressure inside the cavity was monitored using a highly sensitive pressure gauge (Pfeiffer Vacuum), and sample flow into the cavity was controlled by a needle-valve connected to one of the ports of the cavity. In addition, a gas-mixing set up was employed to dilute and subsequently achieve different target concentrations from a standard calibration gas diluting with zero-air (N_2+O_2).

A characteristic empty-cavity ring-down time of τ_0 =8.53 μs with a standard deviation (1σ) of 0.8% was achieved in the present CRDS system for an averaging ten ring-down

events. In our experiment, 350 data points were typically collected for acquiring a single spectral transition, which translates to a total acquisition time of 60 seconds. We obtained the minimum absorption coefficient of $\alpha_{min} = 3.12 \times 10^{-8}$ $cm^{-1,}$ which signifies the detection limit of the present system. The α_{min} value of the present CRDS system ensures the highly sensitive spectral analysis of the isotopomer of $^{13}CH_4$.

3.5 Results and discussion

3.5.1 Interference-free transition lines:

In this study, we focused on the ν_4 fundamental vibrational band of CH_4, which arises from asymmetric bending motion and is centred around 7.5 µm. This spectral region is advantageous for atmospheric sensing applications since it has minimal signatures from water (H_2O) and carbon dioxide (CO_2). However, to study the isotopic composition of CH_4, it is crucial to identify well-resolved transition lines of the individual isotopomer without interference from other molecular species. Monitoring the ^{13}C isotopomer of CH_4 selectively and sensitively is challenging due to the lower mass difference (^{13}C:^{12}C=1.003) and smaller natural abundance (1.1%) of $^{13}CH_4$ compared to the principal $^{12}CH_4$. To identify the transition lines of $^{13}CH_4$ isotopomer that are interference-free and suitable for real-world sensing applications, we first examined the HITRAN database [28] for all the transition lines residing within the mode-hop-free (MHF) tuning range of 1250 -1333 cm^{-1} of our EC-QCL (as shown in Fig. 3.2a). Next, we simulated the spectra under our experimental conditions, including a 2.5 km pathlength, 5 Torr pressure, and 296 K temperature, which helped us identify 22 potential transitions with F, A, and E symmetry of the ^{13}C isotopomer of CH_4. We then probed these spectral features (as shown in Fig. 3.2b) to investigate their different spectroscopic parameters. It's worth noting that these selected transition lines of $^{13}CH_4$ are well-resolved and interference-free, making them suitable for real-world sensing applications with known spectroscopic parameters.

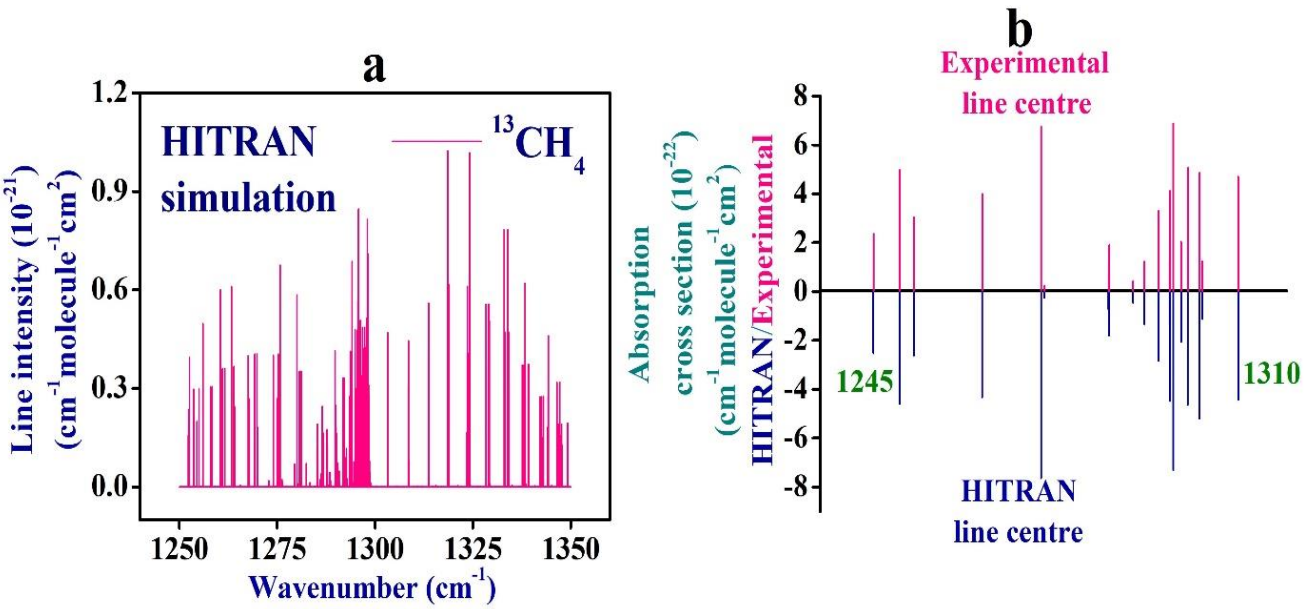

Fig. 3.2 (a) The simulated spectra from the HITRAN database of $^{13}CH_4$ in the 7.5 µm region. (b) Comparison of 22 experimental interference-free spectral lines of $^{13}CH_4$ with HITRAN database value

3.5.2 Line-intensity Measurements

We have obtained experimental absorption features for all selected transitions of $^{13}CH_4$, as illustrated in Figure 3.3. To accomplish this, we used a calibrated gas mixture containing (7.0 ± 0.21) ppm of $^{13}CH_4$, which was sourced from Cambridge Isotope Laboratories Inc. We plotted a change in the ring-down decay rate (Δk) against the corresponding wavenumber to generate the absorption spectrum. To determine the line-intensity of the selected transition lines, we introduced the standard calibrated gas at various pressures into the optical cavity. This allowed us to quantify the strength of the absorption features and obtain a more comprehensive understanding of the molecular properties of $^{13}CH_4$.

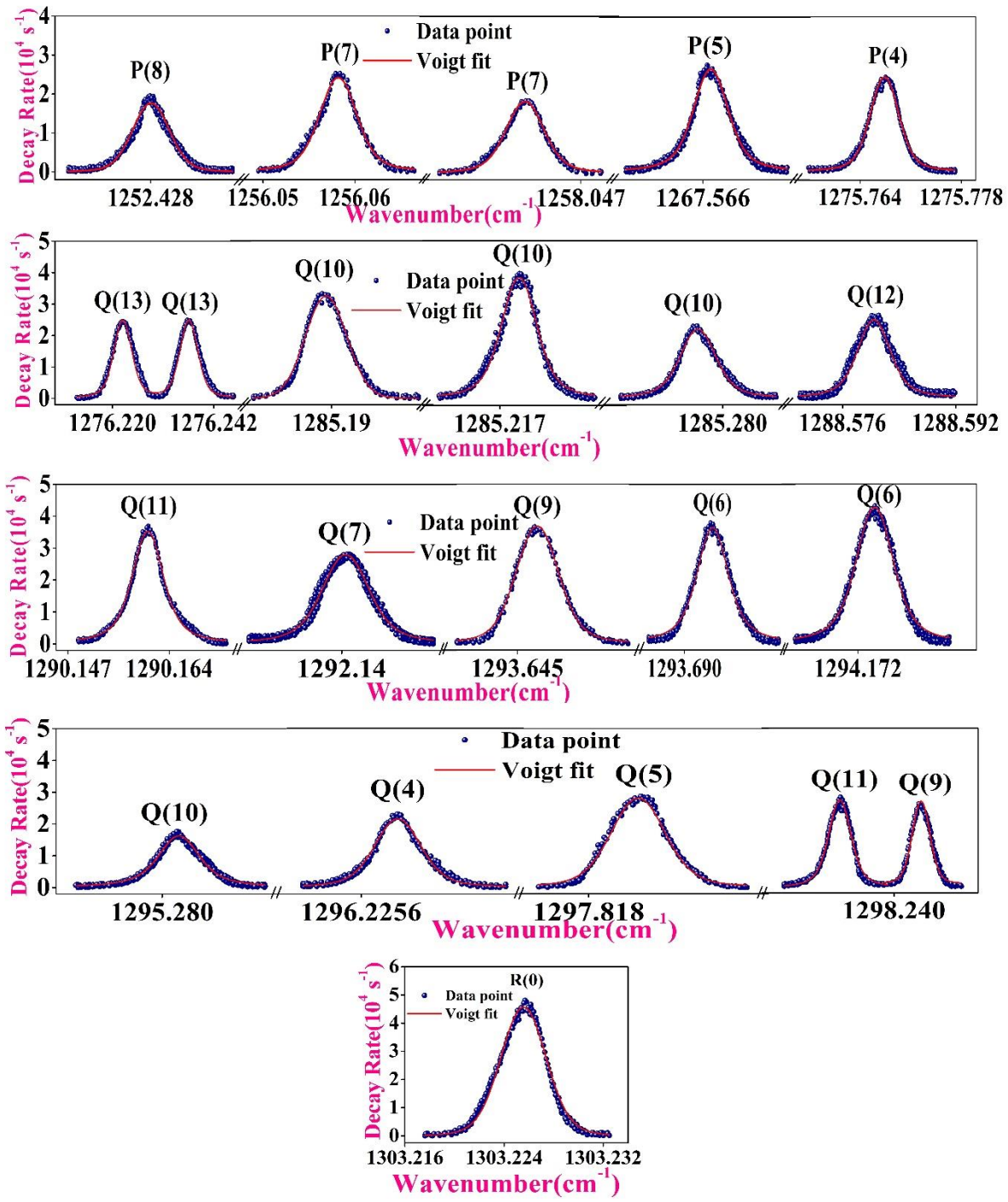

Fig. 3.3 High-resolution CRDS experimental spectral lines of $^{13}CH_4$ in P, Q, and R-branches around 7.5 μm region.

It is important to note that the number of $^{13}CH_4$ molecules present in the optical cavity will vary at different pressures. This variation is reflected in the change of the area of the Voigt-fitted experimental spectra, as shown in Figure 3.4a. To determine the line-intensity of each individual transition line, we calculated the slope of the linear fit

between the fitted areas of the spectra and the pressures within the cavity, as illustrated in Figure 3.4b. We have provided a detailed tabulation in Table 3.1, comparing the experimental values of the line position and line-intensity of all the selected $^{13}CH_4$ transitions with the values from the HITRAN database [28]. This comprehensive comparison allows us to validate our experimental results and gain a deeper understanding of the molecular properties of $^{13}CH_4$.

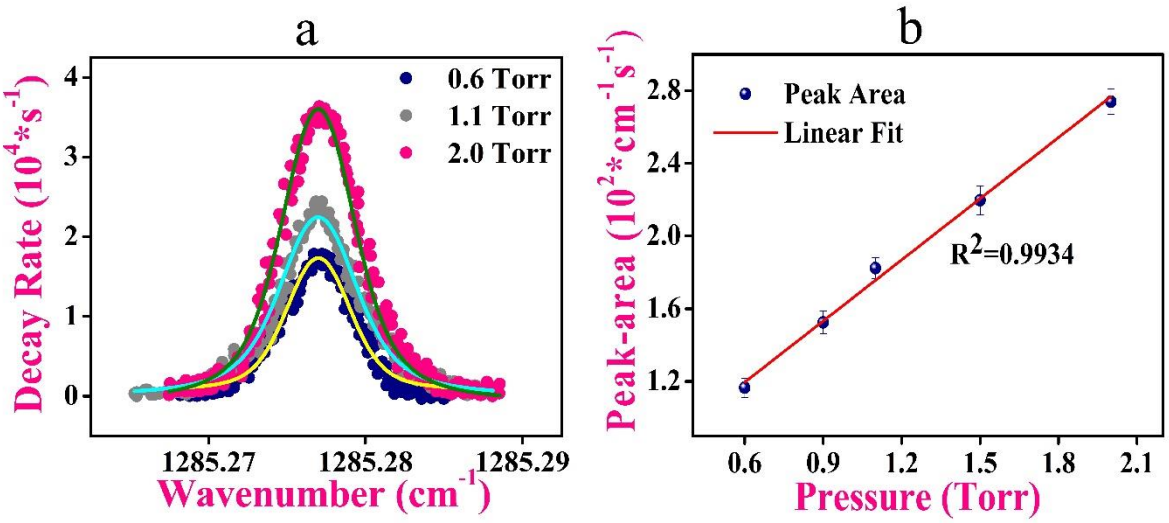

Fig.3.4 (a) CRDS spectra of $^{13}CH_4$ at 1285.2992 cm^{-1} with different concentrations. (b) A graph where pressure is plotted against peak area whose slope is used for calculating absorption cross-section.

Table 3.1. Experimental and simulated spectral lines positions and absorption cross-sections of different transitions of $^{13}CH_4$. All the line centres belong to ν_4 transitions with ground ν' (0,0,0,0) and upper state ν'' (0,0,0,1) parameter in the vibrational symmetry transition $1A_1 \rightarrow 1F_2$. The assignment column is given for P, Q & R branches with the rotational quantum number (J) and symmetry levels (A, E, F).

Peak no	HITRAN Wavenumber centre (cm^{-1})	Experimental Wavenumber centre (cm^{-1})	HITRAN Line-Intensity (cm/molecule) ($*10^{-22}$)	Experimental Line-Intensity (cm/molecule) ($*10^{-22}$)	Assignment
1	1252.4400	1252.424(8)	2.360	2.509±0.03	P8 $F_2 \rightarrow F_1$
2	1256.0713	1256.057(0)	4.978	4.597±0.04	P7 $A_1 \rightarrow A_2$
3	1258.0491	1258.030(1)	3.047	2.623±0.05	P7 $F_1 \rightarrow F_2$
4	1267.5913	1267.571(0)	3.999	4.326±0.04	P5 $F_2 \rightarrow F_1$
5	1275.7792	1275.758(2)	6.755	7.627±0.08	P4 $A_2 \rightarrow A_1$
6	1276.2511	1276.228(0)	0.230	0.2457±0.01	Q13 $F_2 \rightarrow F_1$
7	1276.2620	1276.239(5)	0.230	0.234±0.01	Q13 $F_1 \rightarrow F_2$
8	1285.198	1285.181(3)	0.763	0.723±0.02	Q10 $E \rightarrow E$
9	1285.231	1285.215(9)	1.145	1.120±0.02	Q10 $F_1 \rightarrow F_2$
10	1285.2992	1285.276(2)	1.908	1.805±0.05	Q10 $A_1 \rightarrow A_2$
11	1288.5966	1288.580(2)	0.427	0.4482±0.01	Q12 $F_2 \rightarrow F_1$
12	1290.1828	1290.162(0)	1.226	1.339±0.02	Q11 $A_1 \rightarrow A_2$
13	1292.1564	1292.140(7)	3.305	2.833±0.04	Q7 $F_1 \rightarrow F_2$
14	1293.6683	1293.646(3)	1.196	1.305±0.02	Q9 $E_1 \rightarrow E$

15	1293.7162	1293.701(6)	4.129	4.483±0.04	Q6 $F_1 \rightarrow F_2$
16	1294.1964	1294.182(3)	6.875	7.303±0.05	Q6 $A_1 \rightarrow A_2$
17	1295.3031	1295.285(2)	2.028	2.053±0.02	Q10 $A_2 \rightarrow A_1$
18	1296.2467	1296.227(6)	5.072	4.620±0.04	Q4 $F_2 \rightarrow F_1$
19	1297.8434	1297.821(6)	4.861	5.192±0.04	Q5 $F_2 \rightarrow F_1$
20	1298.2510	1298.229(4)	1.235	1.114±0.02	Q10 $F_1 \rightarrow F_2$
21	1298.2656	1298.245(5)	0.7759	0.674±0.01	Q11 $F_2 \rightarrow F_1$
22	1303.2487	1303.226(7)	4.701	4.427±0.04	R0 $A_2 \rightarrow A_1$

3.5.3 Air-broadening coefficients at room temperature

We conducted an investigation into the impact of air pressure on the spectral lines of $^{13}CH_4$ at room temperature (296K). Specifically, we introduced a specific concentration of $^{13}CH_4$ into the cavity, and then increased the total pressure inside the cavity by sequentially adding zero-air (N_2+O_2). Importantly, we maintained the partial pressure of $^{13}CH_4$ at a low level (around seven ppm) compared to the total pressure to eliminate the self-broadening effect. Our experimental results showed that the absorption spectra became increasingly broadened at higher pressures, resulting in a decrease in peak height as illustrated in Figure 3.5a. However, the total area of the fitted absorption spectra remained constant. We also found that the Lorentzian full-width at half-maximum (FWHM) of the absorption spectra linearly increased with the total pressure inside the optical cavity, as shown in Figure 3.5b. This suggests that the broadening effect on the absorption spectra of the targeted molecular species was due to the presence of foreign molecular species (i.e., zero-air in the present study). We calculated the air broadening coefficient (γ) for each transition of the $^{13}CH_4$ isotope by determining the slope of the linear fit between the Lorentzian FWHM and total pressure. These values are presented in Table 3.2. To examine the potential dependency of air-broadening coefficients on the rotational quantum numbers (J)

associated with each transition, we plotted the variation of the air-broadening coefficient with different m values (where m = J-1, J, and J+1 for P, Q, and R branches, respectively) in Figure 3.5c. These branches are associated with F, A, and E symmetric transitions. Our analysis revealed that the air-broadening coefficient decreased as the J values increased, regardless of the rotational symmetry and branch.

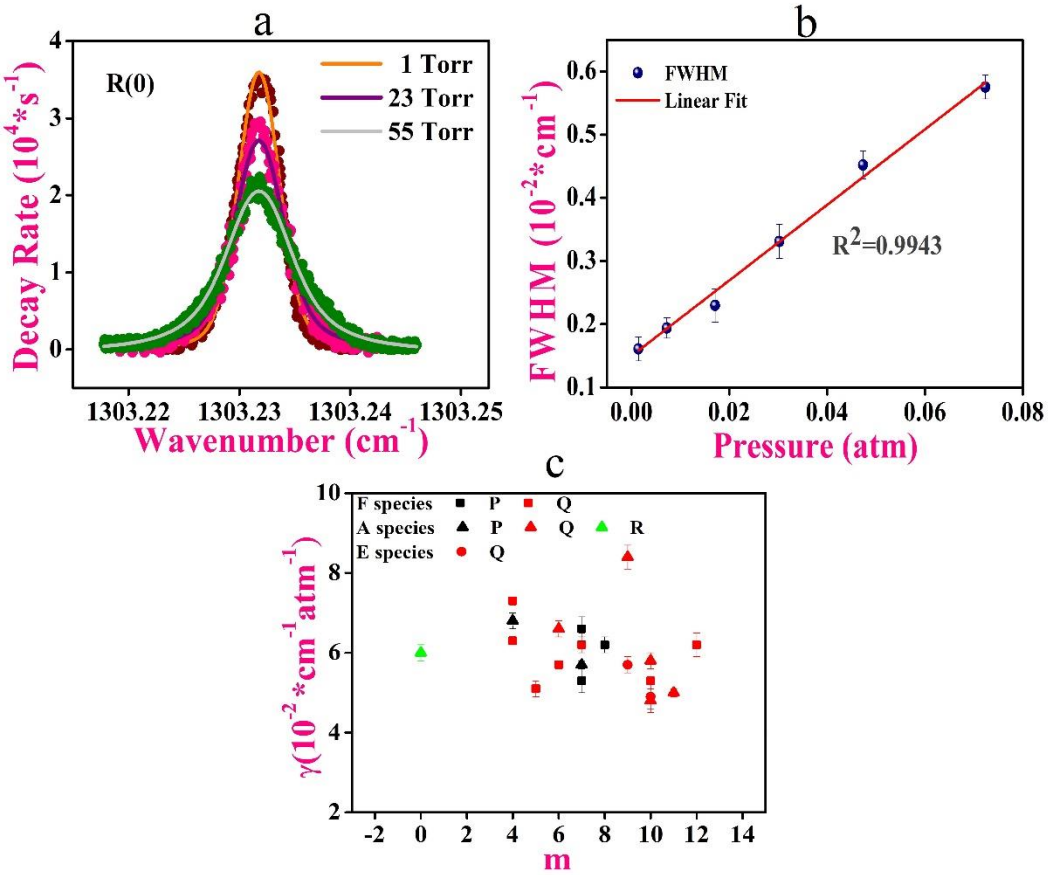

Fig. 3.5 (a) Variation of a particular spectral line in different pressures at 1303.2487 cm^{-1} (b) Linear plot between Lorentzian FWHM of the spectral line and cavity pressures. (c) Variation of measured air-broadened Lorentz halfwidth coefficients as a function of m for F-F, A-A, and E-E transitions.

Table 3.2. Comparison of experimental and HITRAN pressure broadening coefficients of different transition lines of $^{13}CH_4$.

Peak no	**Wavenumber centre (cm^{-1}) (HITRAN)**	Assignment	Pressure broadening coefficient (cm^{-1} atm^{-1}) **(HITRAN)**	Pressure broadening coefficient (cm^{-1} atm^{-1}) **(Experiment)**
1	**1252.4400**	P8 $F_2 \rightarrow F_1$	0.053	0.062±0.002
2	**1255.0351**	P7 $F_1 \rightarrow F_2$	0.061	0.066±0.003
3	**1256.0713**	P7 $A_1 \rightarrow A_2$	0.058	0.057±0.001
4	**1258.0491**	P7 $F_1 \rightarrow F_2$	0.058	0.053±0.003
5	**1275.7792**	P4 $A_2 \rightarrow A_1$	0.061	0.068±0.002
6	**1285.1980**	Q10 E $\rightarrow$ E	0.043	0.049±0.003
7	**1285.2310**	Q10 $F_1 \rightarrow F_2$	0.046	0.053±0.001
8	**1285.2992**	Q10 $A_1 \rightarrow A_2$	0.047	0.058±0.002
9	**1288.5966**	Q12 $F_2 \rightarrow F_1$	0.052	0.062±0.003
10	**1290.1828**	Q11 $A_1 \rightarrow A_2$	0.042	0.050±0.001
11	**1292.1564**	Q7 $F_1 \rightarrow F_2$	0.060	0.062±0.002
12	**1293.6683**	Q9 E $\rightarrow$ E	0.049	0.057±0.002
13	**1293.7162**	Q6 $F_1 \rightarrow F_2$	0.060	0.057±0.001
14	**1294.1964**	Q6 $A_1 \rightarrow A_2$	0.057	0.066±0.002
15	**1295.3031**	Q10 $A_2 \rightarrow A_1$	0.050	0.048±0.003
16	**1296.2467**	Q4 $F_2 \rightarrow F_1$	0.062	0.063±0.001
17	**1297.8434**	Q5 $F_2 \rightarrow F_1$	0.062	0.051±0.002
18	**1297.9141**	Q4 $F_1 \rightarrow F_2$	0.062	0.073±0.001
19	**1298.3925**	Q9 $A_1 \rightarrow A_2$	0.055	0.084±0.003
20	**1303.2487**	R0 $A_2 \rightarrow A_1$	0.053	0.060±0.002

3.5.4 Temperature dependence of broadening coefficients

We finally explored the effect of temperature on the broadening co-efficient (γ) of the selected transitions of $^{13}CH_4$. It is an important spectroscopic parameter to accurately interpret the spectra at high temperatures, such as the extra-terrestrial spectrum. Now, the temperature-dependent of broadening coefficient can be expressed by the relation:

$$\frac{\gamma(T)}{\gamma(T_0)} = \left(\frac{T}{T_0}\right)^{-n} \qquad (3.7)$$

Where $\gamma(T_0)$ and $\gamma(T)$ are the broadening coefficients at the temperature of T_0 and T, respectively, and n denotes the temperature-dependent exponent. In this investigation, we evaluated the air pressure broadening coefficients at three different temperatures, i.e., 296 K, 313 K, and 330 K (Fig. 3.6 a, b, c). It can be found from Fig. 3.6d that the broadening coefficients decreased with the increase in temperature. We calculated the temperature-dependent exponent, n, from the slope of the linear fit between the pressure broadening coefficient and temperature following Equation 3.7.

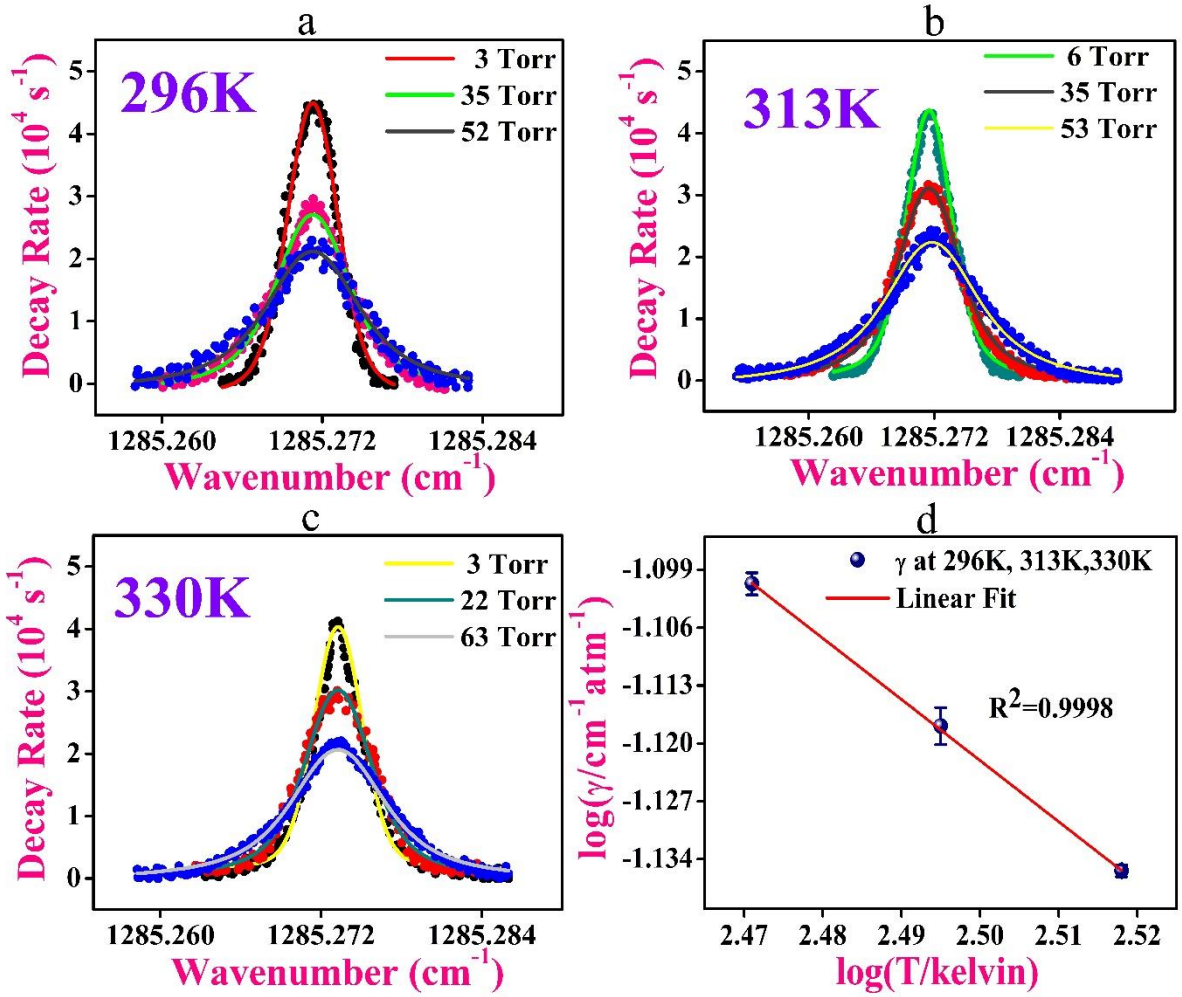

Fig. 3.6 (a), (b), and (c) are the pressure broadening investigation of a line centre at 1285.2992 cm^{-1} at 296 K, 313 K, and 330 K, respectively. (d) Log-log linear temperature plot against pressure broadening coefficients for calculating temperature-dependent exponent.

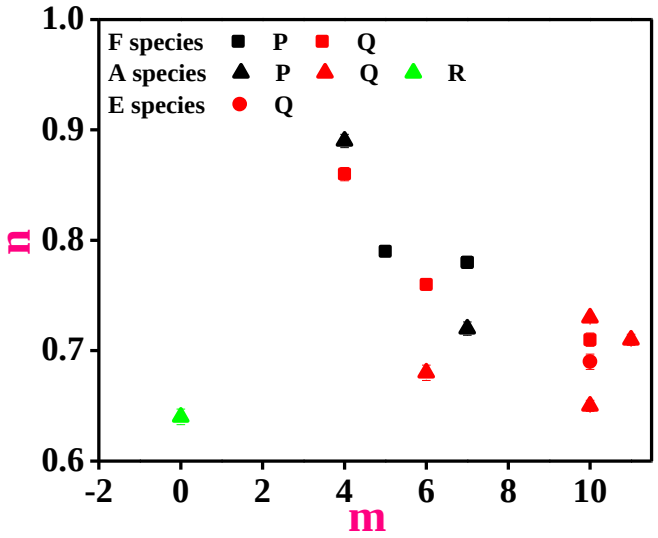

Fig. 3.7 Variation of measured temperature-dependent exponent as a function of m for F-F, A-A, and E-E transitions.

The study also included the tabulation of experimental values of the temperature dependence of broadening coefficients for different transitions of $^{13}CH_4$ in Table 3.3, alongside corresponding HITRAN values. Notably, the HITRAN database provides a single value of temperature-dependent exponent (n) for a particular rotational quantum number, irrespective of the associated symmetries. However, the experimental results revealed symmetry-specific temperature-dependent exponents (n) for each rotational transition. Furthermore, we observed that the temperature-dependent exponent (n) linearly decreased with increasing rotational quantum number, J, and that inter-symmetry variation of n values was noticeable for a particular J value (as shown in Fig. 3.7). Our findings will be invaluable in facilitating more accurate interpretation of ^{13}C-isotopomer features of CH_4.

Table 3.3 Comparison of the experimental and HITRAN online value of temperature dependent exponent of spectra lines.

Peak No	Wavenumber Centre (cm^{-1}) **(HITRAN)**	Assignment	Temperature broadening co-efficient (n) **(Experiment)**	Temperature broadening co-efficient (n) **(HITRAN)**
1	1255.0351	P7 $F_1 \rightarrow F_2$	0.78±0.005	0.73
2	1256.0713	P7 $A_1 \rightarrow A_2$	0.72±0.006	0.73
3	1258.0491	P7 $F_1 \rightarrow F_2$	0.78±0.005	0.73
4	1267.5913	P5 $F_2 \rightarrow F_1$	0.79±0.004	0.75
5	1275.7792	P4 $A_2 \rightarrow A_1$	0.89±0.006	0.80
6	1285.1980	Q10 $E \rightarrow E$	0.69±0.007	0.67
7	1285.2310	Q10 $F_1 \rightarrow F_2$	0.71±0.006	0.67
8	1285.2992	Q10 $A_1 \rightarrow A_2$	0.73±0.003	0.67
9	1290.1828	Q11 $A_1 \rightarrow A_2$	0.71±0.005	0.65
10	1293.7162	Q6 $F_1 \rightarrow F_2$	0.76±0.005	0.72
11	1294.1964	Q6 $A_1 \rightarrow A_2$	0.68±0.007	0.72
12	1295.3031	Q10 $A_2 \rightarrow A_1$	0.65±0.005	0.67
13	1296.2467	Q4 $F_2 \rightarrow F_1$	0.86±0.006	0.80
14	1303.2487	R0 $A_2 \rightarrow A_1$	0.64±0.007	0.63

3.6 Conclusion

We performed a detailed high-resolution spectroscopic study of ν_4 fundamental vibrational band of CH_4 probing 22 interference-free transition lines of ^{13}C-isotopomer using a mid-IR CW-QCL-based CRDS technique at 7.8 µm. We evaluated several important spectroscopic parameters, i.e., line intensity, air-broadening coefficient, and temperature dependence of the broadening coefficient of the transition lines. We also explored symmetry-dependent variation of temperature-dependent exponent (n) for a specific rotational quantum number. Hence, the present study provided all the required spectroscopic parameters of the interference-free transition lines of $^{13}CH_4$ to be exploited for real-world applications.

3.7 References

[1] Varanasi, P., L. P. Giver, and F. P. J. Valero. "Intensity measurements in the ν_4-Fundamental of $^{13}CH_4$ at planetary atmospheric temperatures." *Journal of Quantitative Spectroscopy and Radiative Transfer* 30, no. 6 (1983): 491-495.

[2] Chedin, A., N. Husson, N. A. Scott, and D. Gautier. "ν_4 band of methane ($^{12}CH_4$ and $^{13}CH_4$). Line parameters and evaluation of Jovian atmospheric transmission at 7.7 µm." *Journal of Molecular Spectroscopy* 71, no. 1-3 (1978): 343-368.

[3] Orton, G. S., and A. G. Robiette. "Errata: A line parameter list for the ν_2 and ν_4 bands of $^{12}CH_4$ and $^{13}CH_4$, extended to J′= 25 and its application to planetary atmospheres." *Journal of Quantitative Spectroscopy and Radiative Transfer* 29, no. 3 (1983): 283-284.

[4] Kiseleva, M., J. Mandon, S. Persijn, and F. J. M. Harren. "Accurate measurements of line strengths and air-broadening coefficients in methane

around 1.66 μm using cavity ring down spectroscopy." *Journal of Quantitative Spectroscopy and Radiative Transfer* 224 (2019): 9-17.

[5] Mondelain, D., C. Camy-Peyret, W. Deng, Sébastien Payan, and A. W. Mantz. "Study of molecular line parameters down to very low temperature." *Applied Physics B* 90, no. 2 (2008): 227-233.

[6] Varanasi, Prasad, and Sury Chudamani. "Intensity and line width measurements in the v4 fundamental band of 13CH4." *Journal of Geophysical Research: Atmospheres* 94, no. D8 (1989): 11175-11178.

[7] Townsend-Small, Amy, Stanley C. Tyler, Diane E. Pataki, Xiaomei Xu, and Lance E. Christensen. "Isotopic measurements of atmospheric methane in Los Angeles, California, USA: Influence of "fugitive" fossil fuel emissions." *Journal of Geophysical Research: Atmospheres* 117, no. D7 (2012).

[8] Devi, V. Malathy, Curtis P. Rinsland, Mary Ann H. Smith, and D. Chris Benner. "Air-broadened Lorentz halfwidths and pressure-induced line shifts in the v 4 band of $^{13}CH_4$." *Applied optics* 27, no. 11 (1988): 2296-2308.

[9] Smith, M. A. H., D. Chris Benner, A. Predoi-Cross, and V. Malathy Devi. "Multispectrum analysis of $^{12}CH_4$ in the v_4 spectral region: II. Self-broadened half widths, pressure-induced shifts, temperature dependences and line mixing." *Journal of Quantitative Spectroscopy and Radiative Transfer* 111, no. 9 (2010): 1152-1166.

[10] Frankenberg, Christian, Thorsten Warneke, André Butz, Ilse Aben, Frank Hase, Peter Spietz, and Linda R. Brown. "Pressure broadening in the 2v 3 band of methane and its implication on atmospheric retrievals." *Atmospheric chemistry and physics* 8, no. 17 (2008): 5061-5075.

[11] Devi, V. Malathy, Curtis P. Rinsland, Mary Ann H. Smith, and D. Chris Benner. "Measurements of $^{12}CH_4$ v_4 band halfwidths using a tunable diode laser system

and a Fourier transform spectrometer." *Applied optics* 24, no. 17 (1985): 2788-2791.

[12] Devi, V. Malathy, D. Chris Benner, Mary Ann H. Smith, and Curtis P. Rinsland. "Measurements of air-, N_2-, and O_2-broadened halfwidths and pressure-induced line shifts in the v_3 band of $^{13}CH_4$." *Applied optics* 30, no. 3 (1991): 287-304.

[13] Campargue, A., J. Lopez Segovia, S. Béguier, S. Kassi, and D. Mondelain. "The absorption spectrum of $^{13}CH_4$ in the region of the $2v_3$ band at 1.66 μm: Empirical line lists and temperature dependence." *Journal of Quantitative Spectroscopy and Radiative Transfer* 152 (2015): 140-148.

[14] Gabard, Tony. "Calculated helium-broadened line parameters in the v4 band of 13CH4." *Journal of Quantitative Spectroscopy and Radiative Transfer* 59, no. 3-5 (1998): 287-302.

[15] Faist, Jerome, Federico Capasso, Deborah L. Sivco, Carlo Sirtori, Albert L. Hutchinson, and Alfred Y. Cho. "Quantum cascade laser." *Science* 264, no. 5158 (1994): 553-556.

[16] Totschnig, Gerhard, Franz Winter, V. Pustogov, Jerôme Faist, and Alexander Müller. "Mid-infrared external-cavity quantum-cascade laser." *Optics letters* 27, no. 20 (2002): 1788-1790.

[17] Hugi, Andreas, Richard Maulini, and Jérôme Faist. "External cavity quantum cascade laser." *Semiconductor Science and Technology* 25, no. 8 (2010): 083001.

[18] Maity, Abhijit, Mithun Pal, Gourab Dutta Banik, Sanchi Maithani, and Manik Pradhan. "Cavity ring-down spectroscopy using an EC-QCL operating at 7.5 μm for direct monitoring of methane isotopes in air." *Laser Physics Letters* 14, no. 11 (2017): 115701.

[19] Chen, H., A. Karion, C. W. Rella, Jan Winderlich, Christoph Gerbig, A. Filges, T. Newberger, C. Sweeney, and P. P. Tans. "Accurate measurements of carbon monoxide in humid air using the cavity ring-down spectroscopy (CRDS) technique." *Atmospheric Measurement Techniques Discussions* 5, no. 5 (2012): 6493-6517.

[20] Maithani, Sanchi, Santanu Mandal, Abhijit Maity, Mithun Pal, and Manik Pradhan. "High-resolution spectral analysis of ammonia near 6.2 μm using a cw EC-QCL coupled with cavity ring-down spectroscopy." *Analyst* 143, no. 9 (2018): 2109-2114.

[21] Sumizawa, H., H. Yamada, and K. Tonokura. "Real-time monitoring of nitric oxide in diesel exhaust gas by mid-infrared cavity ring-down spectroscopy." *Applied Physics B* 100 (2010): 925-931.

[22] Banik, Gourab Dutta, Suman Som, Abhijit Maity, Mithun Pal, Sanchi Maithani, Santanu Mandal, and Manik Pradhan. "An EC-QCL based N 2 O sensor at 5.2 μm using cavity ring-down spectroscopy for environmental applications." *Analytical Methods* 9, no. 15 (2017): 2315-2320.

[23] Mazurenka, Mikhail, Andrew J. Orr-Ewing, Robert Peverall, and Grant AD Ritchie. "4 Cavity ring-down and cavity enhanced spectroscopy using diode lasers." *Annual Reports Section" C"(Physical Chemistry)* 101 (2005): 100-142.

[24] Welzel, S., R. Engeln, and J. Röpcke. "Quantum cascade laser based chemical sensing using optically resonant cavities." *Cavity-Enhanced Spectroscopy and Sensing* (2014): 93-142.

[25] Hugi, Andreas, Romain Terazzi, Yargo Bonetti, Andreas Wittmann, Milan Fischer, Mattias Beck, Jérôme Faist, and Emilio Gini. "External cavity quantum cascade laser tunable from 7.6 to 11.4 μ m." *Applied Physics Letters* 95, no. 6 (2009): 061103.

[26] Maithani, Sanchi, Abhijit Maity, and Manik Pradhan. "Quantum cascade laser spectroscopy for atmospheric sensing and biomedical diagnostics." In *Advances in Spectroscopy: Molecules to Materials: Proceedings of NCASMM 2018*, pp. 67-82. Springer Singapore, 2019.

[27] Pal, Mithun, and Manik Pradhan. "Quantum Cascade Laser Spectroscopy." *Modern Techniques of Spectroscopy: Basics, Instrumentation, and Applications* (2021): 363-387.

[28] Hill, Christian, Iouli E. Gordon, Roman V. Kochanov, Lorenzo Barrett, Jonas S. Wilzewski, and Laurence S. Rothman. "HITRANonline: An online interface and the flexible representation of spectroscopic data in the HITRAN database." *Journal of quantitative spectroscopy and radiative transfer* 177 (2016): 4-14.

Chapter-4

Ro-vibrational spectral features and pressure broadening dynamics of dideutero-methane ($^{12}CH_2D_2$) in the $\nu_9(B_2)$ fundamental band

Contents

4.1 Introduction…….…….66

4.2 Experimental section……..…..70

4.3 Results and discussions……..71

4.3.1 High-resolution absorption spectral lines of $^{12}CH_2D_2$….71

4.3.2 Gaussian 16 and PGOPHER simulations……..74

4.3.3 Line intensity measurements of $^{12}CH_2D_2$……..79

4.3.4 Pressure broadening investigations of $^{12}CH_2D_2$……...82

4.3.5 Squared transition moment measurements of $^{12}CH_2D_2$..86

4.4 Conclusion……88

4.5 References…….... 89

4.1 Introduction

Methane (CH_4) is an important prototypical organic molecule and plays a significant role in many research areas, including atmospheric and environmental sciences, reaction kinetics, interstellar chemistry, astrophysics, and combustion science [1-6]. However, the D-substituted isotopomers of methane (CH_3D, CHD_3, CH_2D_2, and CD_4), so-called "clumped isotopes," are distinct from other isotopes in terms of physical and chemical properties and may carry additional information about the various pathways of formation of methane and biochemical cycles in many environments of our solar system [7-11]. Moreover, current interest in exploring the spectroscopy of methane isotopomers in interplanetary missions to Titan and Jupiter has increased significantly [12-15]. In view of different contexts, detailed and accurate knowledge of ro-vibrational levels is required to study high-resolution molecular spectroscopy of methane and its isotopomers. The spectroscopic investigation of deuteromethanes can provide valuable information on the structure and potential hypersurface of methane and its vibrational dynamics-a subject of current spectroscopic interest in the scientific community.

Doubly-deuterated methane ($^{12}CH_2D_2$) is an asymmetric top-type molecule (Fig.4.1) with asymmetry coefficient kappa= -0.27 that is considered one of the most important isotopomers of methane. It is the non-radioactive asymmetric-top isotopomer of methane that belongs to the C_{2v} point group. Because of this, it has received particular interest in molecular spectroscopy and molecular physics. $^{12}CH_2D_2$ has nine non-degenerate vibrational modes, each belonging to one of the four symmetry species A_1, A_2, B_1, and B_2, as shown in Table 4.1 [19]. Normal ro-vibrational spectroscopic study of methane and its isotopomers has always been a difficult and time-consuming task due to strong resonance interactions between the degenerate vibrational states. However, the $^{12}CH_2D_2$ molecule is unique and is free from such difficulties due to its non-degenerate vibrational states. Thus, $^{12}CH_2D_2$ isotopomer contains much more information about the potential surface of methane and its vibrational dynamics from its high-resolution vibrational spectra than the other highly symmetric deuteromethane isotopomers (CH_3D, CHD_3, and CD_4). However, accurately

determining the ro-vibrational infrared (IR) spectral features of $^{12}CH_2D_2$ under the double H→D substitution remains challenging. Further, information on the high-resolution line parameters of $^{12}CH_2D_2$ isotopomer is not yet available in the HITRAN and in other well-known spectroscopic databases [16,17]. The current study thus aims to fill a missing gap for the $^{12}CH_2D_2$ isotopomer of one of the most asymmetric molecules known.

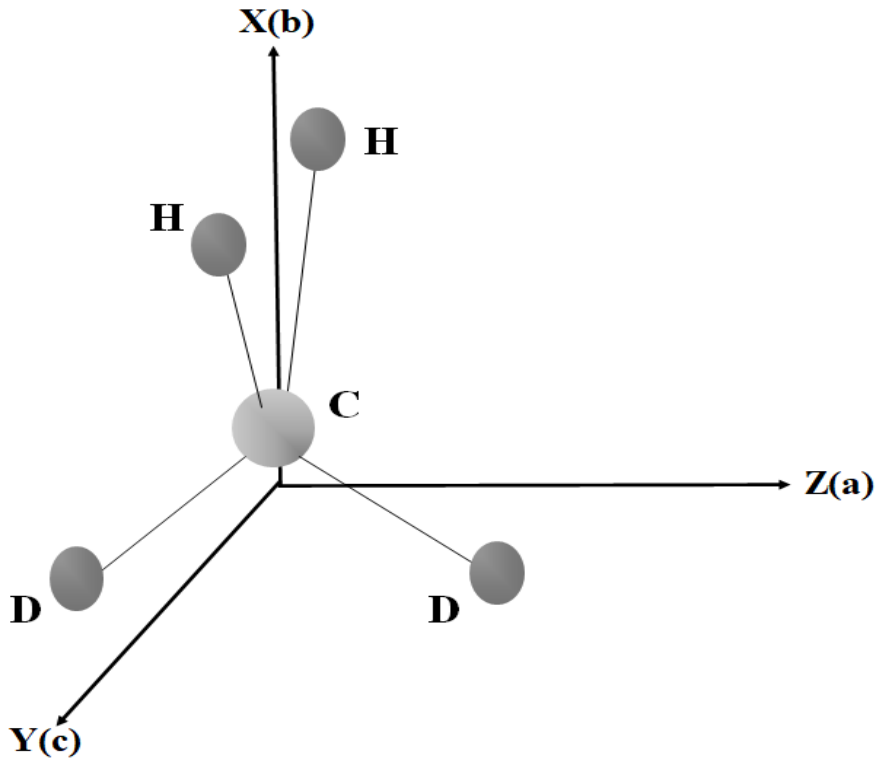

Fig.-4.1. A schematic diagram of CH_2D_2. x, y, and z are the Cartesian axes according to the symmetry group that classifies vibrational modes. a, b and c are the principal axis of rotation for the molecule.

Table 4.1: Tabulation for detailed information about the fundamental bands of $^{12}CH_2D_2$ with symmetry assignment.

Fundamental band	Symmetry species	Band centre (cm^{-1})	Symmetry assignment
ν_1	A_1	2975.4823	CH_2 s-stretching
ν_2	A_1	2203.2171	CD_2 s-stretching
ν_3	A_1	1435.1346	CH_2 s-scissoring
ν_4	A_1	1033.0434	CD_2 s-stretching
ν_5	A_2	1331.4087	CH_2 twisting
ν_6	B_1	3012.2595	CH_2 a-stretching
ν_7	B_1	1091.185	CH_2 s-rocking
ν_8	B_1	2234.6923	CD_2 a-stretching
ν_9	B_2	1236.2771	CH_2 wagging

Over the past decades, many research groups have primarily focused on several theoretical and experimental demonstrations for measuring the ro-vibrational spectra of CH_2D_2 by probing various fundamental, combination, and overtones bands in several spectral regions. Ulenikov and co-workers [18-22], in a series of studies, have carried out a detailed analysis of the IR spectra of CH_2D_2 in various combinations (such as $\nu_3+\nu_4$, $\nu_3+\nu_6$, $\nu_3+\nu_7$, $\nu_4+\nu_9$, $\nu_5+\nu_7$, $\nu_5+\nu_9$, $\nu_7+\nu_9$, etc.) and overtone bands (e. g. $2\nu_3$, $2\nu_4$, $2\nu_7$ and $2\nu_9$) in the range from 1900-6600 cm^{-1} using the Fourier transform spectroscopy. The IR spectra of CH_2D_2 on the various fundamental bands such as ν_3, ν_4, ν_5, ν_6, and ν_7 were also carried by Deroche and co-workers [23-26] with the Fourier-transform spectrometer as well as on the ν_9 fundamental band using an interferential spectrometer with a moderate resolution of 0.015 cm^{-1}. Moreover, from the theoretical side numerous efforts involving quantum dynamics simulations of vibrational spectra of CH_2D_2 have been performed over the years [27-29]. In view of the earlier studies, the detailed experimental demonstration of the high-resolution ro-vibrational spectral features of $^{12}CH_2D_2$ isotopomer, including the precise knowledge of line positions, line

intensities (line strengths), pressure broadening coefficients and transition dipole moments on the ν_9 (B_2 symmetry) fundamental band near 7.8 μm remains largely unexplored. However, there is an analytical challenge for precise and high-resolution measurements of the spectral features of $^{12}CH_2D_2$ isotopomer due to its low fractional abundances. Nevertheless, the recent technological advances of the widely-tunable continuous-wave (*CW*) external-cavity quantum cascade lasers (EC-QCLs) in the mid-IR "fingerprint" region coupled with the ultra-sensitive optical cavity-enhanced techniques such as cavity ring-down spectroscopy (CRDS) have enabled precise and high-resolution measurements of several molecules and their isotopologues at natural abundances [30-32].

In this chapter, we probed the *a*-type ν_9 (B_2-symmetry) fundamental vibrational band of $^{12}CH_2D_2$ isotopomer corresponding to the CH_2-wagging motion and explored the high-resolution ro-vibrational gas-phase spectra of this molecule in the mid-IR region by CRDS technique exploiting a *cw* EC-QCL as an optical light source operating at 7.8 μm. We performed the high-level Gaussian 16 calculations and PGOPHER simulation for accurate determination of various spectroscopic parameters of $^{12}CH_2D_2$ isotopomer with a resolution of 0.001 cm^{-1} in numerous ro-vibrational transitions to the states with rotational quantum number J up to J^{max}=11 covering mostly the R-branch spectral lines for the $\nu_9(B_2)$ vibrational band. We further investigated the pressure-broadening effect of all the probed spectral lines with various foreign gases such as argon (Ar), helium (He), hydrogen mixture (H_2+N_2), nitrogen (N_2), and zero air (Air Liquid, UK) to obtain the information about the interaction ability and adequate pressure required for the measurement of concentrations in various atmospheric conditions. The present study provides the first accurate CRDS measurements of the fine rotationally-resolved spectral features of a prototypical organic molecule like $^{12}CH_2D_2$ isotopomer of methane. Our results may help improve our understanding of methane's vibrational dynamics and potential hypersurface.

4.2 Experimental section

The detailed experimental arrangement and procedure were described elsewhere [30]. In brief, a *CW* EC-QCL (Daylight Solutions, USA) at a centre wavelength ~7.8 μm with a MHF region of 1250-1340 cm^{-1} was used in the present study. The typical line-width of the QC laser source is ~ 0.0003 $cm^{-1,}$ which is highly beneficial for the high-resolution measurements of various spectroscopic parameters. The laser source was coupled with a high-finesse optical cavity (50 cm) and two high-reflective mirrors with a reflectivity of 99.98% (CRD Optics Inc.; USA). A wavemeter (621B-MIR; Bristol Instruments) was utilized to monitor laser frequency with an accuracy of 0.001 cm^{-1}. With the help of piezo electric transducers (PZTs), we modulated the cavity-mode over laser-mode, and the resultant light leaking from the optical cavity was focused to a mercury-cadmium-telluride (MCT) detector (PVI-4TE-8-1X1, Vigo Systems S.A.). A pre-amplifier was used to amplify the output signal, connected to a high-speed data acquisition card of 100 MHz bandwidth (PCI 5122, National Instruments) to analyze the acquired ring-down signal with the custom-made LabVIEW program.

We recorded the typical ring-down time of τ_0=8.53 μs with a standard deviation of 0.8% over averaging 20 ring-down events for this study. Then for recording a single spectral transition, we collected around 400 points with an acquisition time of 90 sec. We can calculate the concentration of the sample from the change in decay rate $\Delta k = c\alpha = \sigma_\lambda [X] c$ where $\Delta k = (1/\tau - 1/\tau_0)$, α is the absorption coefficient of the sample, σ_λ is the wavelength-dependent line intensity, [X] is the concentration of the sample and c is the velocity of light. We calculated the minimum absorption coefficient of α_{min} =3.12 × $10^{-8,}$ which can be translated to a typical detection of 1000 ppbv of $^{12}CH_2D_2$ by using the transition at 1295.1968 cm^{-1} and absorption cross-section of 6.08×10^{-23} cm/molecule at 296K while maintaining a typical pressure of 50 Torr in the optical cavity. However, with consideration of the pressure broadening effect at 1 atm. Pressure, this detection limit would correspond to 77 ppbv.

4.3 Results and discussion

4.3.1 High-resolution absorption spectral lines of $^{12}CH_2D_2$

We have explored the gas-phase fine structure ro-vibrational spectra of $^{12}CH_2D_2$ isotopomer of methane in the $\nu_9(B_2)$ fundamental band corresponding to the CH_2-wagging motion. The ν_9 band with B_2-symmetry is an *a*-type band, and the corresponding transition lines must fulfill the selection rule: $\Delta J = 0, \pm 1$, $\Delta K_A = 0$, and $\Delta K_C = \pm 1$. However, for the presence of weak "forbidden" transitions, it must follow the selection rules: $\Delta J = 0, \pm 1$, $\Delta K_A = \pm(2n)$ and $\Delta K_C = \pm(2m+1)$, where m, n are zero or positive integers. As the line assignments and line positions have already been reported by Deroche and his team (26), we first utilized and reverified the line positions with our experimental setup. Fig. 4.2 shows the high-resolution CRDS spectra of the $^{12}CH_2D_2$ isotopomer of the ν_9 fundamental band. The spectra were recorded by injecting a particular concentration of $^{12}CH_2D_2$ (Cambridge Isotope Laboratories. Inc., USA, 99.99%) of 15000 ppm with zero air (Air Liquid, UK) inside the optical cavity with a pressure range of 0.5-1.0 Torr under the Doppler broadened limiting conditions at room temperature 296K. We recorded the change in decay rate, i.e. inverse of ring-down time (Δk in s^{-1}) against the wavenumber (cm^{-1}) for a particular ro-vibrational transition of $^{12}CH_2D_2$. The CRDS spectra were fitted with the Voigt line-shape profile.

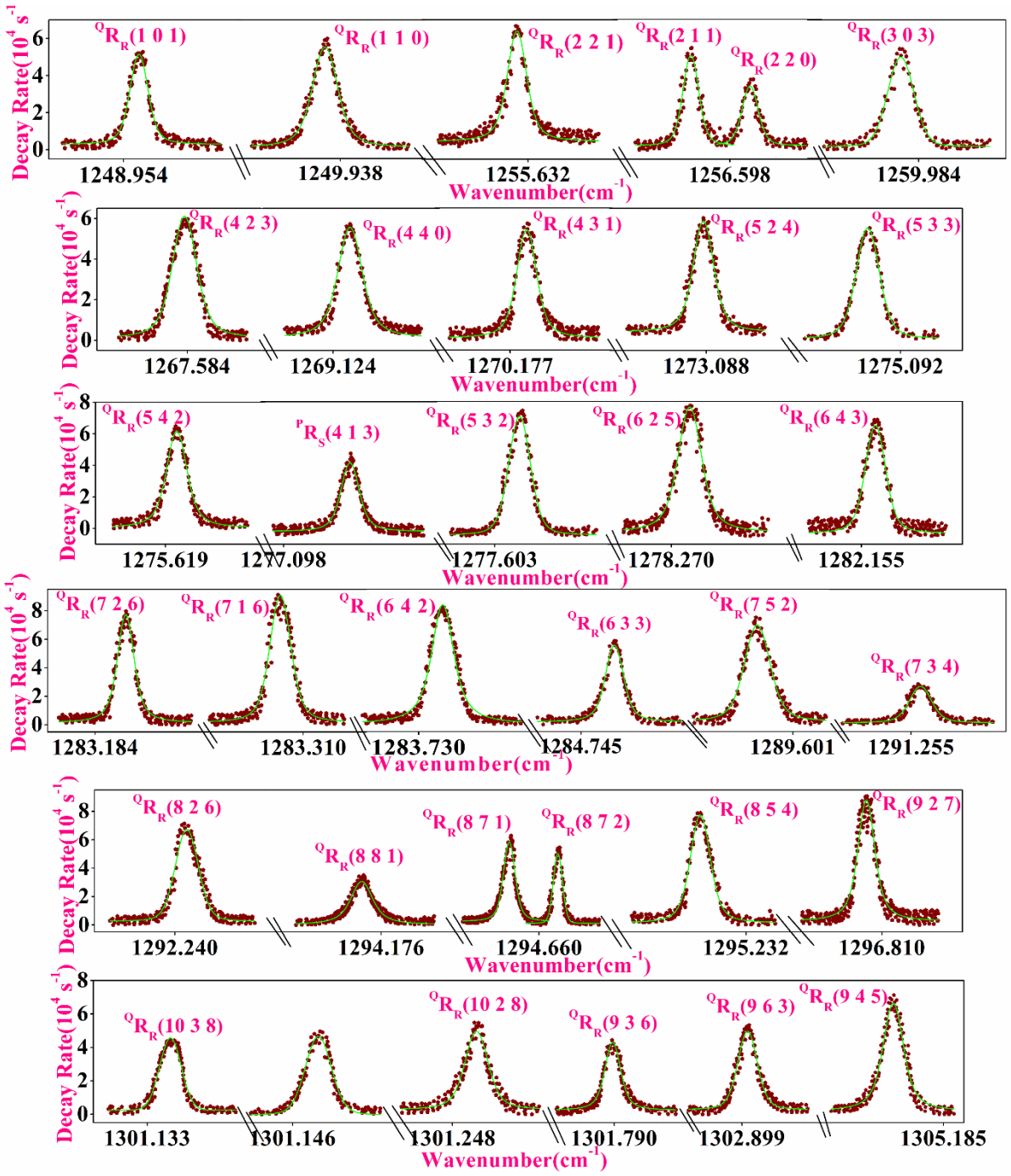

Fig.4.2. High-resolution CRDS experimental spectral lines in the R-branch of CH_2D_2 isotopomer around 7.5 μm. Here, we have given the assignment in the form of $^{\Delta Ka}\Delta J_{\Delta Kc}$ (J″, K_a'', K_c''). J″, K_a'', K_c'' represents the ground state quantum numbers of the respective spectral lines.

In this study, the probed region exhibited the pronounced R-branch ro-vibrational lines where the rotationally-resolved transitions up to J^{max}=11 were observed in the $\nu_9(B_2)$ fundamental band within the tuning range of the QC laser. We have accurately assigned 34 ro-vibrational transitions in the $\nu_9(B_2)$ band with the help of Gaussian 16 and PGOPHER simulation that has been described later on. In this context, a comparison of the HITRAN simulated spectra of the most abundant molecular species, such as water (H_2O), carbon dioxide (CO_2), and "mother" methane ($^{12}CH_4$) molecule with the experimental CRDS spectra of $^{12}CH_2D_2$ isotopomer in the probed spectral region were given in Fig. 4.3. As the information of the line parameters of $^{12}CH_2D_2$ is absent in the HITRAN database, this investigation will be a prime database for future inclusion of $^{12}CH_2D_2$ data therein. Further, the spectroscopic identification of the gas-phase $^{12}CH_2D_2$ spectral lines in the presence of the complicated spectra of several other molecular species, as depicted in Fig. 4.3, makes our study more significant and thus provides a way for selective and precise identification and classification of $^{12}CH_2D_2$ gas-phase spectral features in the interference-free regions.

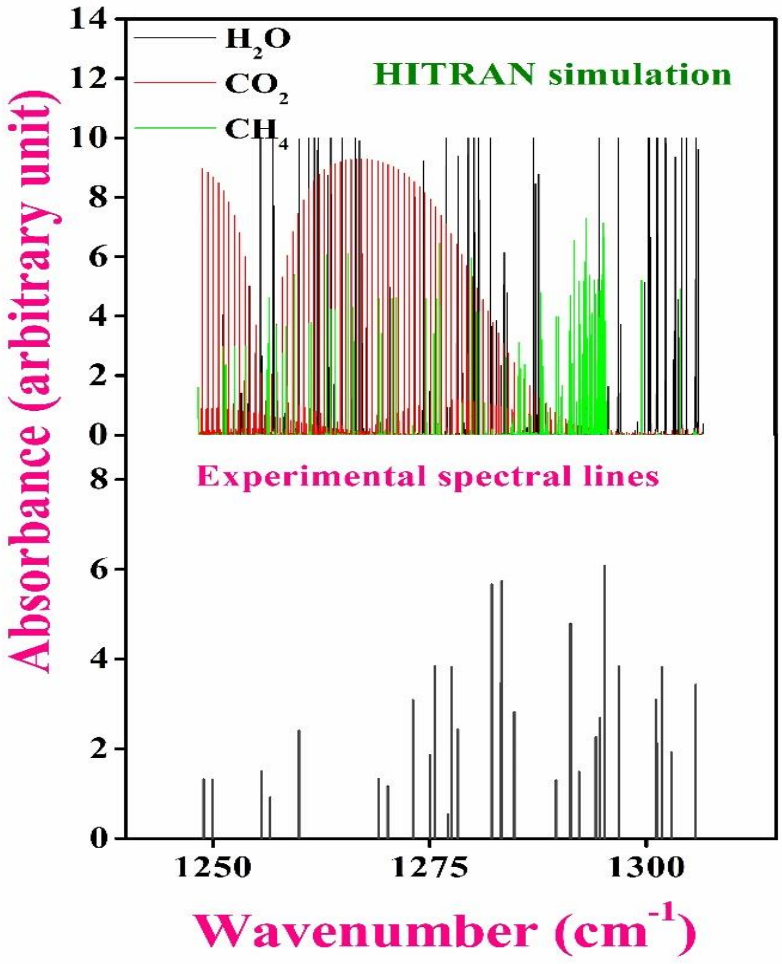

Fig. 4.3. Comparison of the HITRAN simulated spectra of H_2O, CO_2, $^{12}CH_4$ with experimentally obtained CRDS gas-phase spectra of $^{12}CH_2D_2$ isotopomer for proper visualization of the interference-free region.

4.3.2 Gaussian 16 and PGOPHER simulations

Next, in order to verify the experimentally obtained CRDS gas-phase spectra of $^{12}CH_2D_2$ and to theoretically predict the line parameters such as line positions and line-intensities (line strengths) of this molecule, we performed the PGOPHER simulation for an asymmetric-top molecule with symmetry C_{2v} for the $\nu_9(B_2)$ band of $^{12}CH_2D_2$ with band centred at 1236.27 cm^{-1}. We first calculated the various spectroscopic parameters such as rotational constants (A, B, C in cm^{-1}) of the ground and excited states along with dipole moment derivatives (dd_a, dd_b & dd_c in Debye) by the Gaussian 16 using the DFT-RB3YLP (Density Functional Theory-Becke, three-

parameter, Lee-Yang-Parr) method with a basis set of 6-311++G (2df, 2p) as shown in Table 4.2.

Table 4.2

Spectroscopic parameters of CH_2D_2 for the ground state and excited states as calculated using Gaussian 16.

Spectroscopic Parameters	**Calculated Values by Gaussian 16**
Ground state A (cm^{-1})	4.2886
Ground state B (cm^{-1})	3.4934
Ground state C (cm^{-1})	3.0395
Excited state A (cm^{-1})	4.2590
Excited state B (cm^{-1})	3.5491
Excited state C (cm^{-1})	2.9300
Dipole derivative - dd_a (Debye)	0.9468
Dipole derivative - dd_b (Debye)	1.6260
Dipole derivative – dd_c (Debye)	-2.5801
Principal inertia moment - I_A (amu-$Å^2$)	3.8865
Principal inertia moment - I_B (amu-$Å^2$)	4.7684
Principal inertia moment - I_C (amu-$Å^2$)	5.4740

All these spectroscopic parameters were then utilized as an input for the PGOPHER simulation, and subsequently, the least square fitting process was employed for better overlapping of the spectral lines between the simulated and experimental results, thus leading to precise assignments of the line positions. Fig. 4.4 shows the comparison between the simulated PGOPHER and normalized CRDS spectra of the 12CH2D2 isotopomer, and we generally obtained an excellent agreement between them. For the comparison of simulated, experimental, and Deroche-reported lines, a detailed tabulation has been given in Table 4.3. We also utilized the experimental and theoretical values of the line strengths of various spectral transitions to make a ratio-plot with respect to the line positions as shown in Fig. 4.5, which gave a better overview of the comparison of the spectral parameters with minimum deviation.

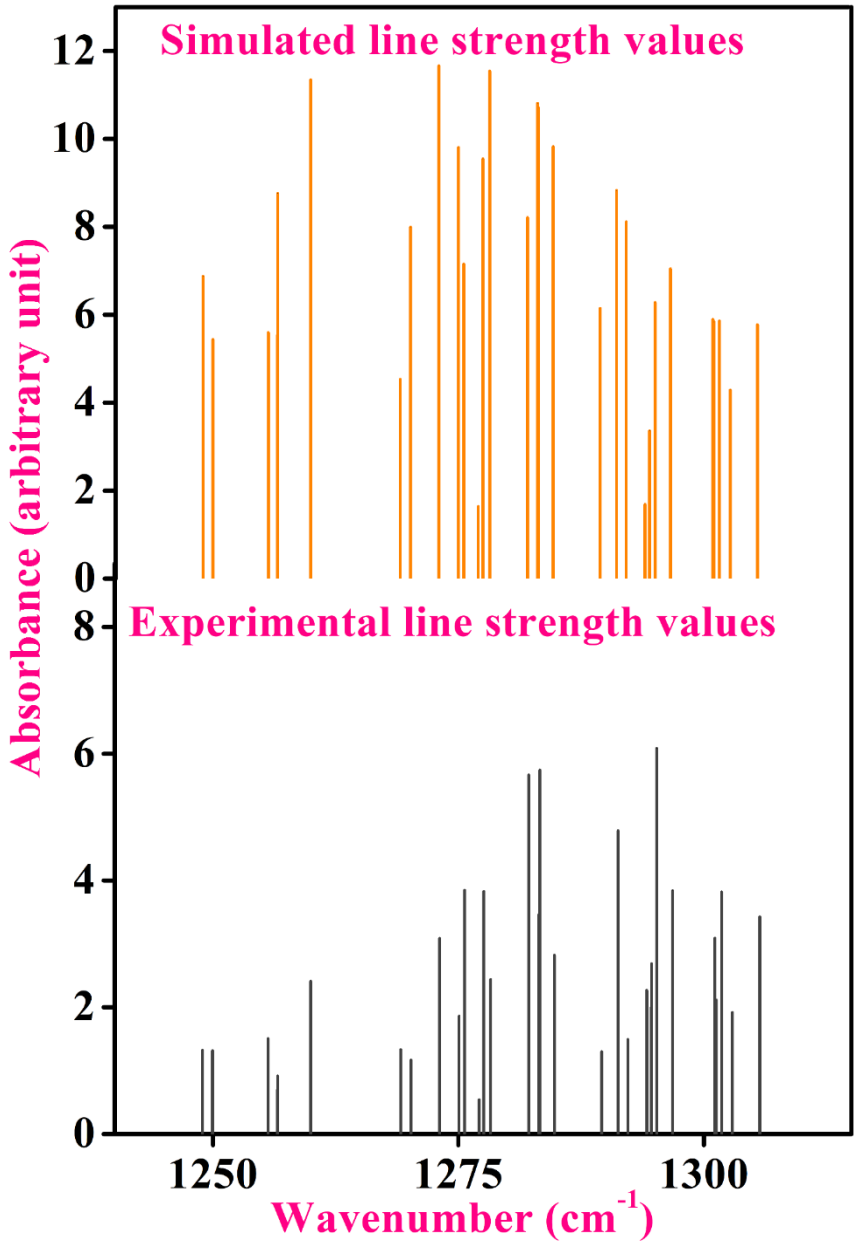

Fig. 4.4: A comparison of the experimental CRDS and PGOPHER simulated values of the line strengths of the spectral transitions.

Table 4.3: Experimentally obtained, simulated and Deroche reported spectral line positions for the ν_9 band of $^{12}CH_2D_2$ isotopomer. J", K_a" and K_c" are the ground state rotational quantum numbers while J', K_a' and K_c' are the excited state rotational quantum numbers. The assignment column written in the form of $^{\Delta Ka}\Delta J_{\Delta Kc}$.

Spectral transitions J′ K_a′ K_c′-J″	Assignment $^{\Delta Ka}\Delta J_{\Delta Kc}$	Simulated line position (cm^{-1})	Experimental line position	Line positions by Deroche (cm^{-}
2 0 2-1 0 1	$^{Q}R_R$	1248.9573	1248.934(5)	1248.969
2 1 1-1 1 0	$^{Q}R_R$	1249.9343	1249.947(2)	1249.949
3 2 2-2 2 1	$^{Q}R_R$	1255.6294	1255.613(4)	1255.645
3 1 2-2 1 1	$^{Q}R_R$	1256.6028	1256.568(4)	1256.609
3 2 1-2 2 0	$^{Q}R_R$	1256.5886	1256.582(5)	1256.609
4 0 4-3 0 3	$^{Q}R_R$	1259.9817	1259.963(1)	1259.997
5 2 4-4 2 3	$^{Q}R_R$	1267.5835	1267.584(3)	1267.596
5 4 1-4 4 0	$^{Q}R_R$	1269.1272	1269.122(4)	1269.135
5 3 2-4 3 1	$^{Q}R_R$	1270.1806	1270.170(3)	1270.188
6 2 5-5 2 4	$^{Q}R_R$	1273.0874	1273.082(3)	1273.099
6 3 4-5 3 3	$^{Q}R_R$	1275.0864	1275.072(3)	1275.099
6 4 3-5 4 2	$^{Q}R_R$	1275.6217	1275.624(6)	1275.633
5 3 2-4 1 3	$^{P}R_S$	1277.1141	1277.110(1)	1277.126
6 3 3-5 3 2	$^{Q}R_R$	1277.6073	1277.587(4)	1277.619
7 2 6-6 2 5	$^{Q}R_R$	1278.2737	1278.274(7)	1278.283
7 4 4-6 4 3	$^{Q}R_R$	1282.1577	1282.162(1)	1282.179
8 2 7 -7 2 6	$^{Q}R_R$	1283.1930	1283.172(2)	1283.207
8 1 7-7 1 6	$^{Q}R_R$	1283.3055	1283.292(6)	1283.319
9 0 9-8 0 8	$^{Q}R_R$	1283.7368	1283.744(3)	1283.758
7 3 4 -6 3 3	$^{Q}R_R$	1284.7532	1284.765(5)	1284.768
8 5 3-7 5 2	$^{Q}R_R$	1289.5953	1289.595(7)	1289.607
8 3 5-7 3 4	$^{Q}R_R$	1291.2565	1291.264(2)	1291.270
9 2 7-8 2 6	$^{Q}R_R$	1292.2419	1292.248(2)	1292.263
9 8 2-8 8 1	$^{Q}R_R$	1294.1704	1294.173(4)	1294.186
9 7 2-8 7 1	$^{Q}R_R$	1294.6670	1294.645(1)	1294.668
9 7 3-8 7 2	$^{Q}R_R$	1294.6492	1294.668(1)	1294.668
9 6 4-8 6 3	$^{Q}R_R$	1295.2222	1295.196(8)	1295.235
10 2 8-9 2 7	$^{Q}R_R$	1296.8050	1296.794(2)	1296.813
11 3 9-10 3	$^{Q}R_R$	1301.1364	1301.118(5)	1301.151
11 2 9-10 2	$^{Q}R_R$	1301.2525	1301.243(2)	1301.267
10 3 7-9 3 6	$^{Q}R_R$	1301.7897	1301.796(6)	1301.808
10 6 4-9 6 3	$^{Q}R_R$	1302.9000	1302.895(3)	1302.914
11 4 8-10 4	$^{Q}R_R$	1305.1728	1305.171(8)	1305.182

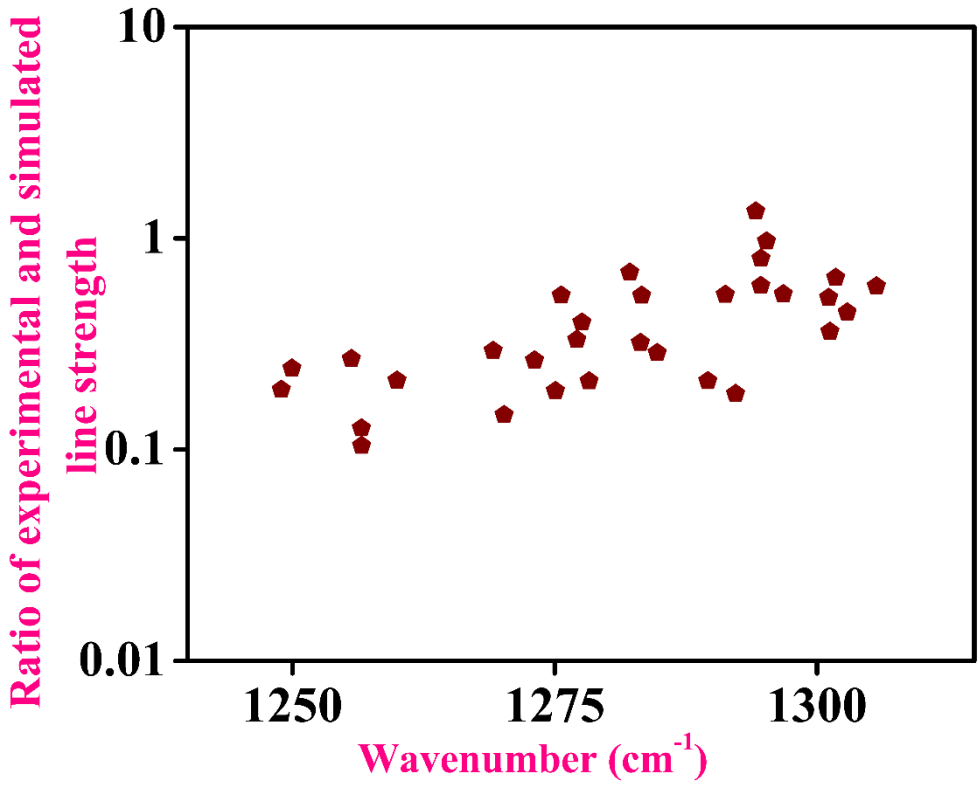

Fig. 4.5. A visual representation of ratio of simulated and experimental line strength values against wavenumber.

4.3.3 Line intensity measurements of $^{12}CH_2D_2$

Next, we discussed the line intensity measurements of each experimentally probed spectral line of $^{12}CH_2D_2$ isotopomer. This measurement was performed by injecting $^{12}CH_2D_2$ and zero air mixture of different pressure into the optical cavity. Fig. 4.6a shows high-resolution CRDS spectra at 1291.2642 cm^{-1} with different pressure of $^{12}CH_2D_2$. Here, the ring-down decay rate (in s^{-1}) was plotted against the wavenumber (in cm^{-1}), and subsequently, the absorption line was fitted with the Voigt line-shape function. The slope of the linear fit between the integrated peak-areas (in cm^{-1} s^{-1}) and corresponding pressures inside the optical cavity (in Torr), as shown in Fig. 4.6b was used to calculate the line intensity of the spectral transition. All the experimental values of the line intensity for each spectral transition of $^{12}CH_2D_2$ has been tabulated

in Table 4.4. It is noteworthy to mention that these are the first direct experimental evidence of the precise measurements of the line-strenghts of each ro-vibrational transition in the $\nu_9(B_2)$ fundamental band of $^{12}CH_2D_2$ using a CRDS technique coupled with a QC laser at 7.8 μm.

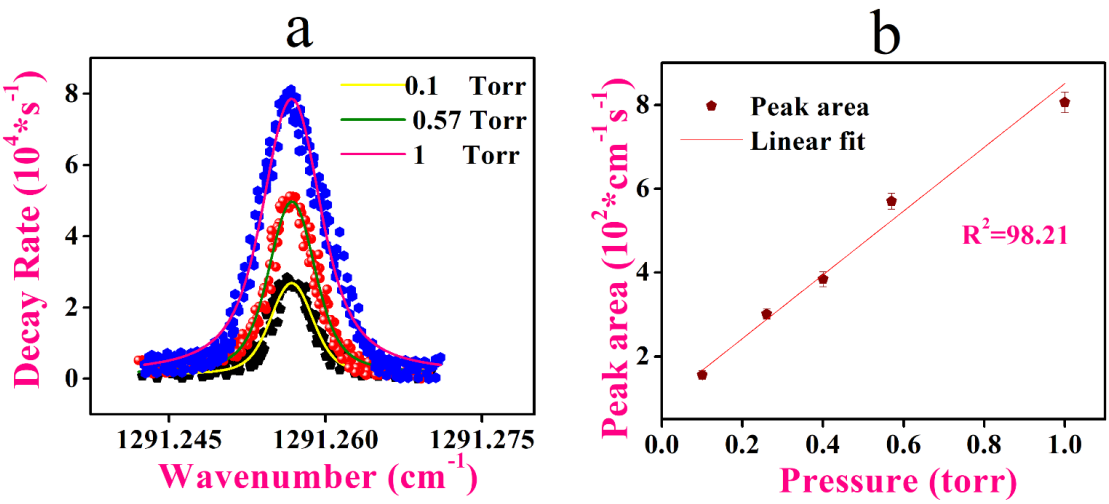

Fig. 4.6. (a) CRDS spectra at 1291.2642 cm^{-1} for different pressure of $^{12}CH_2D_2$ (b) A graph where pressure is plotted against the peak-area whose slope is used for the calculation of line-strength of the absorption line.

Table 4.4: Tabulation for the experimental line positions and line strengths of the experimentally probed absorption lines of $^{12}CH_2D_2$. In assignment column, J", K_a" and K_c" are referred to the ground state rotational quantum numbers while J', K_a' and K_c' are the excited state rotational quantum numbers.

Sl no	Wavenumber centre (cm^{-1}) (experimental)	Spectral transitions J′ K_a′ K_c′- J″ K_a″ K_c″	Line intensity (cm^{-1}molecule^{-1} cm^2*10^{-23}) (experimental)	Sl no	Wavenumber centre (cm^{-1}) (experimental)	Spectral transitions J′ K_a′ K_c′- J″ K_a″ K_c″	Line intensity (cm^{-1}molecule^{-1} cm^2*10^{-23}) (experimental)
1	1248.934(5)	2 0 2-1 0 1	1.32±0.03	**17**	1283.292(6)	8 1 7-7 1 6	5.74±0.07
2	1249.947(2)	2 1 1-1 1 0	1.31±0.03	**18**	1284.765(5)	7 3 4 -6 3 3	2.82±0.06
3	1255.613(4)	3 2 2-2 2 1	1.50±0.02	**19**	1289.595(7)	8 5 3-7 5 2	1.30±0.05
4	1256.568(4)	3 1 2-2 1 1	0.69±0.06	**20**	1291.264(2)	8 3 5-7 3 4	4.78±0.03
5	1256.582(5)	3 2 1-2 2 0	0.91±0.04	**21**	1292.248(2)	9 2 7-8 2 6	1.49±0.06
6	1259.963(1)	4 0 4-3 0 3	2.41±0.07	**22**	1294.173(4)	9 8 2-8 8 1	2.27±0.04
7	1269.122(4)	5 4 1-4 4 0	1.33±0.02	**23**	1294.645(1)	9 7 2-8 7 1	2.00±0.03
8	1270.170(3)	5 3 2-4 3 1	1.16±0.05	**24**	1294.668(1)	9 7 3-8 7 2	2.68±0.02
9	1273.082(2)	6 2 5-5 2 4	3.08±0.07	**25**	1295.196(8)	9 6 4-8 6 3	6.08±0.06
10	1275.072(3)	6 3 4-5 3 3	1.85±0.02	**26**	1296.794(2)	10 2 8-9 2 7	3.84±0.08
11	1275.624(6)	6 4 3-5 4 2	3.84±0.06	**27**	1301.118(5)	11 3 9-10 3 8	3.09±0.05
12	1277.110(1)	5 3 2-4 1 3	0.54±0.03	**28**	1301.146(2)	*	0.34±0.03
13	1277.587(4)	6 3 3-5 3 2	3.82±0.08	**29**	1301.243(2)	11 2 9-10 2 8	2.11±0.01
14	1278.274(7)	7 2 6-6 2 5	2.43±0.07	**30**	1301.796(6)	10 3 7-9 3 6	3.82±0.06
15	1282.162(1)	7 4 4-6 4 3	5.66±0.07	**31**	1302.895(3)	10 6 4-9 6 3	1.91±0.02
16	1283.172(2)	8 2 7 -7 2 6	3.46±0.05	**32**	1305.171(8)	11 4 8-10 4 7	3.42±0.03

4.3.4 Pressure broadening investigations of $^{12}CH_2D_2$

We next investigated the collisional or pressure broadening effect on the ro-vibrational lines of $^{12}CH_2D_2$ with various foreign gases at room temperature (298K) so that the spectral measurements were not only constrained to the Doppler broadened limited conditions at low pressures but also to the higher pressures. We subsequently determined each foreign gas's pressure broadening coefficients (i in cm-1 atm-1 (i = He, Ar, N2, Hydrogen mixture and zero air). Studying the pressure broadening effect and its coefficients provides important information for analyzing atmospheric spectra and has many important implications in planetary science. The above perturbing gas molecules were selected to investigate the different spectroscopic changes of the ro-vibrational lines in doubly-deuterated isotopomer of methane in various atmospheric conditions. In this investigation, we injected a specific concentration of the $^{12}CH_2D_2$ gas mixture into the cavity and subsequently increased the pressure inside the cavity by adding various gases. As shown in Fig.4. 7, we observed that with an increase in pressure of the perturbing gas, the spectral lines were getting broadened, and consequently, the peak-heights were reduced, which were ultimately balanced with the total area of the fitted absorption spectra. It is noted that each spectral line was fitted with the Voigt line-shape profile. A graph was then plotted between the total pressure inside the optical cavity and the Lorentzian FWHM (full width at half maximum) of each spectral line and from the slope of the linear fit the pressure broadening coefficient (γ) was calculated of that spectral line for each perturbing gas. The detailed tabulation for the γ values of each absorption line with respect to all gases has been provided in Table 4.5. These values are the first direct experimental determination (to our knowledge) of the pressure broadening coefficients of various spectral transitions of $^{12}CH_2D_2$ isotopomer in the ν_9 (B_2-symmetry) fundamental band using a high-resolution EC-QC laser combined with an ultra-sensitive CRDS technique.

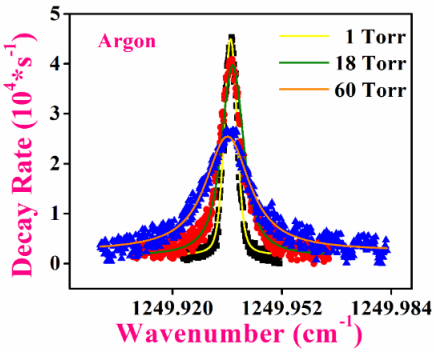
Argon
1 Torr
18 Torr
60 Torr
Decay Rate (10^4*s^-1)
Wavenumber (cm^-1)
1249.920
1249.952
1249.984

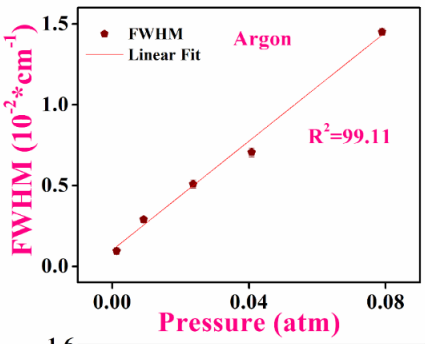
FWHM
Linear Fit
Argon
R^2=99.11
FWHM (10^-2*cm^-1)
Pressure (atm)
0.00
0.04
0.08

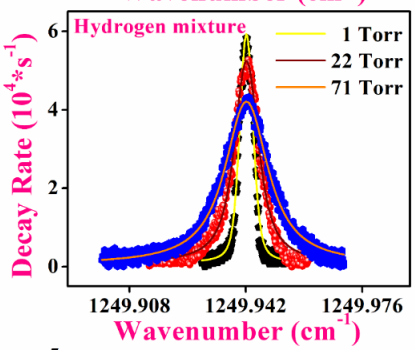
Hydrogen mixture
1 Torr
22 Torr
71 Torr
Decay Rate (10^4*s^-1)
Wavenumber (cm^-1)
1249.908
1249.942
1249.976

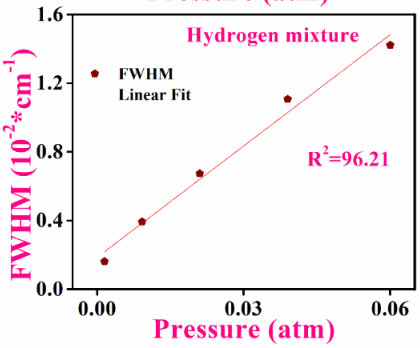
Hydrogen mixture
FWHM
Linear Fit
R^2=96.21
FWHM (10^-2*cm^-1)
Pressure (atm)
0.00
0.03
0.06

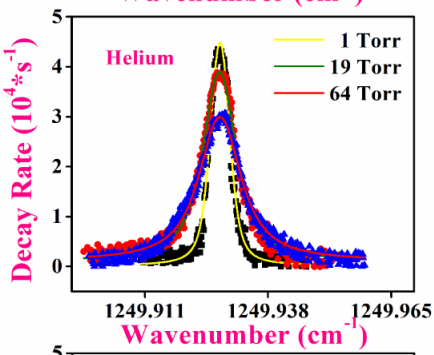
Helium
1 Torr
19 Torr
64 Torr
Decay Rate (10^4*s^-1)
Wavenumber (cm^-1)
1249.911
1249.938
1249.965

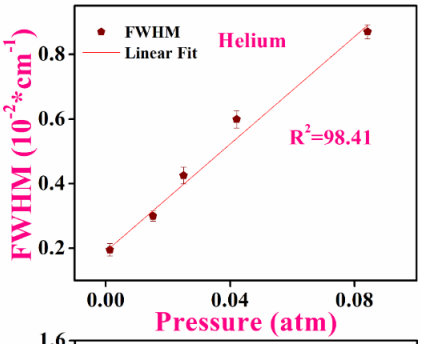
FWHM
Linear Fit
Helium
R^2=98.41
FWHM (10^-2*cm^-1)
Pressure (atm)
0.00
0.04
0.08

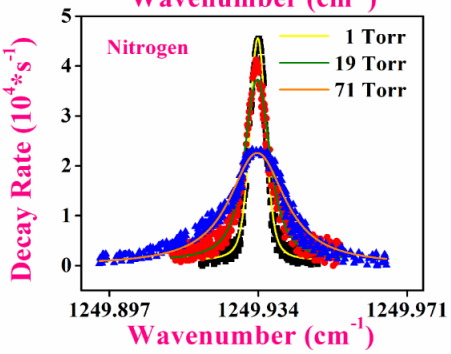
Nitrogen
1 Torr
19 Torr
71 Torr
Decay Rate (10^4*s^-1)
Wavenumber (cm^-1)
1249.897
1249.934
1249.971

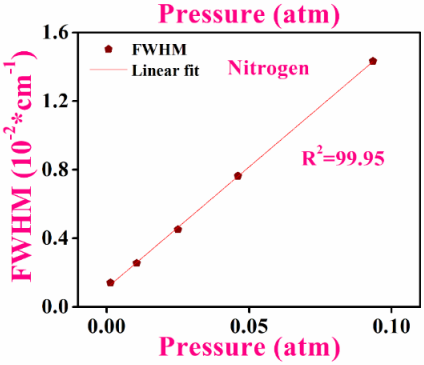
FWHM
Linear fit
Nitrogen
R^2=99.95
FWHM (10^-2*cm^-1)
Pressure (atm)
0.00
0.05
0.10

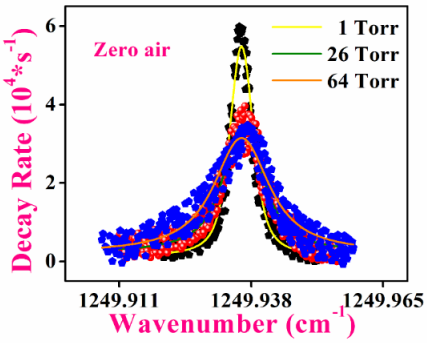
Zero air
1 Torr
26 Torr
64 Torr
Decay Rate (10^4*s^-1)
Wavenumber (cm^-1)
1249.911
1249.938
1249.965

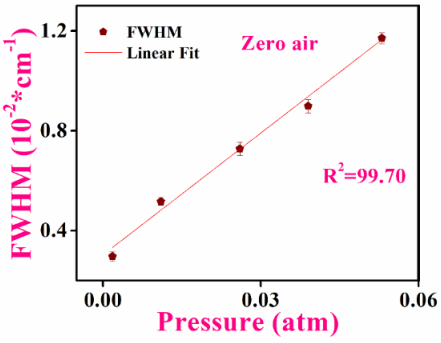
FWHM
Linear Fit
Zero air
R^2=99.70
FWHM (10^-2*cm^-1)
Pressure (atm)
0.00
0.03
0.06

Fig.4.7. Pressure broadening investigation of the spectral line of $^{12}CH_2D_2$ at 1249.94 cm^{-1} for different foreign gases. Linear plots between the Lorentzian FWHM of the spectral line and cavity pressures for different gases and the slopes were utilized for the calculation of broadening coefficients.

Table 4.5: Tabulation for the values of pressure broadening coefficients of various spectral lines with different gases.

Sl no	Wavenumber centre (cm^{-1}) (experimental)	Spectral transitions $J'\ K_a'\ K_c'$- $J''\ K_a''\ K_c''$	Pressure broadening coefficient ($cm^{-1}\ atm^{-1}$)				
			Zero air	Hydrogen mixture(H_2)	Nitrogen (N_2)	Helium (He)	Argon (Ar)
1	1248.934(5)	2 0 2-1 0 1	0.150±0.002	0.214±0.003	0.199±0.004	0.119±0.007	0.147±0.003
2	1249.947(6)	2 1 1-1 1 0	0.162±0.005	0.214±0.004	0.152±0.003	0.131±0.003	0.146±0.004
3	1255.613(4)	1 2 2-2 2 1	0.184±0.003	0.228±0.002	*	*	*
4	1259.963(5)	4 0 4-3 0 3	0.167±0.006	0.227±0.003	0.192±0.003	0.119±0.003	0.121±0.003
5	1267.584(3)	5 2 4-4 2 3	0.193±0.002	0.236±0.006	0.161±0.006	0.114±0.006	0.122±0.004
6	1270.170(9)	5 3 2-4 3 1	0.164±0.001	0.215±0.002	0.185±0.002	0.120±0.002	0.125±0.003
7	1273.082(3)	6 2 5-5 2 4	0.176±0.007	0.230±0.001	0.169±0.001	0.100±0.001	0.120±0.003
8	1275.072(9)	6 3 4-5 3 2	0.193±0.003	0.234±0.003	0.190±0.002	0.088±0.007	0.108±0.007
9	1275.624(6)	6 4 3-5 4 2	0.163±0.004	0.224±0.003	0.157±0.007	0.103±0.003	0.132±0.003
10	1277.110(2)	5 3 2-4 1 3	0.200±0.002	0.252±0.004	0.181±0.004	0.095±0.004	0.128±0.004
11	1277.587(8)	6 3 3-5 3 2	0.144±0.003	0.233±0.002	0.189±0.003	0.147±0.002	0.140±0.002
12	1278.274(5)	7 2 6-6 2 5	0.147±0.002	0.211±0.005	0.198±0.003	0.064±0.003	0.117±0.003
13	1282.162(3)	7 4 4-6 4 3	0.146±0.002	0.185±0.003	0.200±0.002	0.124±0.002	0.126±0.002
14	1283.172(1)	8 2 7 -7 2 6	0.172±0.007	0.202±0.002	0.192±0.004	0.086±0.002	0.116±0.002
15	1283.744(3)	9 0 9-8 0 8	0.196±0.003	0.220±0.007	0.180±0.007	0.182±0.007	0.128±0.007

16	1284.765(4)	7 3 4 -6 3 3	0.206±0.004	0.218±0.001	0.203±0.001	0.120±0.001	0.138±0.001
17	1289.595(6)	8 5 3-7 5 2	0.141±0.005	0.220±0.007	0.197±0.004	0.107±0.004	0.121±0.004
18	1291.264(5)	8 3 5-7 1 4	0.127±0.003	0.191±0.005	0.155±0.005	0.096±0.005	0.109±0.005
19	1292.248(7)	9 2 7-8 2 6	0.174±0.004	0.209±0.003	0.137±0.003	0.074±0.003	0.105±0.003
20	1294.173(4)	9 8 2-8 8 1	0.167±0.003	0.219±0.004	0.175±0.004	0.138±0.004	0.119±0.004
21	1295.194(5)	9 6 4-8 6 3	0.131±0.003	0.203±0.008	0.175±0.003	0.109±0.003	0.116±0.003
22	1296.794(3)	10 2 8-9 2 7	0.162±0.004	0.194±0.004	0.177±0.003	0.083±0.003	0.110±0.003
23	1301.243(3)	11 2 9-10 2 8	0.137±0.001	0.193±0.001	0.129±0.004	0.083±0.004	0.108±0.004
24	1301.796(7)	10 3 7-9 3 6	0.147±0.003	0.216±0.006	0.139±0.001	0.095±0.001	0.107±0.001
25	1302.895(4)	10 6 4-9 6 3	0.130±0.005	0.201±0.005	0.180±0.006	0.075±0.006	0.112±0.006
26	1305.171(8)	11 4 8-10 4 7	0.116±0.007	0.223±0.007	0.140±0.005	0.093±0.005	0.104±0.005

We then explored whether the pressure broadening co-efficients (γ_i) of the perturbing gases associated with the relevant transitions depend on the rotational quantum number (J). In order to do this, we plotted the variation of γ values against J for each perturbing gas as shown in Fig.4.8. We observed that with the increase in J, the γ values, in general, decreased irrespective of the type of transition or the perturbing gases.

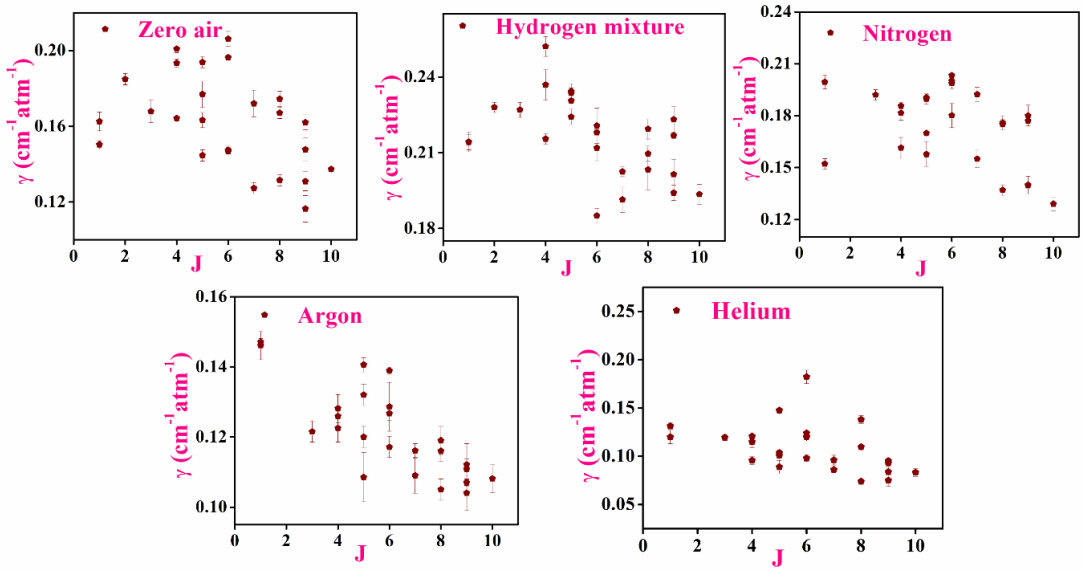

Fig. 4.8. Variation of the calculated broadening coefficients (γ_i) for different perturbed gases as a function of rotational quantum number J.

4.3.5 Squared transition moment measurements of $^{12}CH_2D_2$

Finally, we calculated the squared transition moment by using the line-strength of each ro-vibrational transition of $^{12}CH_2D_2$ molecule. The intensity of the individual absorption line is connected with the transition moment s according to the following formula as given in the HITRAN database [33].

$$S_{ij}=\frac{8\pi^3 10^{-36}}{3hcQ_{tot}(T)} g_c \nu_{ij} e^{\frac{-hcE_i}{k_B T}} (1 - e^{\frac{-hc\nu_{ij}}{k_B T}}) R_{ij} \quad 4.1$$

where, S_{ij} represents the line-strength of each individual spectral line; ν_{ij} is the line-centre of transition lines in cm^{-1}; E_i is the total ro-vibrational energy of the lower state in cm^{-1}; c, h, k_B is the velocity of light, Planck constant and Boltzmann constant, respectively; $Q_{tot}(T)$ is the total partition function at 296K; g_c is the nuclear spin statistical weight whose value g_c=21 for ν_9 band [27] and R_{ij} refers to the squared of transition moment of spectral lines. In this context, we have utilized the experimentally CRDS-determined values of line-centre and line-strength of the corresponding spectral transitions as given in Table 4.4. We have also used the values of the total partition function of $^{12}CH_2D_2$ at 296K and the total ro-vibrational energy of the lower state from the work of M. Rey and O. N. Ulenikov group [27,22], respectively, for this calculation. The calculated values of the squared transition moment of all the probed spectral lines in this study have been given in Table 4.6. We have also shown the dependence of the transition moment with rotational quantum number *J* in Figure 4.9. and observed that the squared value of the transition moment increases with *J*. Taken together, these new results in the *a*-type ν_9 (B_2-symmetry) fundamental band are an important step forward towards a better understanding of the ro-vibrational spectra and level dynamics of the $^{12}CH_2D_2$ isotopomer of methane.

Table 4.6: Tabulation for the calculated values of the transition moments for various ro-vibrational transition lines of $^{12}CH_2D_2$ isotopomer.

Sl no	Wavenumber centre (cm^{-1}) (experimental)	Spectral transitions J′ K_a' K_c'- J″ K_a'' K_c''	Transition moment $(Debye)^2$	Sl no	Wavenumber centre (cm^{-1}) (experimental)	Spectral transitions J′ K_a' K_c'- J″ K_a'' K_c''	Transition moment $(Debye)^2$
1	1248.934(5)	2 0 2-1 0 1	0.000072(3	**17**	1283.292(6)	8 1 7-7 1 6	0.000634(2)
2	1249.947(2)	2 1 1-1 1 0	0.000073(2	**18**	1284.765(5)	7 3 4 -6 3 3	0.000304(8)
3	1255.613(4)	3 2 2-2 2 1	0.000089(5	**19**	1289.595(7)	8 5 3-7 5 2	0.000195(7)
4	1256.568(4)	3 1 2-2 1 1	0.000041(1	**20**	1291.264(2)	8 3 5-7 3 4	0.000646(4)
5	1256.582(5)	3 2 1-2 2 0	0.000054(3	**21**	1292.248(2)	9 2 7-8 2 6	0.000251(3)
6	1259.963(1)	4 0 4-3 0 3	0.000153(1	**22**	1294.173(4)	9 8 2-8 8 1	0.001010(5)
7	1269.122(4)	5 4 1-4 4 0	0.000104(5	**23**	1294.645(1)	9 7 2-8 7 1	0.000412(2)
8	1270.170(3)	5 3 2-4 3 1	0.000088(5	**24**	1294.668(1)	9 7 3-8 7 2	0.000554(7)
9	1273.082(2)	6 2 5-5 2 4	0.000264(3	**25**	1295.196(8)	9 6 4-8 6 3	0.001120(6)
10	1275.072(3)	6 3 4-5 3 3	0.000165(6	**26**	1296.794(2)	10 2 8-9 2 7	0.001550(7)
11	1275.624(6)	6 4 3-5 4 2	0.000351(4	**27**	1301.118(5)	11 3 9-10 3 8	0.001660(4)
12	1277.110(1)	5 3 2-4 1 3	0.000039(2	**28**	1301.146(2)	*	*
13	1277.587(4)	6 3 3-5 3 2	0.000339(4	**29**	1301.243(2)	11 2 9-10 2 8	0.000637(3)
14	1278.274(7)	7 2 6-6 2 5	0.000249(4	**30**	1301.796(6)	10 3 7-9 3 6	0.001360(5)
15	1282.162(1)	7 4 4-6 4 3	0.000624(2	**31**	1302.895(3)	10 6 4-9 6 3	0.000495(2)
16	1283.172(2)	8 2 7 -7 2 6	0.000437(7	**32**	1305.171(8)	11 4 8-10 4 7	0.000823(6)

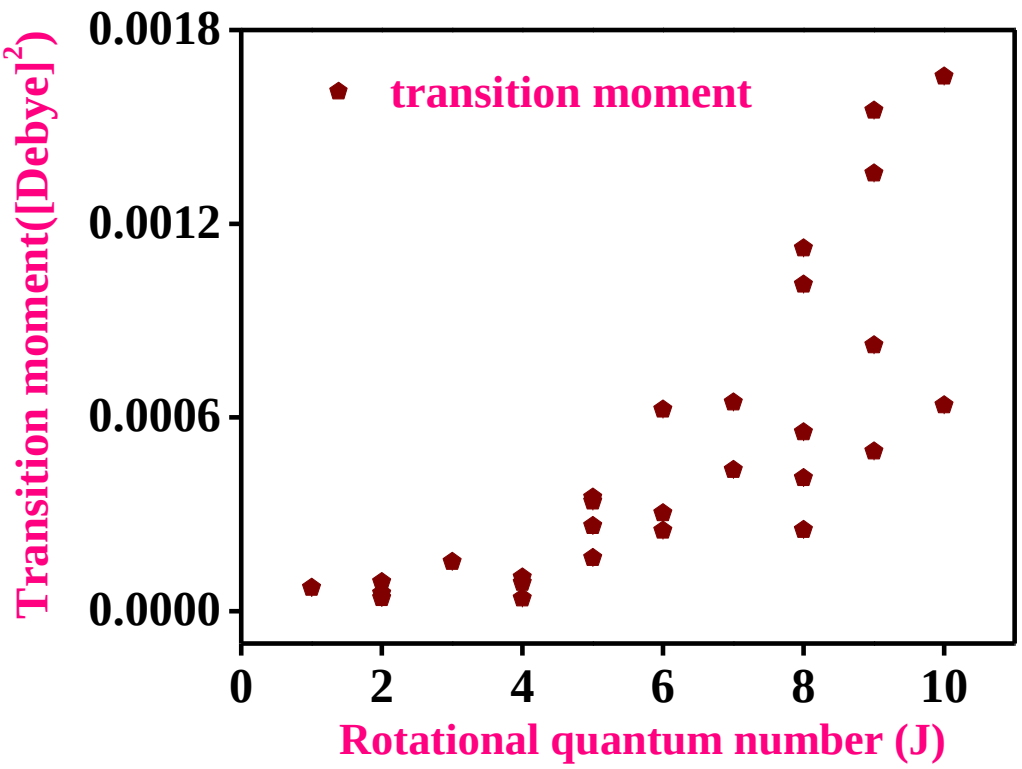

Fig. 4.9. Variation of squared transition moment with rotational transition moment *J*

4.4 Conclusion

In this chapter we have provided the first detailed high-resolution analysis of the ro-vibrational spectral features of the *a*-type ν_9 (B_2-symmetry) fundamental band of $^{12}CH_2D_2$ isotopomer of methane. The latest EC-QCL technology coupled with the optical cavity-enhanced absorption technique such as *cw*-CRDS methodology has provided to resolve the fine structure of the ro-vibrational lines of $^{12}CH_2D_2$ with a resolution of 0.001 cm^{-1}. High-level calculations and simulations such as Gaussian 16 and PGOPHER were performed for accurate spectral assignments of the ro-vibrational transition lines of $^{12}CH_2D_2$ molecule. We measured the line-strengths and subsequently determined the squared transition dipole moments of the probed absorption lines of $^{12}CH_2D_2$. Further, we studied the pressure broadening effect on the spectral lines of $^{12}CH_2D_2$ with several foreign gases like He, N_2, Hydrogen mixture, Ar, etc and determined the broadening coefficients of each ro-vibrational transition with respect to each perturbing gas. Thus, a good knowledge of the gas-phase ro-

vibrational spectral features of $^{12}CH_2D_2$ will give a new window for the investigation of detailed structure and vibrational dynamics of methane isotopomers.

4.5 References:

1) D. W. Griffith, P. Denis, S. Stefan, H. Samuel, N.V. Sanam and P. Platt. "Long open-path measurements of greenhouse gases in air using near-infrared Fourier transform spectroscopy." *Atmos. Meas. Tech.,* 2018, **11**, 1549-1563.

2) J. Xia, F. Zhu, S. Zhang, A. Kolomenskii, J. Dong, K. Okada, J. Strohaber, and H. A.Schuessler. "Probing greenhouse gases in turbulent atmosphere by long-range open-path wavelength modulation spectroscopy." *Opt. Lasers. Eng.,* 2019, **117**, 21-28.

3) M. J. Elrod, "Greenhouse warming potentials from the infrared spectroscopy of atmospheric gases." *J. Chem. Educ.,* 1999, **76**, no. 12, 1702.

4) Q. Gao, Y. Zhang, J. Yu, S. Wu, Z. Zhang, F. Zheng, X. Lou, and W. Guo. "Tunable multi-mode diode laser absorption spectroscopy for methane detection." *Sens. Actuators, A,* 2013, **199**, 106-110.

5) T. Skytt, S. N. Nielsen, and B.G. Jonsson. "Global warming potential and absolute global temperature change potential from carbon dioxide and methane fluxes as indicators of regional sustainability–A case study of Jamtland, Sweden." *Ecol. Indic.,* 2020, **110**, 105831.

6) O. Boucher, P. Friedlingstein, B. Collins, and K. P. Shine. "The indirect global warming potential and global temperature change potential due to methane oxidation." *Environ. Res., Lett,* 2009, **4**, no. 4 ,2009: 044007.

7) E. D. Young, I. E. Kohl, B. S. Lollar, G. Etiope, D. R. Iii, S. Li, M. A. Haghnegahdar, E. A. Schauble, K. A. McCain, D. I. Foustoukos, and C. Sutclife, "The relative abundances of resolved $^{12}CH_2D_2$ and $^{13}CH_3D$ and mechanisms controlling isotopic bond ordering in abiotic and biotic methane gases." *Geochim. Cosmochim. Acta.,* 2017, **203**, 235-264

8) J. Edling, A. Hugh, H. Richardson, and G. E. Ewing. "Infrared spectroscopy of CH_4, CH_2D_2 and CD_4 adsorbed on sodium chloride films." *J. Mol. Struct.,* 1987, **157**, no. 1-3, 167-185.

9) J. K. Wilmshurst and H. J. Bernstein. "THE INFRARED SPECTRA OF CH4, CH_3D, CH_2D_2, CD_3H, and CD_4." *Can. J. Chem.,* 1957, **35**, no. 3 226-235.

10) Y. P. Delgado, E. K. Lewis, C. J. Moehnke, M. C. Salazar, A. J. Hernandez, and C. E. Manzanares. "Cavity ring down absorption at low temperatures: C–H spectra ($\Delta\upsilon$= 1–6) of CH_3D and C–H overtones ($\Delta\upsilon$= 5, 6) of CH_2D_2 and CH_4." *Mol. Phys.,* 2009, **107**, no. 13, 1367-1377.

11) P. Bergmaschi, and G. W. Harris. "Measurements of stable isotope ratios ($^{13}CH_4/^{12}CH_4$; $^{12}CH_3D/^{12}CH_4$) in landfill methane using a tunable diode laser absorption spectrometer." *Global Biogeochem. Cycles,* 1995, **9**, 439-447.

12) P. Varanasi. "High-Resolution Laboratory Data on the Infrared Spectral Lines of Methane and Other Hydrocarbons Needed in Studies of the Jovian Atmosphere." *Bulletin of the American Astronomical Society*, 1993, **25**, 1036.

13) P. Varanasi and S. Chudamani. "Linewidth measurements in the thermal infrared bands of $^{12}CH_3D$ at planetary atmospheric temperatures." *Appl. opt.* 1989, **28**, 2119-2122.

14) M. T. Lemmon, P. H. Smith, and R. D. Lorenz. "Methane abundance on Titan, measured by the space telescope imaging spectrograph." *Icarus,* 2002, **160**, 375-385.

15) O. Mousis, E. Chassefiere, N. G. Holm, A. Bouquet, J. H. Waite, W. D. Geppert, S. Picaud, Y. Aikawa, M. Ali-Dib, J. L. Charlou, and P. Rousselot. "Methane clathrates in the solar system." *Astrobiology,* 2015, **15**, 308-326.

16) L. S. Rothman, D. Jacquemart, A. Barbe, D. Chris Benner, M. Birk, L. R. Brown, M. R. Carleer, C. Chackerian, K. Chance, L. H. Coudert, V. Dana, V. M. Devi, J. M. Flaud, R. R. Gamache, A. Goldman, J. M. Hartmann, K. W. Jucks, A. G. Maki, J. Y. Mandin, S. T. Massie, J. Orphal, A. Perrin, C. P. Rinsland, M. A. H. Smith, J. Tennyson, R. N. Tolchenov, R. A. Toth, J. Vander Auwera, P. Varanasi, G. Wagner, "The HITRAN 2004 molecularspectroscopic database." J. Quant. Spectrosc. Radiat. Transfer, 2005, **96**, 139-204.

17) L. S. Rothman, I. E. Gordon, Y. Babikov, A. Barbe, D. Chris Benner, P. F. Bernath, M. Birk, L. Bizzocchi, V. Boudon, L. R. Brown, A. Campargue, K. Chance, E. A. Cohen, L. H. Coudert, V. M. Devi, B. J. Drouin, A. Fayt, J. M. Flaud, R. R. Gamache, J. J. Harrison, J. M. Hartmann, C. Hill, J. T. Hodges, D. Jacquemart, A. Jolly, J. Lamouroux, R. J. Le Roy, G. Li, D. A. Long, O. M. Lyulin, C. J. Mackie, S. T. Massie, S. Mikhailenko, H. S. P. Müller, O. V. Naumenko, A. V. Nikitin, J. Orphal, V. Perevalov, A. Perrin, E. R. Polovtseva, C. Richard, M. A. H. Smith, E. Starikova, K. Sung, S. Tashkun, J. Tennyson, G. C. Toon, V. G. Tyuterev and G. Wagne, "The HITRAN 2012 molecular spectroscopic database." J. Quant. Spectrosc. Radiat. Transfer,2013, **130**, 4-50.

18) O. N. Ulenikov, A. B. Malikova, G. A. Shevchenko, G. Guelachvili, and M. Morillon-Chapey. "High-resolution Fourier transform spectra of CH_2D_2: The Fermi-interacting vibrational bands ν_8 (B_2), $\nu_4+\nu_9$ (B_2) and $2\nu_9$ (A_1), $\nu_3+\nu_4$ (A_1)." *J. Mol. Spectrosc.,* 1991, **149**, 160-166.

19) O. N. Ulenikov, E. S. Bekhtereva, S. V. Grebneva, H. Hollenstein, and M. Quack. "High resolution Fourier transform spectroscopy of CH_2D_2 in the region 2350–2650 cm− 1: the bands ν_5+ ν_7, 2ν_9, ν_3+ ν_4, ν_3+ ν_7 and ν_5+ ν_9 *Phys. Chem. Chem. Phys.,* 2005, **7**, 1142-1150.

20) O. N. Ulenikov, E. S. Bekhtereva, S. V. Grebneva, H. Hollenstein, and M. Quack. "High-resolution rovibrational analysis of vibrational states of A2 symmetry of the dideuterated methane CH_2D_2: the levels ν_5 and ν_7+ ν_9." *Mol. Phys.,* 2006, **104**, 3371-3386.

21) O. N. Ulenikov, E. S. Bekhtereva, S. Albert, S. Bauerecker, H. Hollenstein, and M. Quack. "High-resolution near infrared spectroscopy and vibrational dynamics of dideuteromethane (CH_2D_2)." *J. Phys. Chem.,* 2009, *A* **113**, 2218-2231.

22) O. N. Ulenikov, R. N. Tolchenov, M. Koivusaari, S. Alanko, and R. Anttila. "High-resolution Fourier transform spectra of CH_2D_2: pentade of the lowest interacting vibrational bands ν_4 (A_1), ν_7 (B_1), ν_9 (B_2), ν_5 (A_2), and ν_3 (A_1)." *J. Mol. Spectrosc.,* 1994, **167**, 109-130.

23) J. C. Deroche and G. Guelachvili. "High resolution infrared spectrum of CH_2D_2: The v1 and v6 fundamental bands near 3000 cm− 1." *J. Mol. Spectrosc.* 1975, **56**, 76-87.

24) J. C. Deroche, G. Graner, and A. Cabana. "High-resolution infrared spectrum of CH_2D_2: The v3 fundamental band at 7 μm." *J. Mol. Spectrosc.* 1975, **57**, 331-347.

25) J. C. Deroche, G. Graner, J. Bendtsen, and S. Brodersen. "The v5 and v3 Raman bands of CH_2D_2." *J. Mol. Spectrosc.* 1976, **62**, 68-79.

26) J. C. Deroche and P. Pinson. "High-resolution infrared spectrum of CH_2D_2: The v9 fundamental band at 8 uṃ." *J. Mol. Spectrosc.* 1975, **58**, 229-238.

27) M. Rey, A. V. Nikitin, and V. G. Tyuterev. "First predictions of rotationally resolved infrared spectra of dideuteromethane ($^{12}CH_2D_2$) from potential energy and dipole moment surfaces." *J. Phys. Chem.* 2015 *A* **119**, 4763-4779.

28) R. Signorell, R. Marquardt, M. Quack, and M. A. SUHM. "The permanentectric dipole moment of CH_2D_2: FIR el spectroscopy." *Mol. Phys.* 1996, **89**, 297-313.

29) H. G. Yu, "Accurate quantum dynamics calculations of vibrational spectrum of dideuteromethane CH_2D_2." *J. Chem. Phys.* 2015, **142,** 194307.

30) A. Maity, M. Pal, G. D. Banik, S. Maithani, and M. Pradhan. "Cavity ring-down spectroscopy using an EC-QCL operating at 7.5 μm for direct monitoring of methane isotopes in air." *Laser Phys. Lett.,* 2017,**14**,115701.

31) M. Pal, S. Maithani, A. Maity, and M. Pradhan. "Simultaneous monitoring of 32 S, 33 S and 34 S isotopes of H 2 S using cavity ring-down spectroscopy with a mid-infrared external-cavity quantum cascade laser." *J. Anal. At. Spectrom.* 2019, **34**, 860-866.

32) S. Maithani, A. Maity, and M. Pradhan. "High-resolution spectral analysis of hybrid A/B-type band of 1, 3-butadiene at 6.2 μm using an EC-QCL coupled with cavity ring-down spectroscopy." *Chem. Phys.*, 2019, **522**,123-128.

33) Šimečková, Marie, David Jacquemart, Laurence S. Rothman, Robert R. Gamache, and Aaron Goldman. "Einstein A-coefficients and statistical weights for molecular absorption transitions in the HITRAN database." *Journal of Quantitative Spectroscopy and Radiative Transfer* 98, no. 1 (2006): 130-155.

Chapter-5

Direct and 2f-wavelength modulation spectroscopy of NO and OCS using an astigmatic multipass cell coupled with a mid-IR 5.2 μm cw-QCL

Contents

5.1 Introduction……95

5.2 Basic Principle of wavelength modulation spectroscopy....96

5.3 Experimental section……97

5.4 Results and discussions……..…..99

5.4.1 Selections of absorption lines……..…..99

5.4.2 Optimization of 2f-WMS signal……. 100

5.4.3 Calibration of 2f-WMS signal……103

5.4.4 Allan Variance test……...104

5.4.5 Comparison signal-to-noise ratio between DAS AND WMS techniques……..105

5.5 Conclusion……...108

5.6 References ……...108

5.1 Introduction

Direct absorption spectroscopy (DAS) is one of the most simple and versatile detection techniques widely used for trace gas detection [1-2]. However, the low-frequency noise limits the sensitivity of DAS. The wavelength modulation spectroscopy (WMS) technique is a good alternative for DAS, where the excessive laser noise could be reduced and the detection method can be used in harsh environmental conditions due to its high signal-to-noise ratio. In WMS, the laser frequency is modulated at a frequency in kilohertz (kHz) range, and the high-frequency wavelength modulation causes the laser to scan back and forth over the part of absorption features due to tuning of laser wavelength across the absorption lines. This absorption affects the spectral profile of the transmitted intensity and introduces harmonic components to the output signal. Then, the detector signal is demodulated at the higher harmonics of the primary signal. We can isolate the harmonics using a lock-in-amplifier after the demodulation. Some earlier studies utilized the WMS technique to detect several trace gases [3-8]. Nevertheless, simultaneous probing of nitric oxide (NO) and carbonyl sulfide (OCS) using an astigmatic multipass cell coupled with the 2*f*-WMS technique in the mid-IR spectral region has not yet been explored in detail.

Both NO and OCS have potential sources involving biomass burning and anthropogenic activities in chemical industries. The generation of OCS is also associated with biogenic ocean activity. On the other hand, NO is an important atmospheric pollutant that is usually released from daily-used vehicles. It also plays a vital role in atmospheric chemistry. NO plays an essential role in cell metabolism and is also related to various respiratory diseases like asthma and chronic obstructive pulmonary disease [9-16, 21-23].

Moreover, carbonyl sulfide (OCS) has various astrophysical applications and is the second most sulfur-containing species in the atmosphere of Venus [17]. Therefore, high-sensitivity and simultaneous real-time monitoring of both NO and OCS are important and require suitable detection methods. The recent technological developments of a mid-IR external-cavity quantum cascade laser (EC-QCL) provide a

suitable light source coupled with the WMS technique for trace gas sensing. The unique features of the EC-QCL, such as narrow line-width, broad tunability, and high output power at room temperature operation, make it very useful in the field of high-resolution spectroscopy [18].

In this chapter, we report on developing a mid-IR 2*f*-WMS method coupled with an astigmatic gas cell and a QCL operating between 5.04 µm to 5.45 µm. We applied the WMS technique to monitor two trace gas molecules, NO and OCS. We demonstrated the details of the 2*f*-WMS method by probing the strongest absorption lines of NO and OCS at 1900.0706 cm^{-1} and 1899.9756 cm^{-1}, respectively, which are positioned in the spectral regions interference-free from other major atmospheric gases. We investigated the optimum output detector signal using the different modulation parameters in the experiment to achieve the maximum signal-to-noise ratio. Finally, a comparison between the direct absorption and 2*f*-WMS for combined monitoring of NO and OCS was performed with a subsequent explanation of why the WMS technique was better in sensitivity compared to the DAS at the same experimental conditions.

5.2 Basic principle of Wavelength modulation spectroscopy (WMS)

Basically, in WMS technique, the laser source, having linewidth smaller than the line width of the absorption line to be observed, is modulated with a high-frequency sine wave [19]. As Modulated laser source scans the absorption line slowly, wavelength modulation turns to amplitude modulation, which is detected after demodulation at a higher frequency by lock-in-amplifier. Thus, WMS is recognized as a derivative spectroscopy.

Laser absorption spectroscopy is governed by the well-known Beer Lambert equation. When incident laser light scans across the sample absorption region, the transmitted light intensity follows the Beer's law:

$$I(\nu)=I_0(\nu)\exp[-\alpha(\nu)L] \quad 5.1$$

where $I_o(\nu)$ is the incident laser intensity, $I(\nu)$ is the transmitted laser intensity, ν is the emission frequency, α(ν) is the absorption coefficient, and L is the optical path length.

Modulation spectroscopic techniques are basically classified into two categories, one is frequency modulation (FM), and another is wavelength modulation (WM). In FM spectroscopy, laser light is modulated at frequencies larger than the target absorption line width, where as in WMS technique; modulation frequency should be kept lower than the absorption line width. In present study we have used the WMS technique.

In WMS technique, modulated laser frequency can be expressed as

$$I(\nu)=I_0(\nu)[1-\alpha(\nu)L] \qquad 5.2$$

$$\nu(t)= \nu_{ave} + aCos(\omega t) \qquad 5.3$$

Where ν_{ave} is the mean laser frequency, a is the modulation amplitude and ω is the angular frequency of the modulation.

The transmitted light intensity has a time dependent part, which can be expanded into cosine Fourier series corresponding to multiples of ω:

$$I(\nu) =I_0(\nu)[1- \alpha(\nu_{ave} + aCos(\omega t))L] \qquad 5.4$$

$$\alpha(\nu_{ave} + aCos(\omega t)) = \sum_{n=0} H_n(\nu_{ave})Cos(n\omega t) \qquad 5.5$$

Where $H_n(\nu_{ave})$ demonstrates the n^{th} Fourier co-efficient of the modulated absorption coefficient. Now incorporating lock-in-amplifier, nth harmonic of the modulation frequency can be detected. As detection bandwidth shifts to large frequency region, it gives the advantage to avoid the low frequency drifts in laser intensity and excess laser noise ($\sim 1/f$) which help to increase the signal to noise ratio immensely.

5.3 Experimental set-up

We have used a light-weight astigmatic multipass cell (AMAC-76LW, Aerodyne Research, USA) with a pathlength of 76 m coupled with a cw EC- QCL (TLS-41053-MHF, Daylight Solutions, USA) working at 5.2 μm. The cell is comprised of two

Nickel-plated aluminium with broad-band dielectric coating mirrors with a reflectivity of 99.2%, and the cell also has a window made up of BaF_2 for the entry of laser light into the multipass cell. A schematic diagram of the developed experimental set-up is shown in Figure 5.1. The laser light was directed into an acousto-optic modulator (AOM) (AGM-405B11M) which diffracts the light into sub-beams. One sub-beam was focused on to a wavemeter (771B-MIR, Bristol Instruments) for real-time monitoring of the wavenumber with an accuracy of $0.001cm^{-1,}$ and the second sub-beam was directed into the multipass cell. We have used a visible He-Ne laser source operating at 633 nm for the alignment of the mid-IR laser beam into the cell and obtained a maximum number of reflections with the help of the visible light source.

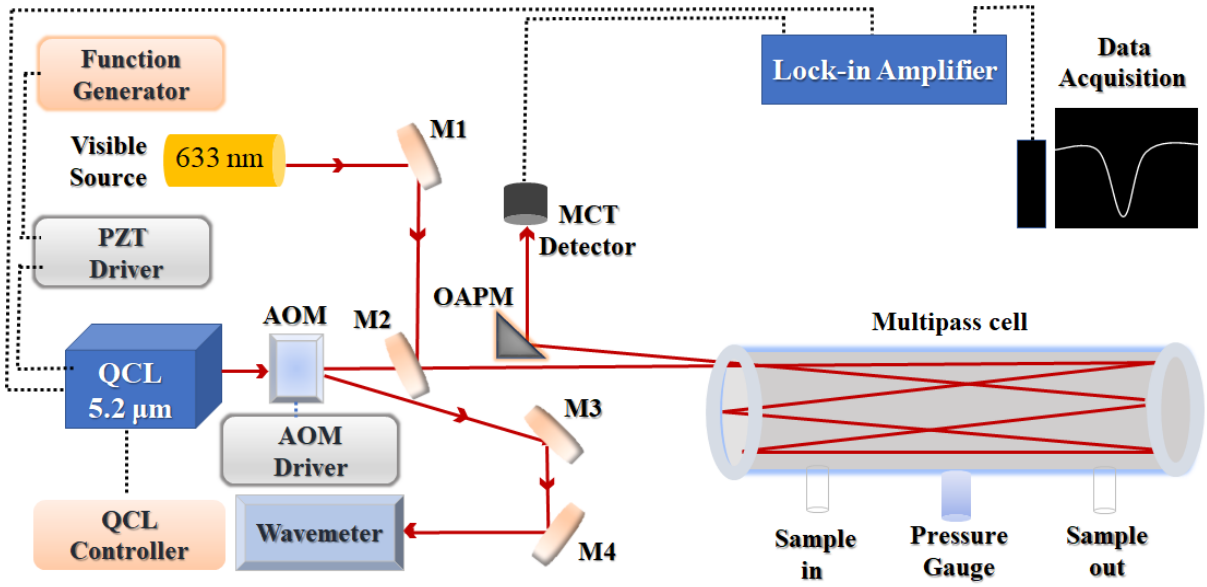

Figure-5.1: - A schematic diagram of the developed experimental setup for the wavelength modulation spectroscopy employing a multipass cell coupled with QCL. M1, M2, M3, M4 are the corresponding bending mirrors.

We then focused the laser beam exiting the cell to the MCT detector (PVI-4TE-8-1X1; Vigo System S.A.) with an off-axis parabolic mirror (OAPM). A pressure gauge (Pfeiffer vacuum) was also connected with the gas cell to maintain the optimum pressure.

For the wavelength modulation, a 30 kHz sine wave modulation injection current was applied to the EC-QCL, and we have used a lock-in-amplifier (Standford Research Systems SR830 DSP) for the detection of detector signal. Further, we have used a piezo-electric driver (MDT693B; Thorlabs) connected with a function generator from which a sine wave of 2.5 Hz with voltage amplitude 25 V was applied to the EC- QCL for the scanning of the selected absorption region of the molecular species.

Finally, the detector signal was transferred to the lock-in-amplifier to demodulate the detector signal at the harmonics of the modulating frequency. The time constant of the lock-in-amplifier was set to 1 ms to obtain optimum experimental conditions. Finally, the demodulated signal was transferred to the high-speed data acquisition system (5122 PCI National Instrument, 14-bit, 100 MHz bandwidth) and a custom-written LabVIEW program analyzed the data.

5.4 Results and discussion

5.4.1 Selection of absorption lines

The accuracy and precision of the experimental results obtained through the Wavelength Modulation Spectroscopy (WMS) technique are highly affected by the interference of other molecular species. Therefore, we conducted a HITRAN simulation under our experimental conditions, including a path length of 75 meters, a temperature of 296K, and a pressure of 100 Torr. The simulation revealed that the selected absorption lines of NO and OCS at 1900.0706 cm^{-1} and 1899.9756 cm^{-1}, respectively, are free from interference from other abundant gas molecules such as water (H_2O), carbon dioxide (CO_2), and methane (CH_4) (Figure 5.2). The absorption lines of NO and OCS were chosen based on their high line intensity of 2.32 ×10-20 $cm^{-1}/(molecule/cm^{-2})$ and 4.11 × 10-21 $cm^{-1}/(molecule/cm^{-2})$, respectively, according to the HITRAN database [20]. These intensity values are the highest among all other absorption lines in the spectral region covered by the EC-QCL system. Hence, our results demonstrate the potential of using the WMS approach for high-sensitivity monitoring of real atmospheric samples.

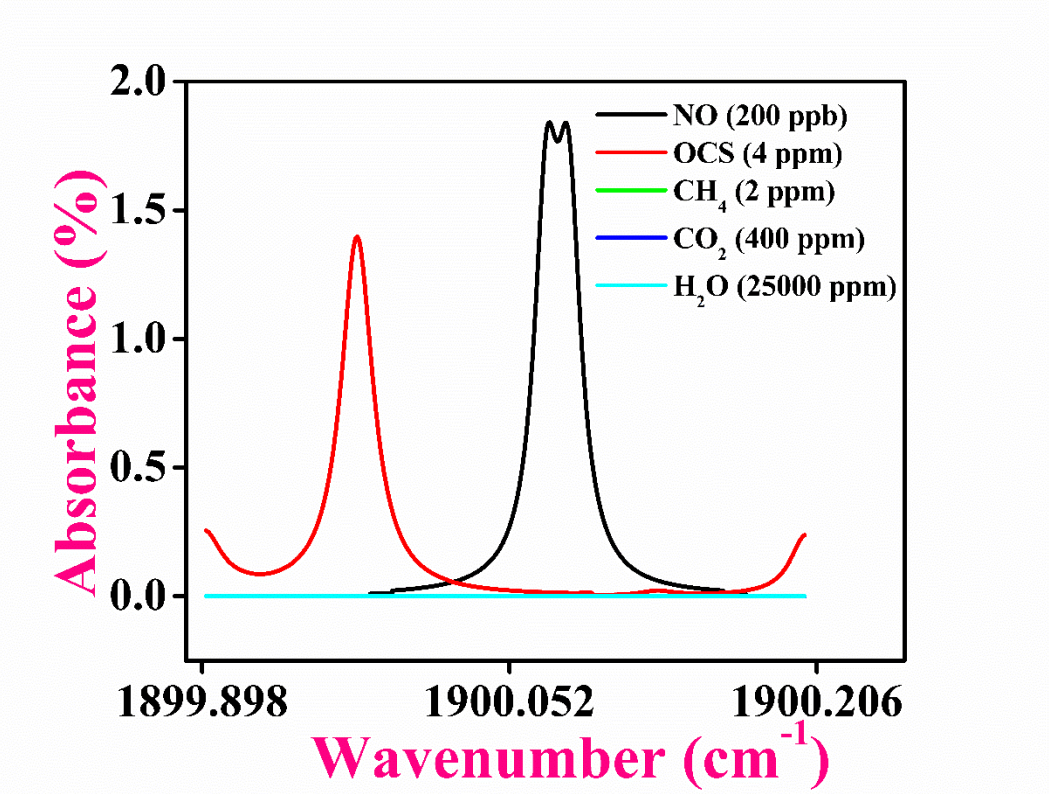

Fig. 5.2- HITRAN simulation of absorption lines of NO and OCS at the experimental conditions of pressure 100 Torr, optical pathlength of 76 m and temperature 296 K showing no spectral interferences of other atmospheric gases like water (H_2O), carbon dioxide (CO_2), methane (CH_4).

5.4.2 Optimization of 2f-WMS signal

The optimal modulation index (m) of the 2f-Wavelength Modulation Spectroscopy (WMS) signal is well-known to be achieved at $m = \Delta v/\gamma = 2.2$, where Δv represents the modulation depth and γ is the half-width half maximum at atmospheric pressure of absorption lines. However, in our study, the γ values of NO and OCS are 0.0567 cm^{-1} atm^{-1} and 0.952 cm^{-1} atm^{-1}, respectively, which implies that the ideal Δv values for NO and OCS are around 0.124 cm^{-1} and 0.209 cm^{-1}, respectively, to maximize the signal-to-noise ratio. Unfortunately, due to the limitations of the current modulation system in our EC-QCL setup, we can only achieve a maximum modulation depth (Δv) of 0.0833 cm^{-1}. To obtain the 2f-WMS signal with the maximum signal-to-noise ratio, we optimized the experimental parameters such as pressure and modulation voltage. Specifically, we experimented with various modulating voltages for both NO and

OCS at a certain pressure, as shown in Figures 5.3a and 5.4a. Our results revealed that the 2f-amplitude increased with an increase in the modulating voltage, but beyond a certain point, it started to decrease due to excessive wavelength modulation. We determined that the optimal modulating voltages for NO and OCS were 2.2 Volt and 2.8 Volt, respectively. Additionally, we conducted similar experiments for pressure optimization by varying the pressure while keeping the modulating amplitude constant. Figures 5.3b and 5.4b illustrate the behaviour of the 2f-output signal for both NO and OCS under different pressures. Our results showed a similar trend for both gases, and we determined that the optimized pressure for both NO and OCS was 100 Torr.

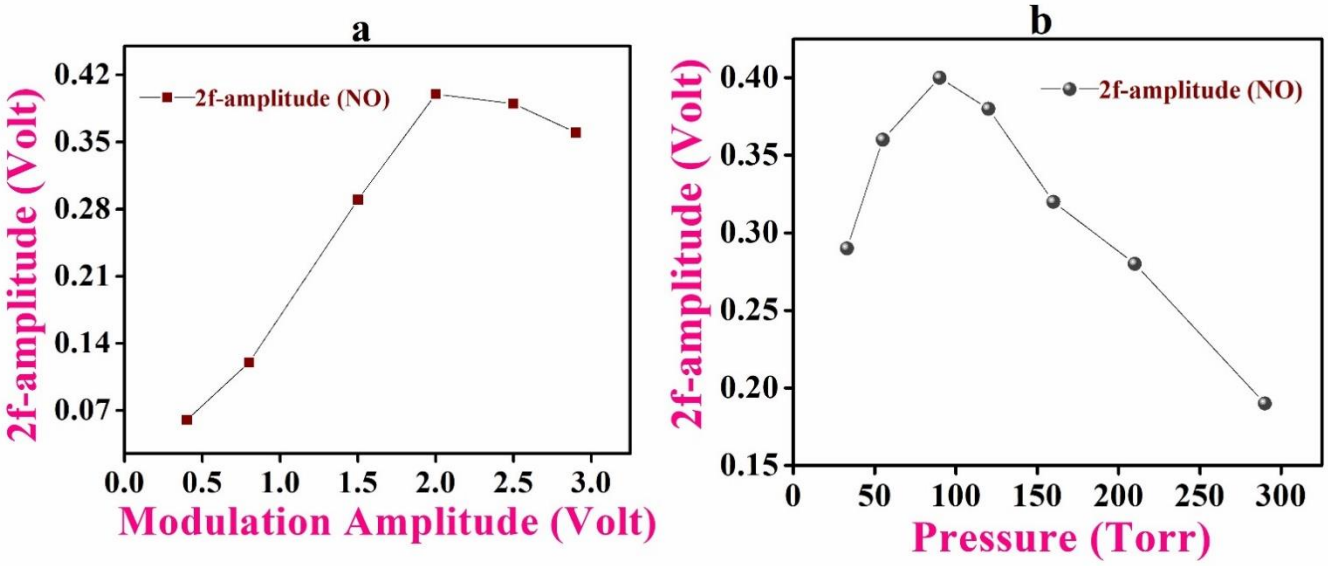

Fig.- 5.3.- (a)Variation of WMS-2*f* output signal at 66 ppm of NO when scanning spectrum centred at 1900.0706 cm^{-1} for different modulating voltages at the pressure of 100 Torr. (b) Amplitude of the WMS-2*f* spectra for 66 ppm of NO as a function gas pressure.

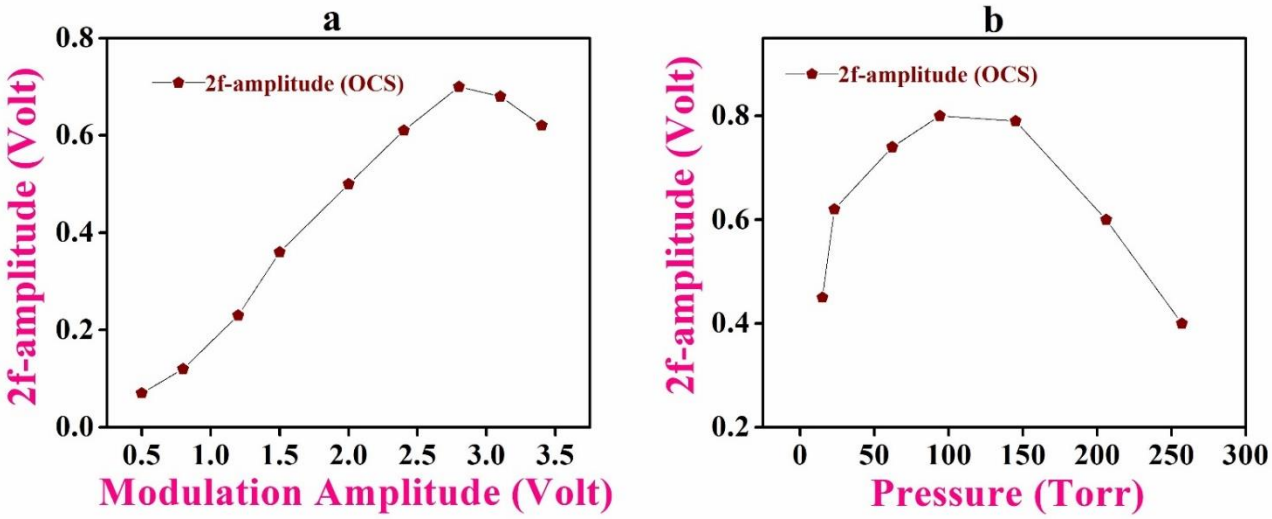

Fig.- 5.4. (a)A plot of 2*f* voltage amplitude for 1000 ppm of OCS when scanning spectrum centred at 1899.9756 cm^{-1} against different modulating voltages at the pressure of 100 Torr. (b) Variation of the 2*f* spectra amplitude for1000 ppm of OCS against the gas pressure.

Following optimizing the parameters for the WMS scheme, we measured the signals of different modulation harmonics for a gas mixture with a known concentration of NO and OCS species. The 1*f*, 2*f*, and 3*f* spectra of NO and OCS are depicted in Figure 5.5 at a working pressure of 100 Torr with a mixing ratio of 100 ppm NO and 1000 ppm OCS.

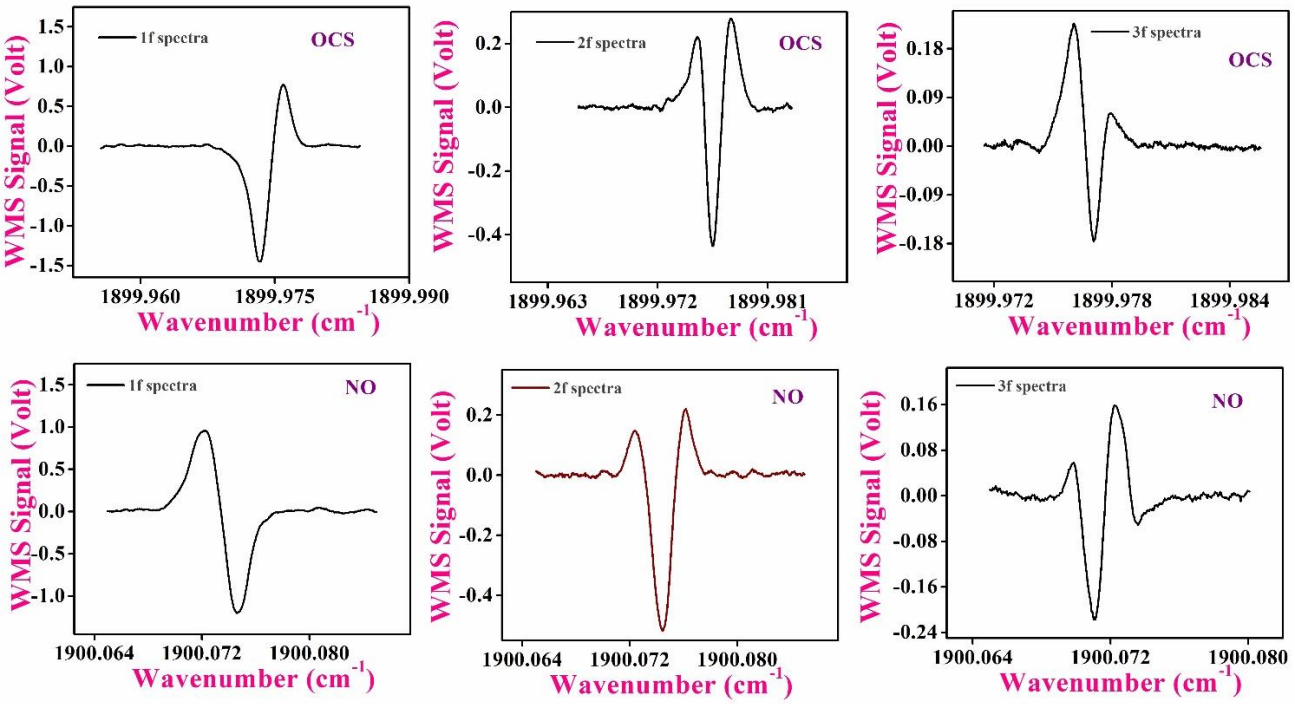

Fig. – 5.5. Representation of 1st, 2nd and 3rd harmonics (i.e 1*f*, 2*f*, and 3*f*) of the output WMS signals for the selected absorption lines of NO and OCS at the optimized modulation voltage of 2.2 V for NO and 2.8 V for OCS and working pressure of 100 Torr with mixing ratio of 100 ppm NO and 1000 ppm OCS.

5.4.3 Calibration of 2f-WMS signal

The output signal of Wavelength Modulation Spectroscopy (WMS) is influenced by various experimental parameters such as sample concentration, optical power, electronic gain, and detection phase. Therefore, to ensure accurate measurements, it is necessary to calibrate the WMS signal using gas samples with known concentrations of the target molecules under optimized experimental conditions. To this end, we performed calibration experiments using known concentrations of NO and OCS at the optimized experimental conditions. We plotted the resulting output 2f signals against the concentrations of NO and OCS to generate calibration curves, as shown in Figures 5.6a and 5.6b. Our calibration experiments yielded a good linear correlation for both NO and OCS, which will enable us to accurately calculate the concentrations of unknown gas samples.

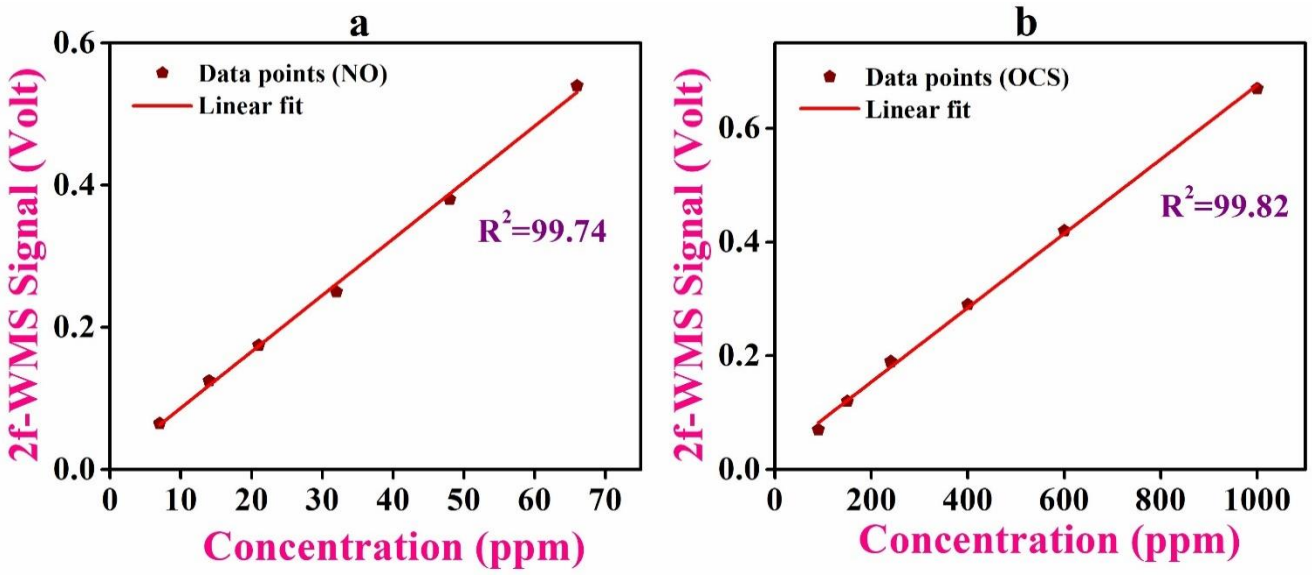

Fig.- 5.6. Calibration curves representing the amplitude of the WMS-2*f* signal for the different mixing ratios of NO (a) and OCS (b). The red line shows the linear fit of the data points.

5.4.4 Allan Variance test

Next, we performed the Allan Variance test [21] to investigate the system's stability and optimize the integration time at our experimental conditions. In this test, we continuously acquired spectra for approximately 30 minutes using an empty cell and analyzed the resulting data. Our analysis revealed that the Allan Variance decreased as we increased the integration time up to an optimum time of 176 seconds, as shown in Figure 5.7. However, for integration times larger than this, the Allan Variance increased due to a shift from the white noise region to the drift-dominated region. These results demonstrate the importance of selecting an appropriate integration time for achieving optimal stability in our system.

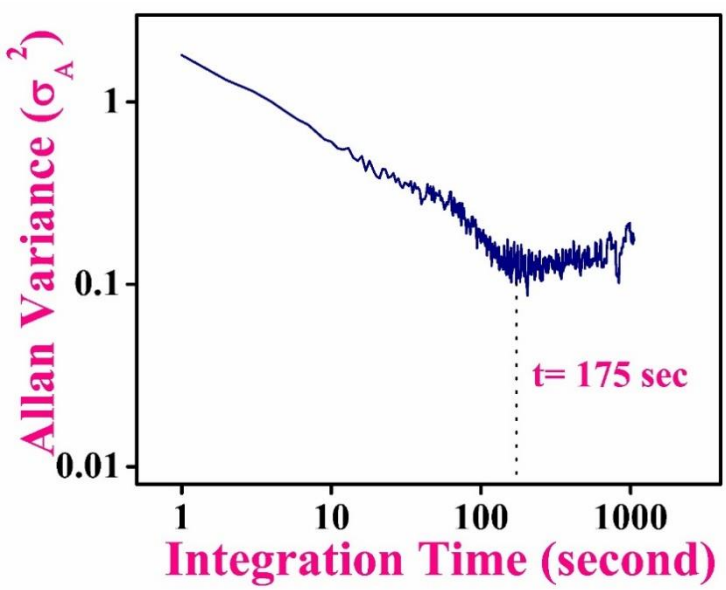

Fig.5.7-Allan Variance test showing the stability of our experimental system and the optimal integration time.

5.4.5 Comparison signal-to-noise ratio between DAS AND WMS techniques

Further, in order to test the effectiveness of the WMS system for simultaneous probing of NO and OCS, we conducted experiments using both direct absorption spectroscopy (DAS) and WMS techniques for different concentrations of the gases. As seen in Figure 5.8, the signal-to-noise ratios for NO and OCS were 9 and 6, respectively, when using direct spectra at mixing ratios of 40 ppm and 200 ppm. However, when using the 2f spectra of WMS, we observed signal-to-noise ratios of 113 for NO and 56 for OCS. This significant difference in signal-to-noise ratios is strong evidence of the higher sensitivity of the WMS technique over DAS. We also determined the detection limits for NO and OCS using the calibration curve in Figure 5.6 and found them to be 300 ppb for NO and 3 ppm for OCS under our experimental conditions. These detection limits were calculated based on the standard deviation of the output WMS signal, which represents the minimum signal that can be detected. Next, we also compared the sensitivities of the reported results on NO and OCS obtained with various techniques in Table 5.1. It is worth noting that the WMS system we used eliminates

the need for critical optical alignment and extended data analysis, unlike cavity-enhanced absorption techniques and other previously employed methods that require relatively critical and time-consuming optical alignment. The WMS approach also eliminates low-frequency noise from the laser source and uses a more compact and simpler optical setup. Additionally, our 2f-WMS system is capable of quickly monitoring NO and OCS in a single laser scan of approximately 0.20 cm-1 across the absorption features, providing another significant advantage compared to other preferred techniques. Therefore, coupling the WMS system with a robust astigmatic cell could lead to a compact and field-deployable prototype sensor for fast and simultaneous monitoring of NO and OCS in harsh real-world environmental conditions with high sensitivity and selectivity.

Table-5.1

Comparison of sensitivity of different works with different techniques.

Authors	Light Source	Techniques employed	Minimum detectable concentration
Geoffrey C. Toon *et al* [23]	MkIV instrument	Fourier Transform Infra-Red (FTIR) Spectrometer	*
Mohammad Reza Mohebbifar *et al* [24]	CO_2 laser (9.2–11.4 μm.)	Laser photoacoustic spectroscopy	3 ppb (OCS)
D.D. Nelson *et al* [26]	quantum cascade laser (5.26 μm)	Tunable Infrared Laser Differential Absorption Spectroscopy	1 ppb (NO)
D. Halmer *et al* [27]	CO laser (4.75 to 5.5 μm)	Cavity leak-out spectroscopy (CALOS)	7 ppt (OCS)
Karol Krzempek *et al* [25]	quantum cascade laser (5.26 μm)	Telecom-fiber-based Mach-Zehnder Interferometer	1000 ppm (NO)

Jacek Wojtas [21]	quantum cascade laser (2.25–16 µm)	Cavity Enhanced Absorption Spectroscopy (CEAS)	30 ppb (NO) 250 ppb (OCS)
Present Study	quantum cascade laser (5.2 µm)	Wavelength Modulation Spectroscopy (WMS)	300 ppb (NO) 3 ppm (OCS)

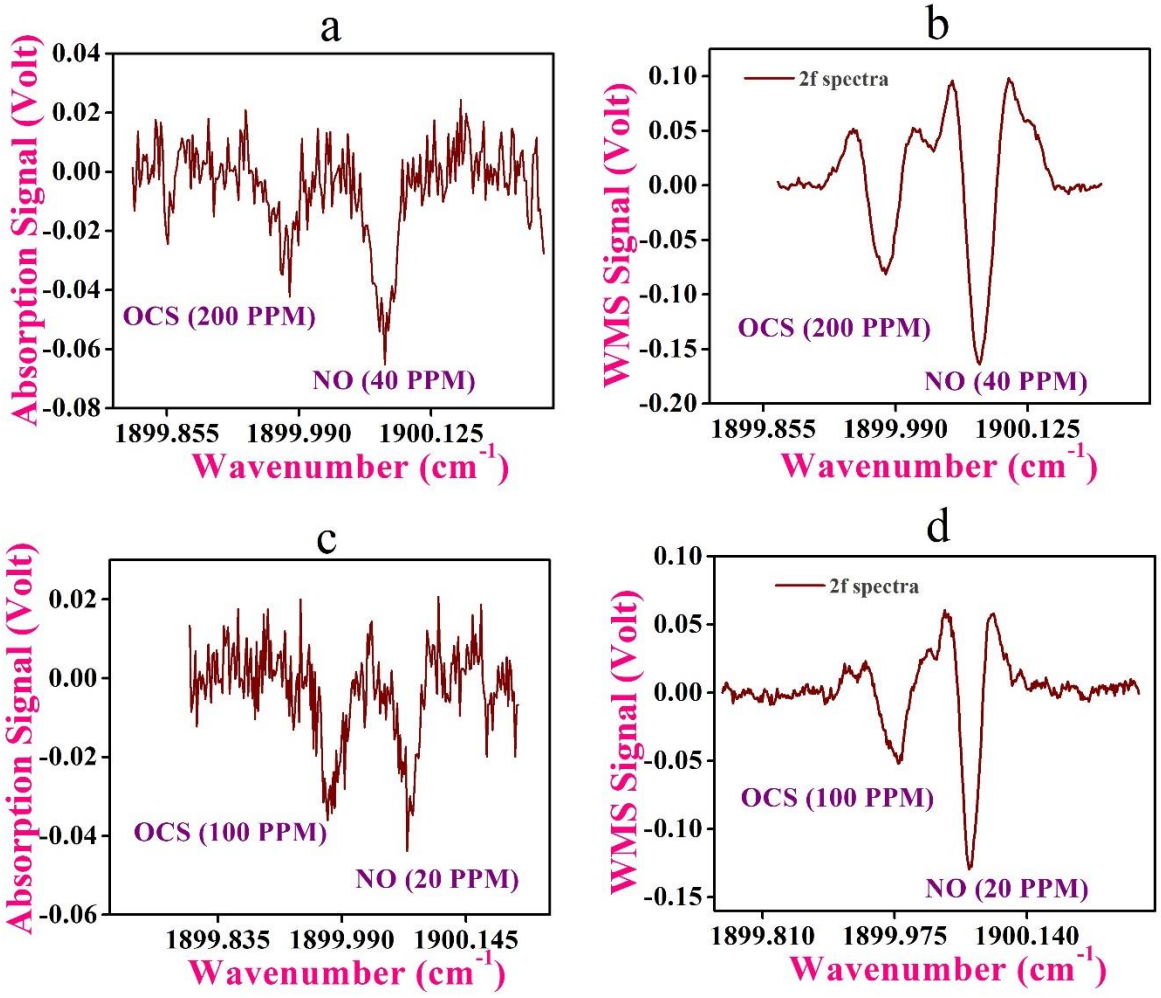

Fig. 5.8.- Simultaneous probing using direct (a & c) and WMS (b & d) techniques with concentrations of 40 ppm and 200 ppm (a & b) and 20 ppm and 100 ppm (c & d) for NO and OCS, respectively.

5.5 Conclusion

In this chapter, we have discussed about the development and demonstration of the 2*f*-WMS detection strategy combining a mid-IR cw EC-QCL and an astigmatic cell for simultaneous probing of NO and OCS molecular species. We utilized the HITRAN simulation to select and simultaneously probe the interference-free strongest absorption lines of the NO and OCS and thereby achieved the sensitivity at the level of 300 ppb for NO and 3 ppm for OCS with a pathlength of 76 m. We performed the Allan Variance test in an empty cavity for about 30 minutes and determined the optimal integration time of 176 seconds. We have also compared the WMS technique with the direct absorption techniques, showing the superiority of the WMS method which has a high potential to be used as a field-deployed sensor for routine monitoring of atmospheric NO and OCS concentrations at various locations.

5.6 References

[1] Zhang S, Liu W, Zhang Y, Shu X, Yu D, Kan R, Dong J, Geng H, Liu J 2010 Gas leakage monitoring with scanned-wavelength direct absorption spectroscopy *Chin. Opt. Lett.* **8** 443-6.

[2] Du Y, Peng Z, Ding Y 2018 High-accuracy sinewave-scanned direct absorption spectroscopy *Opt. express* **26** 29550-60.

[3] Hancock G, Van Helden JH, Peverall R, Ritchie GA, Walker RJ 2009 Direct and wavelength modulation spectroscopy using a cw external cavity quantum cascade laser *Appl. Phys. Lett.* **94** 201110.

[4] Chen X, Yang CG, Hu M, Shen JK, Niu EC, Xu ZY, Fan XL, Wei M, Yao L, He YB, Liu JG 2018 Highly-sensitive NO, NO_2, and NH_3 measurements with an open-multipass cell based on mid-infrared wavelength modulation spectroscopy *Chinese Phys.* B. **27** 040701.

[5] Schilt S, Thévenaz L 2004 Experimental method based on wavelength-modulation spectroscopy for the characterization of semiconductor lasers under direct modulation *Appl. Opt.* 2004 **43** 4446-53.

[6] Li H, Rieker GB, Liu X, Jeffries JB, Hanson RK 2006 Extension of wavelength-modulation spectroscopy to large modulation depth for diode laser absorption measurements in high-pressure gases *Appl. Opt.* **45** 1052-61.

[7] Pal M, Maity A, Pradhan M 2018 A continuous-wave quantum cascade laser near 7.5 μm combined with 2f-wavelength modulation spectroscopy for trace monitoring of ambient CH4 concentrations *Laser Phys.* **28** 105702.

[8] Maity A, Pal M, Maithani S, Banik GD, Pradhan M 2018 Wavelength modulation spectroscopy coupled with an external-cavity quantum cascade laser operating between 7.5 and 8 μm *Laser Phys. Lett.* **15** 045701.

[9] Dimitriades B 1972 Effects of hydrocarbon and nitrogen oxides on photochemical smog formation *Environ. Sci. & Technol.* **6** 253-60.

[10] McCurdy MR, Sharafkhaneh A, Abdel-Monem H, Rojo J, Tittel FK 2011 Exhaled nitric oxide parameters and functional capacity in chronic obstructive pulmonary disease *J. Breath Res*. **5** 016003.

[11] Seo HJ, Jeong RH, Boo JH, Song J, Boo JH 2017 Study on chemical removal of nitric oxide (NO) as a main cause of fine dust (air pollution) and acid rain *Appl. Sci. Converg. Technol*. **26** 218-22.

[12] Chao X, Jeffries JB, Hanson RK 2013 Development of laser absorption techniques for real-time, in-situ dual-species monitoring (NO/NH_3, CO/O_2) in combustion exhaust *Proc. Combust. Inst*. **34** 3583-92.

[13] Shi C, Wang D, Wang Z, Ma L, Wang Q, Xu K, Chen SC, Ren W 2017 A mid-infrared fiber-coupled QEPAS nitric oxide sensor for real-time engine exhaust monitoring *IEEE Sens. J.* **17** 7418-24.

[14] Som S, Banik GD, Maity A, Chaudhuri S, Pradhan M 2018 Exhaled nitric oxide as a potential marker for detecting non-ulcer dyspepsia and peptic ulcer disease *J. Breath Res*. **12** 026005.

[15] Bakhirkin YA, Kosterev AA, Curl RF, Tittel FK, Yarekha DA, Hvozdara L, Giovannini M, Faist J. 2006 Sub-ppbv nitric oxide concentration measurements using cw thermoelectrically cooled quantum cascade laser-based integrated cavity output spectroscopy *Appl. Phys.* B. 2006 **82** 149-54.

[16] Sumizawa H, Yamada H, Tonokura K 2010 Real-time monitoring of nitric oxide in diesel exhaust gas by mid-infrared cavity ring-down spectroscopy *Appl. Phys.* B. **100** 925-31.

[17] Brühl C, Lelieveld J, Crutzen PJ, Tost H 2012 The role of carbonyl sulphide as a source of stratospheric sulphate aerosol and its impact on climate *Atmos. Chem. Phys.* **12** 1239-53.

[18] Kosterev A, Wysocki G, Bakhirkin Y, So S, Lewicki R, Fraser M, Tittel F, Curl RF 2008 Application of quantum cascade lasers to trace gas analysis *Appl. Phys. B*. **90** 165-76.

[19] Li, Hejie, Gregory B. Rieker, Xiang Liu, Jay B. Jeffries, and Ronald K. Hanson. "Extension of wavelength-modulation spectroscopy to large modulation depth for diode laser absorption measurements in high-pressure gases." *Applied optics* 45, no. 5 (2006): 1052-1061.

[20] Rothman LS *et al*.2005 The HITRAN 2004 molecular spectroscopic database *J. Quant. Spectrosc. Radiat. Transfer.* **96** 139-204.

[21] Werle PO, Mücke R, Slemr F 1993 The limits of signal averaging in atmospheric trace-gas monitoring by tunable diode-laser absorption spectroscopy (TDLAS) *Appl. Phys. B* **57** 131-9.

[22] Wojtas, J 2015 Application of cavity enhanced absorption spectroscopy to the detection of nitric oxide, carbonyl sulphide, and ethane—breath biomarker of serious diseases *Sensors* **6** 14356-69.

[23] Toon GC, Blavier JFL and Sung K 2018 Atmospheric carbonyl sulfide (OCS) measured remotely by FTIR solar absorption spectrometry *Atmos. Chem. Phys.* **3** 1923-44.

[24] Mohebbifar MR 2021 Ppb level detection of carbonyl sulfide and ethene and study resonant frequencies using laser photoacoustic spectroscopy. *Microw. Opt. Technol. Lett.*, **10** 2517-22.

[25] Krzempek K, Dudzik G, Nikodem M, Wysocki G and Abramski K 2017 Photothermal detection of NO molecules using a 5.2 μm quantum cascade laser and a simple fiber-based interferometer. *2017 Conference on Lasers and Electro-Optics Europe & European Quantum Electronics Conference (CLEO/Europe-EQEC)* (1-1). IEEE.

[26] Nelson DD, Shorter JH, McManus JB, and Zahniser MS 2002. Sub-part-per-billion detection of nitric oxide in air using a thermoelectrically cooled mid-infrared quantum cascade laser spectrometer *Appl. Phys. B* **2** 343-50.

[27] Halmer D, Von Basum G, Hering P and Mürtz M 2005 Mid-infrared cavity leak-out spectroscopy for ultrasensitive detection of carbonyl sulfide *Opt. Lett.* **17** 2314-16.

Chapter-6

An EC-QCL based dual-species (CH_4/ N_2O) detection method at 7.8 μm in mid-IR region for simultaneous applications of atmospheric monitoring and breath diagnostics

Contents

6.1 Introduction……..…..113

6.2 Experimental section……114

6.3 Results and discussions……..…116

6.3.1 Selections of absorption lines……....116

6.3.2 Optimization of 2f-WMS signal……... 117

6.3.3 Calibration of 2f-WMS signal……....119

6.3.4 Allan Variance test…….…120

6.3.5 Real time monitoring of CH_4 and N_2O……....121

6.4 Conclusion…….....122

6.5 References…….. 123

6.1 Introduction

Methane (CH_4) and nitrous oxide (N_2O), the two most prevalent atmospheric greenhouse gases next to carbon dioxide (CO_2), contribute drastically to climate change and global warming [1-3]. CH_4 and N_2O have familiar emission sources like agricultural processes, industrial production, tropical forests, and fossil fuel combustion; thus, the atmospheric concentrations of both species have significantly increased in the last few decades [4-9]. N_2O plays a significant role in medical sciences, especially in surgery and dentistry, for its anaesthetic and pain-reducing effects [10-11]. Exhaled breath N_2O also indicates aerobic nitrification and denitrification process in the human gastrointestinal tract [12]. Conversely, breath CH_4 is associated with bloating gas, and constipation-related diseases, such as constipation-predominant irritable bowel syndrome (IBS-C) [13-14]. Given these, the real-time sensitive and molecule-specific detection of CH_4 and N_2O is of significant interest in widespread environmental monitoring and biomedical diagnostics applications. In the past, various research groups have used numerous optical spectroscopic methods such as cavity ring-down spectroscopy (CRDS), quartz-enhanced photoacoustic spectroscopy (QEPAS), and optical-feedback cavity-enhanced absorption spectroscopy (OF-CEAS) for monitoring of these two molecular species [15-20]. Nevertheless, developing a simple, compact, ultra-sensitive optical detection method with a simple optical alignment for simultaneous monitoring of CH4 and N2O in ambient air and human exhaled breath at high temporal resolution remains challenging. Moreover, the detection strategy should have field-deployable capabilities to measure short-time fluctuations and fluxes of the constituents in harsh environmental conditions.

Tunable diode lasers combined with second harmonic detection wavelength modulation spectroscopy (2*f*-WMS) have recently been used as one of the most versatile techniques in trace gas sensing [21-22]. In WMS absorption measurements, a high-frequency (kHz) sinusoidal wave is injected into the laser source for modulation, and this modulation shifts the signal to a higher bandwidth region. A lock-in-amplifier detects the output harmonics components following demodulation of the signal, which eliminates the low-frequency laser noise (1/f noise). The second

harmonic (2*f*) component of the output signal is used as a detection signal to retrieve the sample concentrations with frequent standard calibration. However, the recent technological advancement of continuous-wave (cw) external-cavity (EC) quantum cascade laser (QCL) in the mid-IR molecular fingerprint region draws significant attention in the field of atmospheric monitoring. It is noteworthy to mention that several unique features of the EC-QCL sources, such as extremely narrow linewidth (~0.0002 cm^{-1}), broad tunability, and highly compact and room-temperature operation, makes them more convenient light source as compared to other excitation sources in the mid-IR regions for high-resolution spectroscopic applications [23]. In this context, combining a WMS detection strategy and a cw-EC-QCL technology would be a promising approach for developing a compact and robust optical method with high molecular sensitivity and specificity. The methodology will have excellent capabilities for precise and simultaneous monitoring of various trace gases like CH_4 and N_2O in various applications, including medical diagnostics and environmental monitoring.

In this chapter, we have discussed on the development of a dual-species (CH_4 / N_2O) monitoring optical detection method at 7.8 µm combining an astigmatic multipass cell and a *cw* EC-QCL light source. The system exploits the fundamental principle of 2*f*-WMS and can quantitatively monitor CH4 and N2O concentrations in ambient air and exhaled breath samples with high sensitivity and molecular selectivity. High-resolution 2*f*-WMS spectra of CH_4 and N_2O are recorded by probing the interference-free absorption lines in a single QCL scan of ~ 0.06 cm^{-1}.

6.2 Experimental Section

A schematic diagram of the dual-species monitoring system coupled with a lightweight astigmatic multipass cell (AMAC-76LW, Aerodyne Research, USA) with a pathlength of 76 m is depicted in Fig. 6.1. A room-temperature operated *cw* EC-QCL (MHF-41078; Daylight Solutions, USA) centred at 7.8 µm wavelength with mode-hop-free (MHF) tunability was used as a compact and perfect excitation source to design the current sensor. An acousto-optic modulator (AOM) (AGM-405B11M) was utilized to diffract the QCL beam into two sub-beams, where one part of the beam was directed

into the wavemeter (771B-MIR, Bristol Instruments) for the simultaneous monitoring of the wavenumber with an accuracy of 0.001 cm^{-1}. The second part of the QCL beam was directed into the multipass cell through the window made up of BaF_2 to achieve the maximum path length. A visible He-Ne laser source operating at 633 nm was employed in the setup for the precise and accurate alignment of the QCL beam into the cell. The laser light exiting the cell was focused on an MCT detector (PVI-4TE-8-1X1; Vigo System S.A.) by an off-axis parabolic mirror (OAPM). The optimum pressure inside the cell was controlled by a vacuum pump with a pressure gauge (Pfeiffer vacuum, Model no.- CMR361).

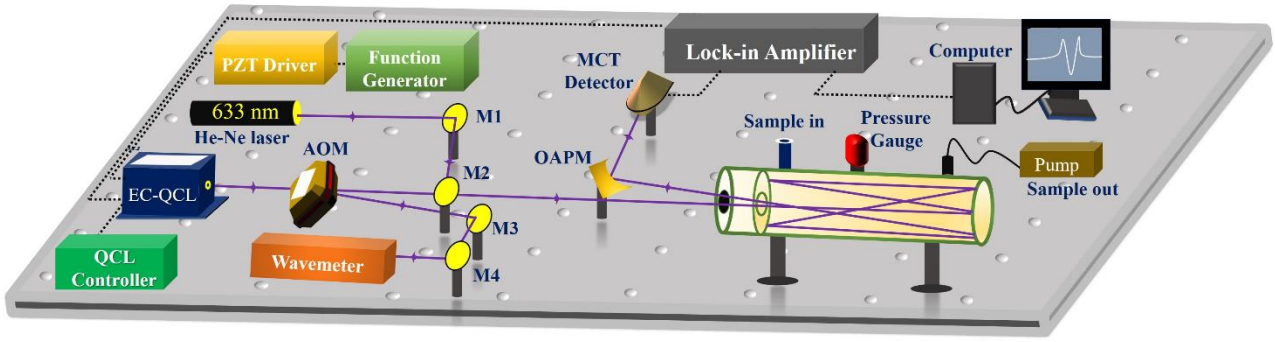

Figure-6.1: - A demonstration diagram for the lab developed astigmatic multipass cell experimental setup coupled with QCL. M1, M2, M3, M4 are the corresponding bending mirrors.

Next, to obtain the precise wavelength modulation signal, we modulated the QCL emitted light with a sine wave with (30 kHz frequency). The output harmonic signal was then demodulated, and the harmonics (1*f*, 2*f*, 3*f*) were separated using a lock-in amplifier (Standford Research Systems SR830 DSP) with a voltage scale of 0.01 V. A piezo-electric driver (MDT693B; Thorlabs) coupled with a function generator (10 V, 2.5 Hz) was used to scan the QCL beam in the selected absorption regions of CH_4 and N_2O. Finally, the demodulated output signal was acquired through a data acquisition system (5122 PCI National Instrument, 14-bit, 100 MHz bandwidth), and a custom-written LabVIEW program analyzed the data.

6.3 Results and Discussion

6.3.1 Selections of absorption lines

To achieve simultaneous and molecule-specific detection of CH_4 and N_2O in ambient air samples, we performed a HITRAN simulation [24] to identify an interference-free spectral region within the tuning range of an EC-QCL. The simulation utilized experimental conditions, including a path length of 76 m, a temperature of 296 K, and a working pressure of 25 Torr. The results of the simulation are presented in Fig. 6.2, which guided our selection of rotational-vibrational absorption lines for CH4 in the v4 band at 1297.8192 cm^{-1}, with a line intensity of 1.13 × 10-20 $cm^{-1}/(molecule/cm^2)$, and for N_2O in the v_1 band at 1297.8314 cm^{-1}, with a line intensity of 1.68 × 10-19 $cm^{-1}/(molecule/cm^2)$. Importantly, these lines are free from absorbance by other common atmospheric molecules such as water (H_2O) and carbon dioxide (CO_2). The resulting narrow spectral window of approximately 0.06 cm^{-1} in the mid-IR region allows for the sensitive and selective detection of CH_4 and N_2O in ambient air samples using a single QCL scan, as we have experimentally demonstrated.

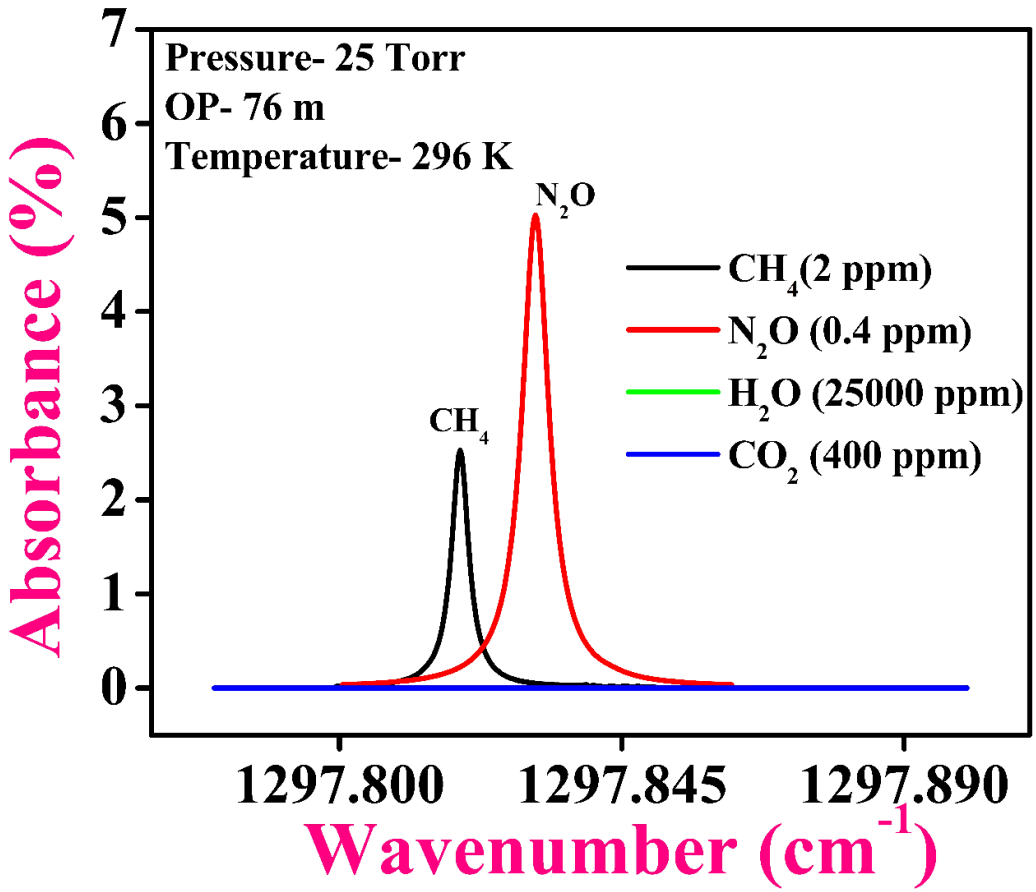

Figure 6.2- Graphical representation of the HITRAN simulation for the spectral lines of CH_4 and N_2O reflecting no interferences of major atmospheric gases like water (H_2O), carbon dioxide (CO_2) at the experimental conditions of pressure 25 Torr, optical pathlength (OP) of 76 m and temperature 296 K.

6.3.2 Optimization of 2f-WMS signal

We employed the WMS detection strategy to achieve a maximum signal-to-noise ratio (SNR) of the output signal amplitude. To optimize this, we varied experimental parameters such as sample pressure and modulation amplitude. We focused on optimizing the sample pressure by adjusting the pressures of CH_4 and N_2O within the multipass cell. We found that increasing the pressure led to an increase in the output 2f-amplitude of the WMS signal, which peaked at a maximum value before gradually decreasing due to excessive broadening. Our experiment showed that the optimized pressure for CH_4 and N_2O was 25 Torr, as demonstrated in Figure 6.3(b). We then proceeded to optimize the modulating voltage by conducting similar experiments. We

observed a similar trend to the pressure optimization, as shown in Figure 6.3(a). However, the optimized modulating voltage for both gases was 2.8 Volts.

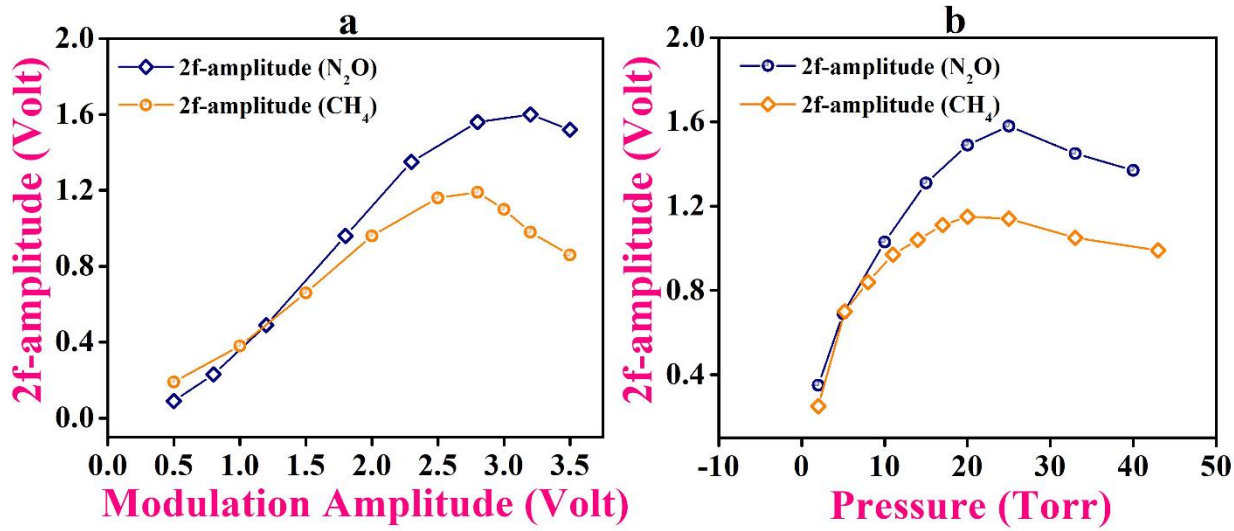

Figure- 6.3.- (a) Variation of 2*f*-WMS output signal at 60 ppm of CH_4 and 20 ppm of N_2O for different modulation voltages during scanning of absorption lines centred at 1297.8192 cm^{-1} and 1297.8314 cm^{-1} for CH_4 and N_2O, respectively with cavity pressure 25 Torr (b) A plot of amplitude of the WMS-2*f* against different gas pressure for 60 ppm of CH_4 and 20 ppm of N_2O.

After refining the experimental conditions for detecting trace amounts of gases using WMS, we proceeded to measure the 1*f*, 2*f*, 3*f* harmonic spectra of CH4 and N2O molecules. These molecules were present in a known concentration of approximately 10 parts per million, and the measurements were taken at a working pressure of 25 Torr. The obtained results are presented in Figure 6.4.

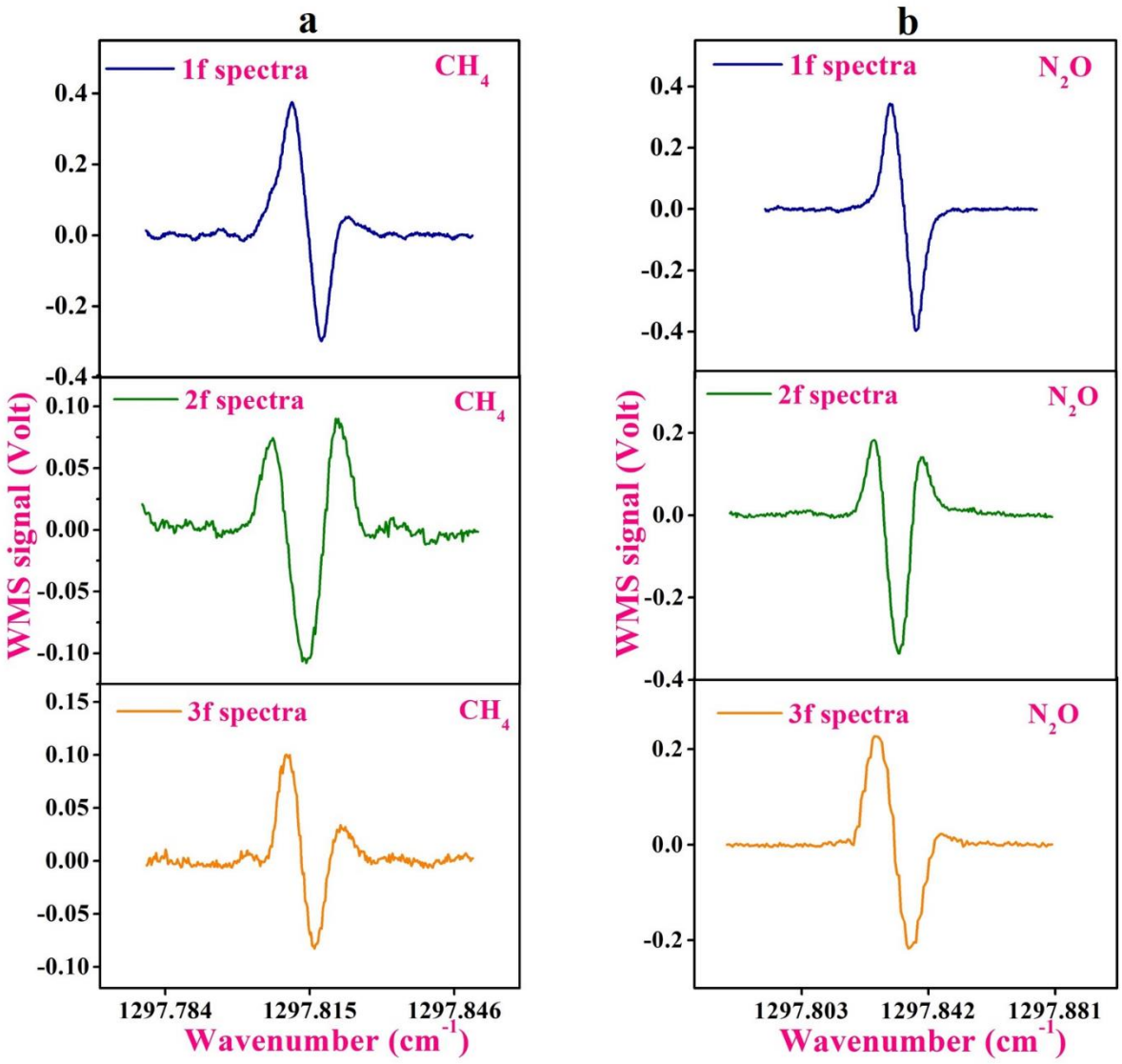

Figure – 6.4. Graphical representation of 1st, 2nd and 3rd harmonics (i.e 1*f*, 2*f*, and 3*f*) spectra of CH_4 (a) and N_2O (b) with mixing ratio of 10 ppm each in the selected absorption lines at optimized modulation voltage of 2.8 V and working pressure of 25 Torr.

6.3.3 Calibration of 2f-WMS signal

To ensure accurate and reliable detection of trace gases using the WMS method, we conducted a comprehensive calibration of the 2f-signal. The goal was to establish a detection method that would be immune to interferences from specific parameters such as optical power and electronic gain during real-time monitoring of gaseous species. The calibration process involved introducing different standard

concentrations of CH_4 and N_2O into the cell, and measuring the resulting 2f-WMS amplitudes. The obtained data was plotted against the sample concentrations, and as shown in Figure 6.5, we achieved excellent linear correlations for both CH_4 and N_2O. These calibration data can be used to accurately calculate the concentration of unknown atmospheric samples, as well as to measure the concentration of CH_4 and N_2O in human exhaled breath.

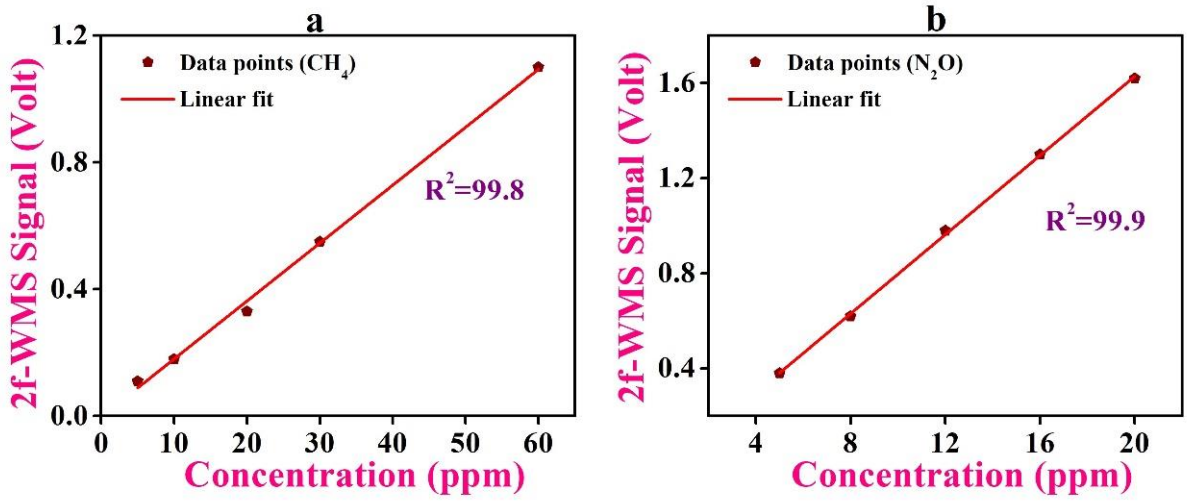

Figure- 6.5. A linear fitted calibration data points showing good linear regression for both CH_4 (a) and N_2O (b) for different gas concentrations against the amplitude of the WMS-2*f* signal.

6.3.4 Allan Variance test

In order to check the stability of our system's performance, we conducted an Allan Variance test, as outlined in [25]. This involved continuously acquiring data from an empty cavity for around 30 minutes, which was then analyzed using a custom-written LabVIEW program. Through this process, we determined that the optimal integration time for our system was up to 88 seconds. However, beyond this point, the Allan Variance (as shown in Figure 6.6) began to increase due to a shift from the 1/f noise region towards the drift-dominated region. This information was crucial in helping us establish the operational limits of our system and ensure the reliable and accurate detection of trace gases.

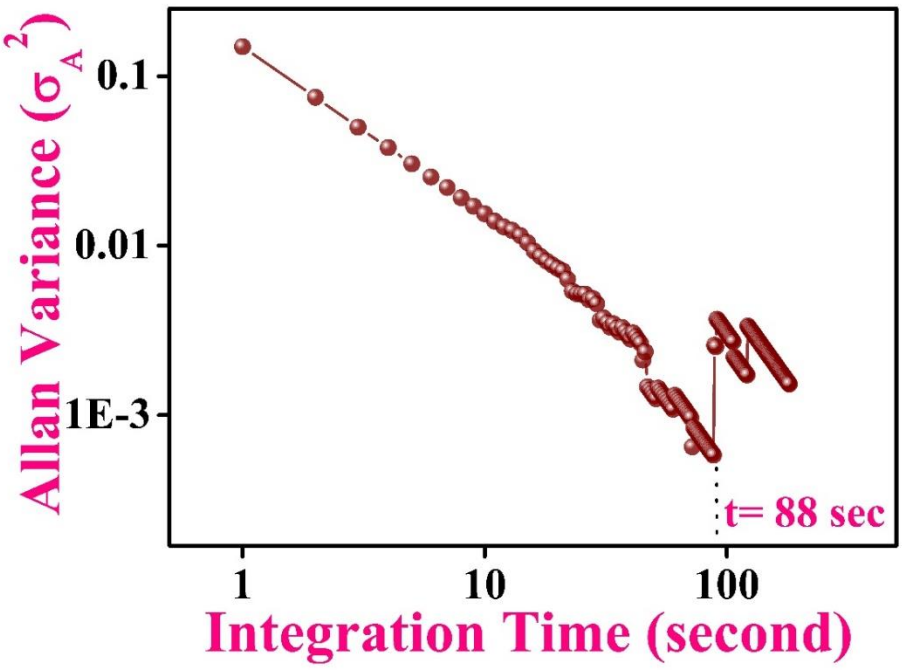

Figure 6.6- Allan Variance plot to test the system performances.

6.3.5 Real time monitoring of CH_4 and N_2O

Finally, to demonstrate the practicality of our lab-developed 2f-WMS optical detection strategy in real-world scenarios, we utilized it in combination with a 7.8 µm cw-EC-QCL source for the simultaneous measurement of ambient and exhaled CH_4 and N_2O mixing ratios. We collected atmospheric air samples from the campus of the S.N. Bose Centre, Kolkata and used the system to measure the ambient concentrations of CH_4 and N_2O, as shown in Figure 6.7(a). The concentrations of CH_4 and N_2O were determined to be (1.95 ± 0.05) ppm and (490 ± 8) ppb, respectively, which are typical values for a normal environment [26]. Furthermore, we conducted simultaneous measurements of CH_4 and N_2O in normal human exhaled breath (Figure 6.7 (b)) using the same procedure. The concentrations of CH_4 and N_2O in exhaled breath were found to be (2.25 ± 0.07) ppm and (290 ± 7) ppb, respectively. Further, to assess the sensitivity of our developed system, we estimated the typical detection limits (DLs) of CH_4 and N_2O based on the standard deviation of the output WMS signal, which is the minimum voltage that can be achieved using the calibration curve. With a data acquisition time of 0.20 sec, we achieved DLs of 30 ppb and 6 ppb for CH_4 and N_2O,

respectively. These results demonstrate the high sensitivity of our 2f-WMS detection method combined with an EC-QCL, allowing for simultaneous monitoring of CH_4 and N_2O in both ambient air and highly complex mixtures such as exhaled breath samples with high molecular specificity.

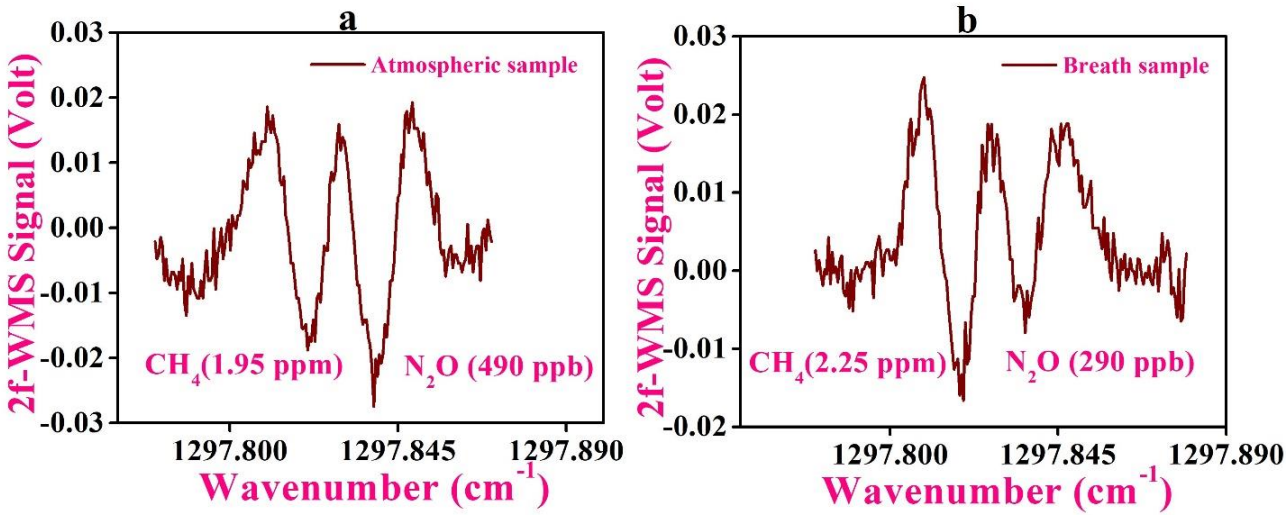

Figure-6.7. Measurements of CH_4 and N_2O concentrations in (a) atmosphere and (b) human breath at optimized experimental conditions. The concentration of CH_4 and N_2O were found to be (a) (1.95 ± 0.05) ppm and (490 ± 8) ppb in atmosphere and (b) (2.25 ± 0.07) ppm and (290 ±7) ppb in human breath, respectively.

6.4 Conclusion

In this chapter, a high-sensitive optical detection method exploiting the 2*f*-WMS detection strategy coupled with an astigmatic multipass cell and a *cw* EC-QCL operating at 7.8 µm has been demonstrated. The system can simultaneously probe the interference-free and high-resolution absorption lines of CH_4 and N_2O in a single laser scan and can monitor both the species in ambient air and breath samples in the levels of ppb. Therefore, the current lab-developed 2f-WMS detection-based optical method can be upgraded as a field-deployable sensor for real-time, simultaneous and continuous monitoring of CH_4 and N_2O in various applications including non-

6.5 References

[1] G.K. Heilig, The greenhouse gas methane (CH_4): Sources and sinks, the impact of population growth, possible interventions, Popul. Environ. 16 (1994) 109-137.

[2] E. D. Schulze, S. Luyssaert, P. Ciais, A. Freibauer, I. A. Janssens, J. F. Soussana, P. Smith, J. Grace, I. Levin, B. Thiruchittampalam, and M. Heimann, Importance of methane and nitrous oxide for Europe's terrestrial greenhouse-gas balance, Nat. Geosci. 2 (2009) 842-850.

[3] M. Keller, D. J. Jacob, S. C. Wofsy, and R. C. Harriss, Effects of tropical deforestation on global and regional atmospheric chemistry, Clim. Change 19 (1991) 139-158.

[4] I. Jang, S. Lee, J. H. Hong, and H. Kang, Methane oxidation rates in forest soils and their controlling variables: a review and a case study in Korea, Ecol. Res. 21 (2006) 849-854.

[5] T. Pérez, S. E. Trumbore, S. C. Tyler, E. A. Davidson, M. Keller, and P. B. De Camargo, Isotopic variability of N_2O emissions from tropical forest soils, Glob. Biogeochem. Cycles 14 (2000) 525-535.

[6] I. Mappé, L. Joly, G. Durry, X. Thomas, T. Decarpenterie, J. Cousin, N. Dumelie, E. Roth, A. Chakir, and P. G. Grillon, A quantum cascade laser absorption spectrometer devoted to the insitu measurement of atmospheric N_2O and CH_4 emission fluxes, Rev. Sci. Instrum. 84 (2013) 023103.

[7] C. B. Hedley, S. Saggar, and K. R. Tate, Procedure for fast simultaneous analysis of the greenhouse gases: methane, carbon dioxide, and nitrous oxide in air samples, Commun. Soil Sci. Plant Anal. 37 (2006) 1501-1510.

[8] W. Yuesi, and W. Yinghong, Quick measurement of CH_4, CO_2 and N_2O emissions from a short-plant ecosystem, Adv. Atmos. Sci. 20 (2003) 842-844.

[9] B. Johnson, Sarah E., O. R. Angeles, M. C. R. Alberto, and R. J. Buresh, Simultaneous minimization of nitrous oxide and methane emission from rice paddy soils is improbable due to redox potential changes with depth in a greenhouse experiment without plants, Geoderma 149 (2009) 45-53.

[10] D. E. Becker, and M. Rosenberg, Nitrous oxide and the inhalation anesthetics, Anesth. Prog. 55 (2008) 124-131.

[11] S. A. Kanagasundaram, L. J. Lane, B. P. Cavalletto, J. P. Keneally, and M. G. Cooper, Efficacy and safety of nitrous oxide in alleviating pain and anxiety during painful procedures, Arch. Dis. Child. 84 (2001) 492-495.

[12] M. Pal, S. Maithani, A. Maity, S. Chaudhuri, and M. Pradhan, Exploring the physiological link of breath N_2O through nitrification and denitrification processes in human gastric juice, J. Breath Res. 13 (2018) 016002.

[13] U. Ghoshal, R. Shukla, D. Srivastava, and U. C. Ghoshal, Irritable bowel syndrome, particularly the constipation-predominant form, involves an increase in Methanobrevibacter smithii, which is associated with higher methane production, Gut and liver 10 (2016) 932-938.

[14] M. Furnari, E. Savarino, L. Bruzzone, A. Moscatelli, L. Gemignani, E. G. Giannini, P. Zentilin, P. Dulbecco, and V. Savarino. J. Gastrointest, Reassessment of the role of methane production between irritable bowel syndrome and functional constipation, Liver Dis. 21 (2012) 157-163.

[15] Q. Wei, B. Li, J. Wang, B. Zhao, and P. Yang, Impact of residual water vapor on the simultaneous measurements of trace CH_4 and N_2O in air with cavity ring-down spectroscopy, Atmosphere 12 (2021) 221.

[16] S. Nishimura, T. Sawamoto, H. Akiyama, S. Sudo, and K. Yagi, Methane and nitrous oxide emissions from a paddy field with Japanese conventional water management and fertilizer application, Glob. Biogeochem. Cycles 18 (2004).

[17] L. M. Bréchet, W. Daniel, C. Stahl, B. Burban, J. Y. Goret, R. L. Salomón, and I. A. Janssens, Simultaneous tree stem and soil greenhouse gas (CO_2, CH_4, N_2O) flux measurements: a novel design for continuous monitoring towards improving flux estimates and temporal resolution, New Phytol. 230 (2021) 2487-2500.

[18] J. R. Christiansen, J. Outhwaite, and S. M. Smukler. Agric, Comparison of CO_2, CH_4 and N_2O soil-atmosphere exchange measured in static chambers with cavity ring-down spectroscopy and gas chromatography, For. Meteorol. 211 (2015) 48-57.

[19] M. Jahjah, W. Ren, P. Stefański, R. Lewicki, J. Zhang, W. Jiang, J. Tarka, and F. K. Tittel, A compact QCL based methane and nitrous oxide sensor for environmental and medical applications, Analyst 139 (2014) 2065-2069.

[20] D. J. Hamilton, and A. J. Orr-Ewing, A quantum cascade laser-based optical feedback cavity-enhanced absorption spectrometer for the simultaneous measurement of CH_4 and N_2O in air, Appl. Phys. B 102 (2011) 879-890.

[21] F. Wang, S. Jia, Y. Wang, and Z. Tang, Recent developments in modulation spectroscopy for methane detection based on tunable diode laser, Appl. Sci. 9 (2019) 2816.

[22] C. Jiang, Y. Liu, B. Yu, S. Yin, and P. Chen, TDLAS-WMS second harmonic detection based on spectral analysis, Rev. Sci. Instrum. 89 (2018) 083106.

[23] A. Kosterev, G. Wysocki, Y. Bakhirkin, S. So, R. Lewicki, M. Fraser, F. Tittel, and R. F. Curl, Application of quantum cascade lasers to trace gas analysis, Appl. Phys. B 90 (2008) 165-176.

[24] L. S. Rothman, I. E. Gordon, Y. Babikov, A. Barbe, D. Chris Benner, P. F. Bernath, M. Birk, L. Bizzocchi, V. Boudon, L. R. Brown, A. Campargue, K. Chance, E. A. Cohen, L. H. Coudert, V. M. Devi, B. J. Drouin, A. Fayt, J. M. Flaud, R. R. Gamache, J. J. Harrison, J. M. Hartmann, C. Hill, J. T. Hodges, D. Jacquemart, A. Jolly, J. Lamouroux, R. J. Le Roy, G. Li, D. A. Long, O. M. Lyulin, C. J. Mackie, S. T. Massie, S. Mikhailenko, H. S. P. Müller, O. V. Naumenko, A. V. Nikitin, J. Orphal, V. Perevalov, A. Perrin, E. R. Polovtseva, C. Richard, M. A. H. Smith, E. Starikova, K. Sung, S. Tashkun, J. Tennyson, G. C. Toon, V. G. Tyuterev and G. Wagner, The HITRAN2012 molecular spectroscopic database, J. Quant. Spectrosc. Radiat. Transfer. 96 (2005) 139-204.

[25] P.O. Werle, R. Mücke R and F. Slemr, The limits of signal averaging in atmospheric trace-gas monitoring by tunable diode-laser absorption spectroscopy (TDLAS), Appl. Phys. B 57 (1993) 131-139.

[26] Stephen A. Montzka, Edward J. Dlugokencky, and James H. Butler, Non-CO2 greenhouse gases and climate change, Nature 476 (2011) 43-50.

Chapter-7

Elucidation of Temperature-Dependent Soil Enzyme Urease Activity and Observation of Deuterium-Enriched Isotopic Resonance Effects

Contents

7.1 Introduction…….127

7.2Results and discussions……...129

7.3 Conclusion…….....134

7.4 Experimental Methods…….....135

7.5 References……....138

7.1 Introduction

Urea is a commonly used nitrogen-containing compound in agriculture, but its excessive use can lead to increased levels of urease activity in farming soil, causing significant problems for soil fertility and the environment by releasing enormous amounts of ammonia (NH_3) and carbon dioxide (CO_2) [1]. Urease is one of the most important enzymes and is found in various soil microbes, fungi, bacteria and plants. It plays a critical role in organic matter mineralization, greenhouse gas emissions and environmental nitrogen transformation [2-4]. In waste water treatment, urease enzymes are essential for the removal of urea [5]. These enzymes also have unique features, providing information about different biological assessments of soils because

the organic content of soil varies according to the atmosphere and different soil types [6-7]. In addition, urease enzyme has received important applications in enzymatic assays along with in medical science, such as the development of urea sensors for clinical measurements of urea in urine, blood and different body fluids [8-9].

Over the past decades, extensive research on the urease-catalyzed hydrolysis of urea has been carried out in various aspects and primarily focused on the reaction kinetics, soil pH, buffer environments and soil moisture content [1,10-11]. But, the effect of temperature on soil urease activity have received a little attention [12-13]. Moreover, early studies have confirmed that the kinetics of enzymatic reactions and cellular growth regulation, including the balance of mitochondrial oxidation and reduction, are influenced by solutions enriched or depleted with deuterium (D) [14-15]. The proportion of heavy (D) and light isotopes (H) has been shown to be a critical factor in the metabolic and physiological processes of plants and animals [16-17]. Moreover, there is a pressing need to explore strategies for optimizing the utilization of urea in soil through the use of urease inhibitors, as well as the regular monitoring of urease-catalyzed hydrolysis under varying environmental conditions. These concerns are particularly salient given the changing atmospheric conditions. In addition, there remains a dearth of research on the impact of urease enzyme in deuterium-enriched soil medium, particularly regarding the isotopic resonance phenomenon [18-19]. The isotopic resonance hypothesis suggests that at some "resonance" isotopic composition of reactants, the kinetics are enhanced or retarded as compared to "off-resonance" conditions. Moreover, how the urease-catalyzed hydrolysis of urea is affected in response to deuterium enrichment in water as well as in soil medium has never been explored and therefore it still remains an open question. Thus, unravelling isotopic resonance involving urease-activity and D-enrichment in soil medium would provide better fundamental understanding of the potential role of D-isotopic composition for urease activation kinetics.

In this chapter, we report the urease activity in soil media under varying temperatures. By examining the impact of different environmental conditions, we sought to better comprehend the hydrolysis process and to track the urease activity at

specific temperature. This approach allowed us to gain a more comprehensive understanding of the factors that influence urease activity in soil, particularly as it relates to temperature variations. In addition, we utilized the D-enriched solution in both standard water medium and in soil medium to explore whether the highly-enriched heavy water (D_2O) is playing a role in either inhibiting or activating urease activity. To accomplish this, we monitored the concentration of the product (CO_2) and two distinct negative isotopic resonances were detected in response to D-enriched solutions in both soil and distilled water media. This observation sheds new light on soil urease activity and the possible role of D_2O as a regulator in urea-urease hydrolysis. Thus, these findings may open new applications in environmental, agricultural and biotechnology along with development of enzymology biochemistry.

7.2 Results and discussions

We first aimed to investigate the effect of urea on the activation of urease-enzyme in soil medium. To do this, we performed urease-catalyzed urea reactions with different concentrations of urea and urease in the soil medium. The reactions were carried out in the ambient air headspace, and the concentration of the product (CO_2) was measured after 1 hour using the high-precision integrated cavity output spectroscopy (IOCS). Our results showed that there was no significant change in the concentration of CO_2 with increasing the urease concentration at a fixed urea concentration (Fig. 7.1a). This indicates that the urease enzyme maintained its continuous catalytic activity under these conditions. However, with increasing the concentration of urea, a significant increase in the product's concentration was observed (Fig. 7.1b). This suggests that urea hydrolysis occurred at a faster rate in the presence of urease enzyme in soil medium. These findings suggest that the concentration of urea plays an important role in the activation of urease enzyme in soil medium. This information could be useful in the development of strategies for optimizing the use of urea in agriculture and consequently to reduce the release of NH_3 and greenhouse gases.

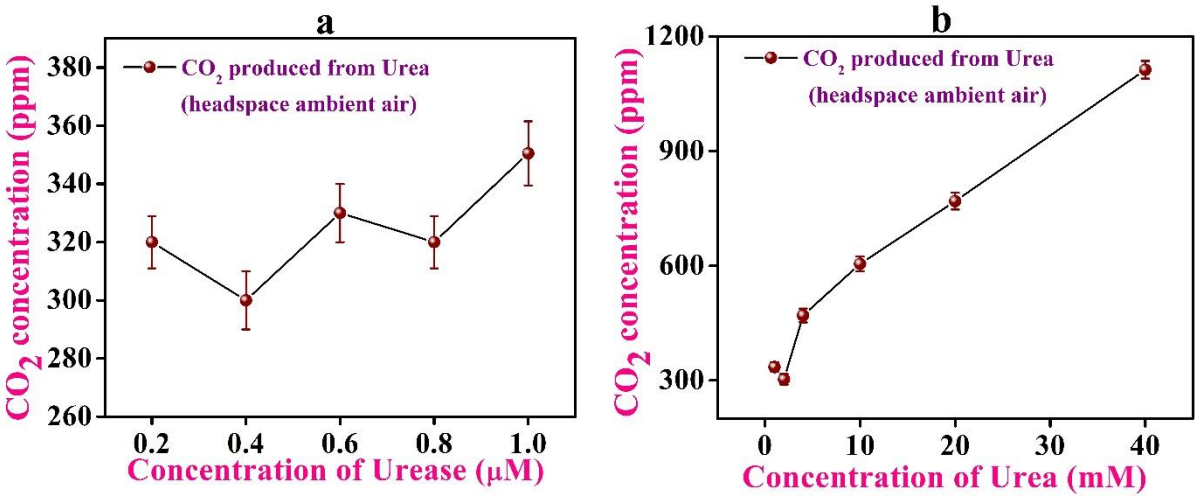

Figure: - 7.1 Concentration-dependent investigations of urea-urease hydrolysis in soil medium.

We next investigated the effects of temperature on urea-urease hydrolysis in the soil medium because temperature can play a significant role in the enzyme activities, indirectly related to soil organic matter's degradation and the global carbon cycle [12-13]. We performed the experiments at a constant concentration of urea (4 mM) and urease (1 μM) in the soil medium. We found a significant increase in the concentration of the product after 1 hour of hydrolysis with an increase in temperature from 30 ^{0}C to 105 ^{0}C (Fig.7.2 a). We also observed the similar increasing trend of the product in the second hour but a much slower rate, which signifies the slowdown of the urease activity with increasing the temperature (Fig.7.2 a). We have plotted the difference of concentration of the product between 1 hour and 2 hour and interestingly observed that the product's concentration increased with temperature till 70-75 ^{0}C and then it decreased significantly with further increase in temperature (Fig.7. 2 b). This decrease in concentration of the product (CO_2) after optimum temperature of ~ 70 ^{0}C is likely to be the effect of denaturation of the urease enzymes in the soil with the increase in temperature [12-13]. This slowdown behaviour of enzyme activity with temperature will affect the enzyme production and impact the soil microbial compositions and their activities.

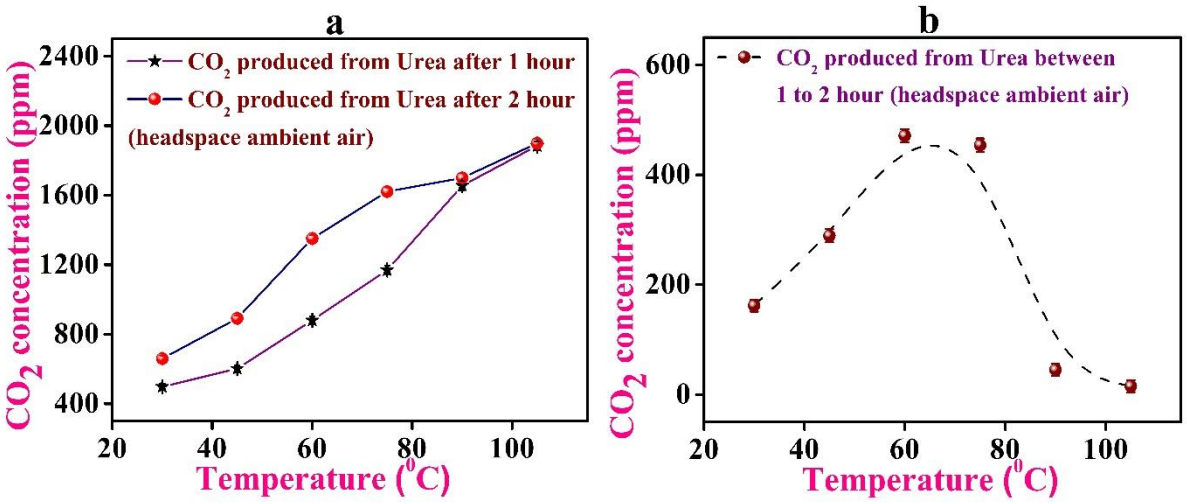

Figure: - 7.2 Temperature variation study of urea (4 mM) and urease(1µM) in soil medium.

Next, we performed the urea-urease hydrolysis in different headspace-environments in the soil medium. We have plotted the concentration product (CO_2) against the different headspace conditions like ambient air, nitrogen and pure CO_2. We observed that the concentration of the product in the nitrogen-headspace is much higher than the other two headspace conditions (Fig.7.3). These findings suggest that the minimum presence of CO_2 in the nitrogen medium enhances the hydrolysis process by activating the urease enzyme. Furthermore, we observed that with an increase in concentration of CO_2 in the ambient air and pure CO_2 headspace-environment, the output concentrations of the product decreased. This decrease is likely caused by increase in partial pressure and over-saturation of the urease enzyme because of the excess presence of pure CO_2 in the reaction environment. Taken together, these findings suggest that the headspace-environment can significantly impact the hydrolysis of urea-urease in a soil medium

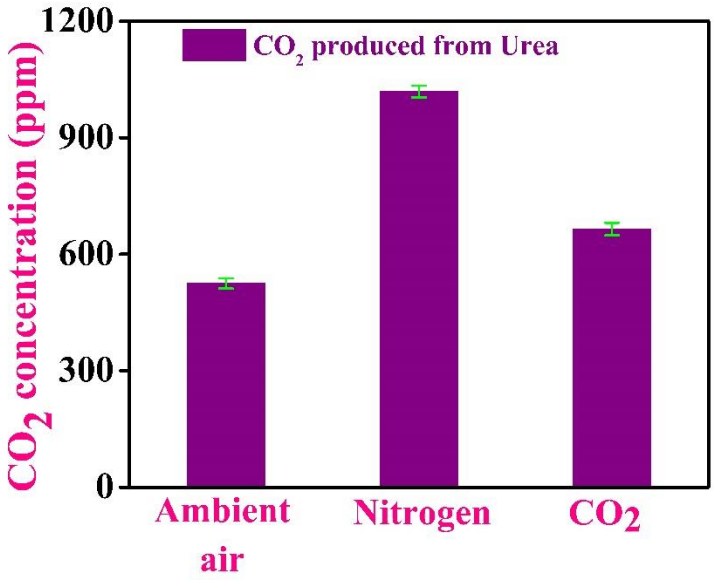

Figure: -7.3 Urea-urease hydrolysis in soil medium, under different headspace-environment study.

We next investigated any inhibition or activation effect of different concentrations of heavy water (D_2O) in the urea-urease hydrolysis in the soil medium. As mentioned earlier, the D- content solution can act as a reaction kinetics controller according to its enrichment or depletion nature. We observed that in the case of D-enriched soluble soil, the product's concentration is slightly higher compared to the normal distilled water-soluble soil (Fig.7.4 a) when the headspace was in ambient air condition. We also performed the same experiment in nitrogen-headspace and observed the same phenomena (Fig.7.4 b). It indicates that with the presence of D-enriched solution in the soil medium, the hydrolysis of urea-urease is taking place much faster than the normal hydrolysis. In order to gain more insights into the potential role of D_2O, we conducted experiments involving different concentrations (per mil) of D-enriched solution in the soil medium during urea-urease hydrolysis. The most striking findings revealed here is that a sudden decrease in the concentrations of CO_2 at a δD value of 2660 per mil as shown in Fig. 7.5b, which was followed by a return to normal hydrolysis. We also observed a similar kind of phenomenon when conducting urea-urease hydrolysis in different D-enriched solutions without any soil. We found that there is an enormous decrease in CO_2 concentrations at $\delta D \sim 305$ per mil as illustrated in Fig. 7.5a. These observations clearly manifest the isotopic resonance effects in

response to deuterium enrichments in water. Our experiments have revealed two distinct "negative resonance" values, one for soil-based urea-urease hydrolysis and another for urea-urease hydrolysis without soil. The phenomena of isotopic resonance have been previously studied [14, 17-19] in few biological systems and in general, it is known to indicate a reduction in the overall quantum mechanical complexity of a system at the resonance value of the isotopic abundances present in the solutions. In addition, the reaction rates can be enhanced or reduced at isotopic resonance, and the intensity of the resonance is largely influenced by the presence of isotopic compositions in the solutions. In view of these, in our current experiment, we have observed a shift in the isotopic resonance value due to presence of different molecular species in the soil medium when compared to a standard distilled water solution. Our results support the validity of the isotopic resonance phenomena and explored new insights into the urease-catalyzed hydrolysis of urea in soil medium in response to highly enriched deuterium oxide.

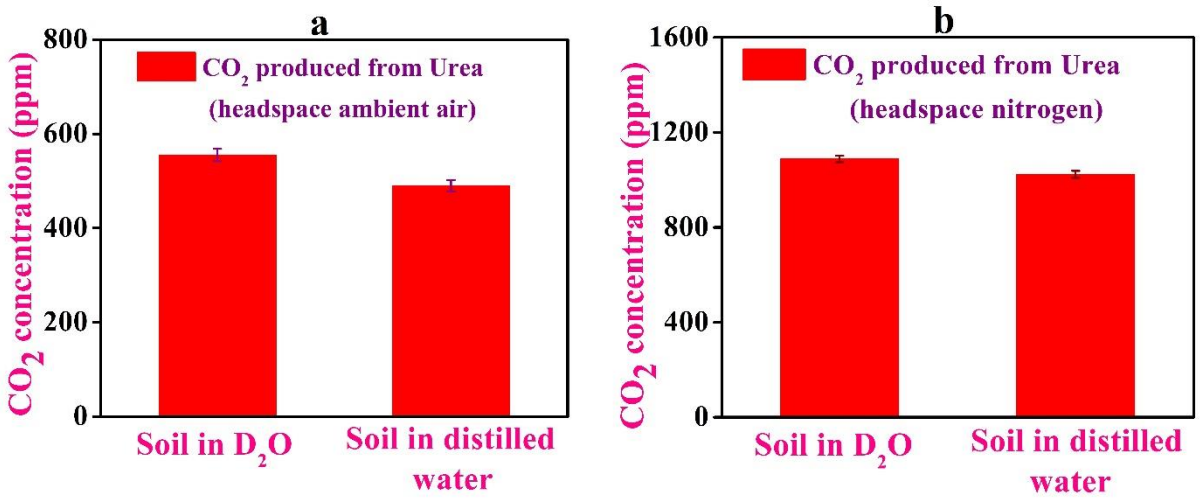

Figure: - 7.4 Urea-urease hydrolysis in response to D-enriched soluble soil and distilled water solution under different headspace conditions.

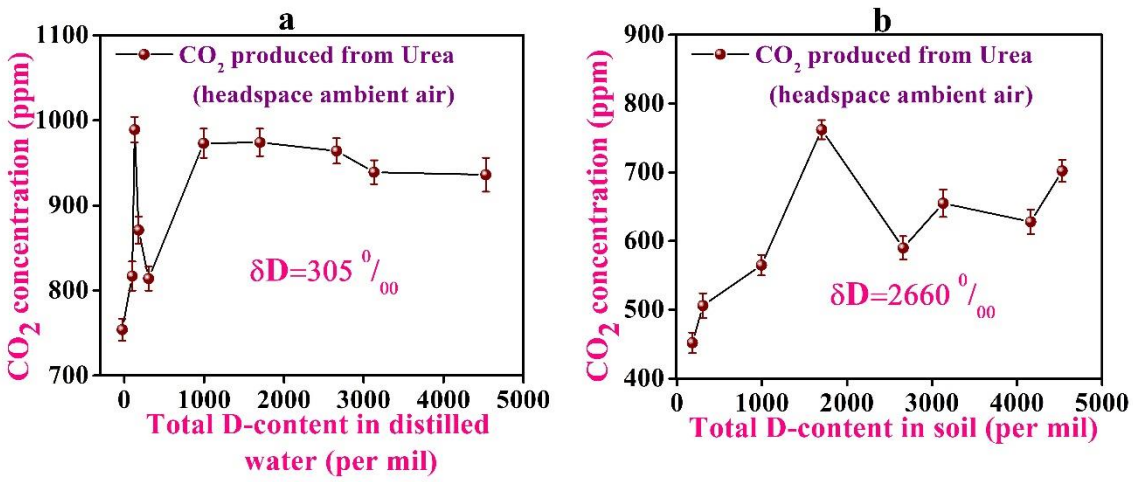

Figure:- 7.5 Investigation on urea-urease hydrolysis using different D-enriched concentrations in soil and distilled water medium and observation of isotopic resonance effects.

7.3 Conclusion

In this chapter, we have explored the detailed study of urea-urease hydrolysis in different temperatures in soil medium under different headspace conditions to know the behaviour of urease-enzyme in different reaction environments in the soil. The potential inhibition or activation effects of D- enrichment solution in the soil in both standard and nitrogen environments were investigated. We observed the first direct experimental evidence of isotopic resonance effects in the urea-urease hydrolysis for different D-enrichment concentrations in both soil medium and standard distilled water medium. Furthermore, a shift in the resonance value is observed in the soil medium with respect to distilled water medium due to the presence of different molecular species in the soil. Our findings deepen the fundamental understanding of the urea-urease hydrolysis in soil medium for different environments. The study also demonstrates that the presence of isotopic D-enrichment can act as a reaction regulator in chemical reactions involving urease enzyme and thus it may open several new applications in agricultural, environmental, biotechnology, enzymology biochemistry and some other areas.

7.4 Experimental Method

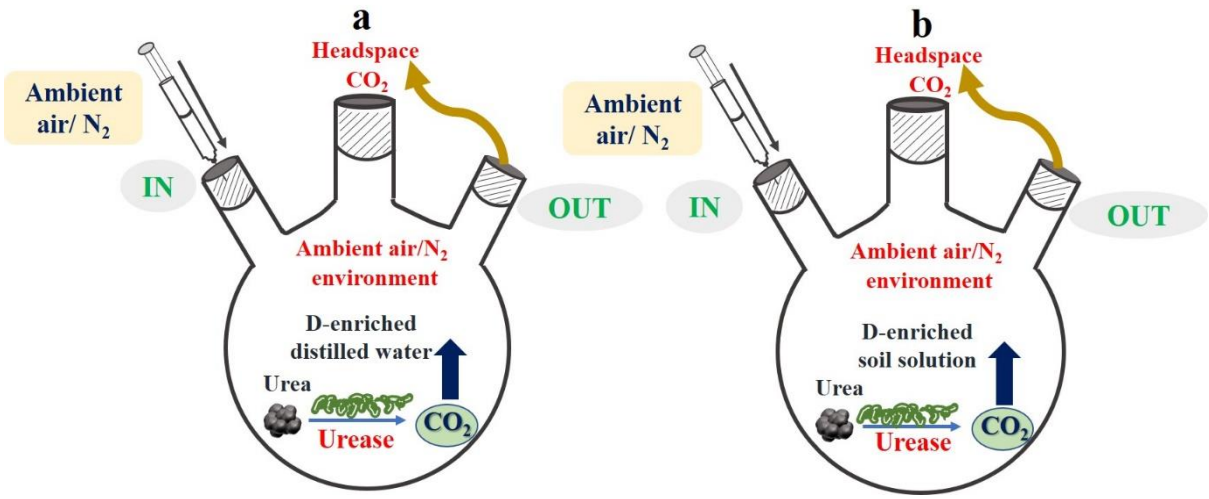

Figure: -7.6 Schematic diagram for urea-urease hydrolysis in (a) D-enriched water (b) D-enriched soil medium.

We utilized urea (^{12}C-99%) and Jack-bean urease enzyme (E.C.3.5.1.5) from Sigma Aldrich for our experiments. Milli-Q water was employed to prepare the aqueous soil solution during the experiment. To conduct the urea-urease hydrolysis in soil medium, we utilized a round-bottomed flask (Fig-7.6 a and 7.6 b). We have used typical gardening soil samples (pH-8.3, sample to water ratio=1:5) collected from the normal surface (10-20 cm) of the S. N. Bose Centres, Kolkata, campus normally during morning time (9 am -10 am, temperature: 25-30 ^{0} C, Winter season).

To gain a better understanding of the physical and chemical characteristics of the soil samples used in our experiments, we conducted a morphological study on the samples by means of scanning electron microscope (SEM) and energy-dispersive X-ray spectroscopy (EDAX). To accomplish this, we mixed approximately 1 gm of soil with 1 mL of Milli-Q water and allowed the mixture to settle down in a microtube for approximately 6 hours. We then took 10 µL of the resulting soil solution and placed it onto a silicon wafer, which was stored for 24 hours. Finally, we conducted the SEM and EDAX experiments on the solid soil texture that formed on the silicon wafer. The physical and chemical nature of the soils, as determined through this analysis, are

shown in Table-7.1 and presented in Fig.7.7. This comprehensive analysis allowed us to gain more insights into the properties of the soil samples used in our experiments.

In the experiment on urea-urease kinetics, we used 0.4 grams of soil and mixed it with 2 mL of Milli-Q water to form an aqueous solution. The solution was then stored in 2 mL microtubes for about 6 hours. To maintain a stable reaction environment, we purged the flask with nitrogen. We added 4 mM of urea and 1 μM of urease into the microtube and transferred the reactive solution into the flask using a syringe. The flasks were kept in ambient air or nitrogen environment as per requirement of the experiment.

It is worth noting that the experimental conditions were carefully controlled to ensure accurate results. For example, we used precise amount of soil and water, and stored the solution in microtubes to avoid any contamination. Additionally, we used nitrogen to purge the flask to prevent any unwanted reactions. Overall, the experimental arrangement was designed very carefully to ensure accurate and reliable results for the investigation of urea-urease kinetics. After an hour of reaction time, we collected the reaction product, from the headspace of the flask and measured the concentration of CO_2 using a high-precision integrated cavity output spectroscopy (IOCS) technique. This method allowed us to measure the CO_2 concentration with high sensitivity and accuracy.

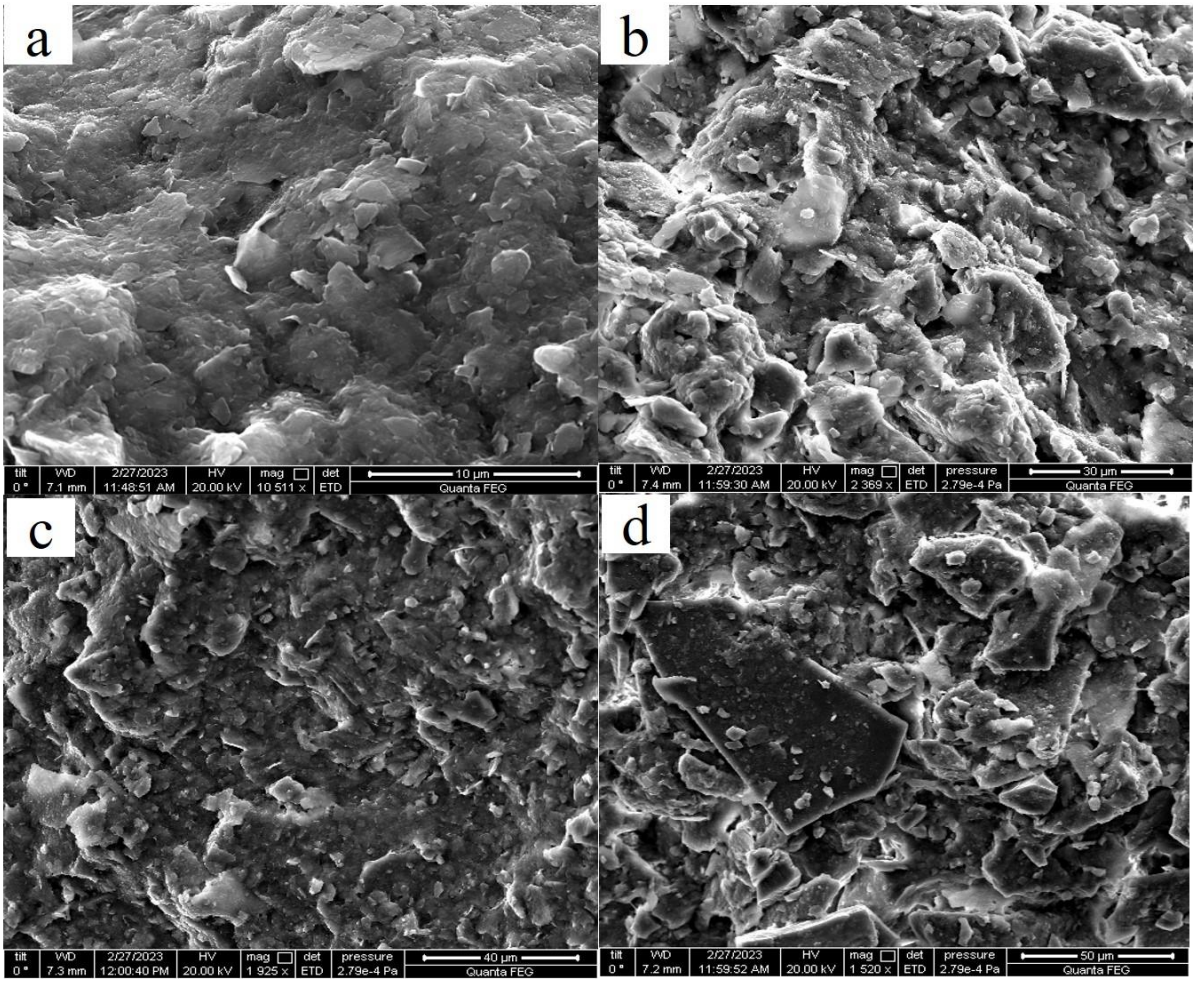

Figure: -7.7 The scanning electron microscopy (SEM) images in different magnifications for the morphological view of soil samples used in the studies.

Table-7.1

Chemical and physical characteristics of the soil samples used in the studies

Soil components	Amount in Percentage (%)	Soil components	Amount in Percentage (%)
Moisture content	10.3	Potassium (K)	4.4
Oxygen (O)	73.5	Nitrogen (N)	2
Magnesium (Mg)	3	Carbon (C)	8.3
Calcium (Ca)	1.1	Iron (Fe)	7

The measurements of the output headspace CO_2 were performed using a CO_2 isotope analyzer (CCIA 36-EP, LGR, USA). The analyzer used the OA-ICOS (off axis-integrated cavity output spectroscopy) technique for real-time measurements of CO_2. In brief, the analyzer consists of an optical cavity with two high-reflective mirrors (R~99.98%), which enhanced the optical pathlength to ~3 km. The high-resolution absorption spectra of $^{12}C^{16}O^{16}O$ were acquired at wavenumber 4874.448 cm^{-1}, belonging to the rovibrational combination band of the CO_2 molecule. The concentrations of CO_2 were measured in parts per million (ppm). In addition, for the measurement of delta D (δD) value of heavy water (D_2O), we have used a high-precision water vapor isotope analyzer (IWA-45EP, ABB LGR). This water vapour isotope analyzer operates with the same principle of OA -ICOS near 1.38 μm spectral region. The isotope ratio of water can be expressed as delta notation (δ) as given below:

$$\delta D\ (^0/_{00}) = \left[\frac{\left(\frac{HDO}{H_2O}\right)_{sample}}{\left(\frac{HDO}{H_2O}\right)_{standard}} - 1\right] \times 1000\ ^0/_{00} \qquad 7.1$$

where, $(HD^{16}O/H_2O)$ standard = 3.1152×10^{-4} is the $HD^{16}O$ abundance of Vienna Standard Mean Ocean Water (VSMOW).

7.5 References

1. Adetunji, Adewole Tomiwa, Bongani Ncube, Andre Harold Meyer, Olatunde Stephen Olatunji, Reckson Mulidzi, and Francis Bayo Lewu. "Soil pH, nitrogen, phosphatase and urease activities in response to cover crop species, termination stage and termination method." *Heliyon* vol. 7, **2021**, e05980.

2. Klose, Susanne, and M. A. Tabatabai. "Urease activity of microbial biomass in soils as affected by cropping systems." *Biology and fertility of soils* 31, **2000**, 191-199.

3. Aziz, Muhammad Abdul, Fahrizal Hazra, Selly Salma, and Dedi Nursyamsi. "Soil enzyme activities and their relationship to total soil bacteria, soil microbial

biomass and soil chemical characteristics of organic and conventional farming." *Journal of Tropical Soils* 23, **2019**, 133-141.

4. Dharmakeerthi, R. S., and M. W. Thenabadu. "Urease activity in soils: a review." *Journal of the National Science Foundation of Sri Lanka* 24, **2013**.

5. Yahya, Mukhtar Nuhu, Hüseyin Gökçekuş, Derin Orhon, Bülent Keskinler, Ahmet Karagunduz, and Philip Isaac Omwene. "A study on the hydrolysis of urea contained in wastewater and continuous recovery of ammonia by an enzymatic membrane reactor." *Processes* 9, **2021**, 1703.

6. Adetunji, Adewole T., Francis B. Lewu, Reckson Mulidzi, and Bongani Ncube. "The biological activities of β-glucosidase, phosphatase and urease as soil quality indicators: a review." *Journal of soil science and plant nutrition* 17, **2017** ,794-807.

7. Cordero, Irene, Helen Snell, and Richard D. Bardgett. "High throughput method for measuring urease activity in soil." *Soil Biology and Biochemistry* 134, **2019**, 72-77.

8. Maity, Abhijit, Mithun Pal, Suman Som, Sanchi Maithani, Sujit Chaudhuri, and Manik Pradhan. "Natural ^{18}O and ^{13}C-urea in gastric juice: a new route for non-invasive detection of ulcers." *Analytical and bioanalytical chemistry* 409, **2017**, 193-200.

9. Fapyane, Deby, Dmitriy Berillo, Jean-Louis Marty, and Niels Peter Revsbech. "Urea biosensor based on a CO_2 microsensor." *ACS omega* 5, **2020**, 27582-27590.

10. Maithani, Sanchi, Mithun Pal, Abhijit Maity, and Manik Pradhan. "Isotope selective activation: a new insight into the catalytic activity of urease." *Rsc Advances* 7, **2017**, 31372-31376.

11. Amini Kiasari, Mohsen, Mohammad Siroos Pakbaz, and Gholam Reza Ghezelbash. "Increasing of soil urease activity by stimulation of indigenous bacteria and investigation of their role on shear strength." *Geomicrobiology Journal* 35, **2018**, 821-828.

12. Moyo, C. C., D. E. Kissel, and M. L. Cabrera. "Temperature effects on soil urease activity." *Soil Biology and Biochemistry* 21, **1989**, 935-938.

13. Sahrawat, K. L. "Effects of temperature and moisture on urease activity in semi-arid tropical soils." *Plant and soil* 78, **1984**, 401-408.

14. Zhang, Xuepei, Jin Wang, and Roman A. Zubarev. "Slight deuterium enrichment in water acts as an antioxidant: is deuterium a cell growth regulator?." *Molecular & Cellular Proteomics* 19, **2020**, 1790-1804.

15. Kosenkov, A. V., M. V. Gulyaev, V. I. Lobyshev, G. M. Yusubalieva, and V. P. Baklaushev. "The reversible effect of deuteration on tissue fluid and biopolymers in normal and tumor tissues of mice." *Biophysics* 63, **2018**, 820-824.

16. Aanderud, Zachary T., and Jay T. Lennon. "Validation of heavy-water stable isotope probing for the characterization of rapidly responding soil bacteria." *Applied and environmental microbiology* 77, **2011**, 4589-4596.

17. Basov, Alexander, Liliya Fedulova, Ekaterina Vasilevskaya, and Stepan Dzhimak. "Possible mechanisms of biological effects observed in living systems during 2H/1H isotope fractionation and deuterium interactions with other biogenic isotopes." *Molecules* 24, **2019**, 4101.

18. Xie, Xueshu, and Roman A. Zubarev. "Isotopic resonance hypothesis: experimental verification by Escherichia coli growth measurements." *Scientific reports* 5, **2015**, 9215.

19. Rodin, Sergey, Paola Rebellato, Arne Lundin, and Roman A. Zubarev. "Isotopic resonance at 370 ppm deuterium negatively affects kinetics of luciferin oxidation by luciferase." *Scientific Reports* 8, **2018**, 16249.

Chapter-8

Summary of the thesis and future perspectives

Contents

8.1 Summary of the thesis……..142

8.2 Future perspectives……..……..144

8.2.1 Field specific deployment of 2f-WMS sensor……...……..144

8.2.2 Development of incoherent broadband cavity enhanced spectroscopy ……..……..…..….145

8.3 References……...…….145

8.1 Summary of the thesis

This thesis has been involved on the demonstration of techniques like cavity ring-down spectroscopy, wavelength modulation spectroscopy and their application in the field of spectroscopy and trace monitoring have been discussed.

Firstly, we have utilized our lab developed continuous wave (*cw*) external-cavity (EC)-QCL coupled with CRDS technique for the spectroscopic investigation of ^{13}C-isotope of CH_4. We acquired experimental absorption features of all the selected transitions of $^{13}CH_4$ in the 7.8-micron region. We, thereafter, evaluated the line-intensity of the selected transition lines of $^{13}CH_4$ by injecting the standard calibrated gas at different pressures into the optical cavity. We next investigated the effect of air pressure on the spectral lines of $^{13}CH_4$ at room temperature (296 K). We calculated the air broadening coefficient (γ) from the slope of the linear fit between Lorentzian FWHM and total pressure for the respective transitions of $^{13}CH_4$ isotope. We finally explored the effect of temperature on the broadening co-efficient (γ) of the selected transitions of $^{13}CH_4$ and calculated the temperature dependent exponent of all absorption lines. This is an

important spectroscopic parameter to accurately interpret the spectra at high temperatures such as extra-terrestrial spectrum.

In the next chapter, we investigated into the fundamental vibrational band of $^{12}CH_2D_2$ isotopomer, which corresponds to the CH2-wagging motion. We examined the high-resolution ro-vibrational gas-phase spectra of this molecule and performed a PGOPHER simulation to verify the experimental spectroscopic parameters against the simulation parameters. Moreover, we conducted an investigation into the impact of collisional or pressure broadening on the ro-vibrational lines of $^{12}CH_2D_2$ at room temperature (296K) with various foreign gases. This allowed us to move beyond the constraints of low-pressure, Doppler broadened conditions and expand our spectral measurements to higher pressures. Through this study, we were able to determine the pressure broadening coefficients, denoted as γ_i in cm^{-1} atm^{-1} (i = He, Ar, N2, Hydrogen mixture, and zero air), for each foreign gas. The findings related to the pressure broadening effect and its coefficients are of significant importance in the analysis of atmospheric spectra and have far-reaching implications in planetary science. These results provide essential information for understanding the complex interactions of molecules in the atmosphere and their impact on the overall atmospheric composition.

In the next chapter, we have developed a mid-IR 2*f*-wavelength modulation spectroscopy (WMS) detection system combining a continuous wave (cw) external-cavity quantum cascade laser (EC-QCL) at 5.2 μm and an astigmatic multi-pass cell with path-length 76 m for the monitoring of nitric oxide (NO) and carbonyl sulfide (OCS). We demonstrated the detailed development experimental of experimental set-up and optimized the output signal using modulation amplitude and pressure. Further, we applied the WMS system for simultaneous probing of NO and OCS exploiting both direct absorption spectroscopy (DAS) and WMS technique for different concentrations of NO and OCS and shown a well-observed difference in the signal-to-noise ratios evidenced of higher-sensitivity of the WMS technique over the DAS technique.

We next used the wavelength modulation spectroscopy techniques for the dual-species (CH_4 / N_2O) monitoring optical detection method at 7.8 μm combining an

astigmatic multipass cell and a *cw* EC-QCL light source. The system exploits the fundamental principle of 2*f*-WMS and it can quantitatively monitor CH_4 and N_2O concentrations both in ambient air and exhaled breath samples with high sensitivity and molecular selectivity. We utilized the lab-developed 2*f*-WMS optical detection strategy coupled with the 7.8 µm *cw*-EC-QCL source for the simultaneous measurements of ambient and exhaled CH_4 and N_2O mixing ratios to ensure the feasibility of measuring real samples. We collected the atmospheric air samples from the campus of the S.N. Bose Centre, Kolkata and breath samples and subsequently measured the ambient concentrations of CH_4 and N_2O.

In the final part of the thesis, we have explored and observed the direct experimental evidence of isotopic resonance effects in the urea-urease hydrolysis both in soil medium and standard distilled water medium in response to D-enrichment. This study explores that the presence of isotopic D-enrichment can act as a reaction regulator in chemical reactions involving urease enzyme. These findings have several applications in environmental, agriculture, clinical science areas along with the development of enzymology biochemistry.

8.2 Future perspectives

8.2.1 Field specific deployment of 2f-WMS sensor

As discussed in chapter-6 and 7, the developed high-sensitive sensor can further update and can be applied in the field measurement of trace molecules concentrations in both atmosphere and biological breath samples. This will help us to understand the atmospheric chemistry and also the measurement of breath samples can help us to relate various diseases to trace gases and early diagnosis of diseases.

8.2.2 Development of incoherent broadband cavity enhanced spectroscopy

Incoherent broadband cavity-enhanced spectroscopy (IBBCEAS) is a technique used in analytical chemistry to detect and quantify trace amounts of gases and other substances in a sample [1-2]. The technique involves shining a broadband light source through a cavity, which contains the sample to be analyzed. The cavity is designed to enhance the interaction between the light and the sample, increasing the sensitivity of the measurement. As the light passes through the cavity, it undergoes multiple reflections and becomes trapped, increasing the path length of the light and allowing for more precise measurements. We have focused to develop a simple high-sensitive sensor that can be used to monitor multiple trace gases like NO_2, SO_2, O_3 etc.

8.3 References

[1] Zheng, Kaiyuan, Chuantao Zheng, Ningning Ma, Zidi Liu, Yue Yang, Yu Zhang, Yiding Wang, and Frank K. Tittel. "Near-infrared broadband cavity-enhanced spectroscopic multigas sensor using a 1650 nm light emitting diode." *ACS sensors* 4, no. 7 (2019): 1899-1908.

[2] Liu, Jingwei, Xin Li, Yiming Yang, Haichao Wang, Cailing Kuang, Yuan Zhu, Mindong Chen, Jianlin Hu, Limin Zeng, and Yuanhang Zhang. "Sensitive detection of ambient formaldehyde by incoherent broadband cavity enhanced absorption spectroscopy." *Analytical chemistry* 92, no. 3 (2020): 2697-2705.